A COMPARISON OF THE SEISMIC PERFORMANCE OF PRECAST WALL CONSTRUCTION : EMULATION AND HYBRID APPROACHES

A research report submitted in partial fulfilment of the requirements for the degree of
Master of Civil Engineering

Tony John Holden

February 2001

University of Canterbury
Christchurch, New Zealand

ABSTRACT

Two geometrically identical half-scale precast concrete wall units were constructed and tested under reversed cyclic lateral loading. One unit was conventionally reinforced designed in accordance with NZS 3101: 1995 for full ductile response. The wall panel in this unit was grouted within a slot connection cast into the foundation beam. The other unit was part of a hybrid system that incorporated post-tensioned unbonded carbon fibre tendons and steel fibre reinforced concrete. Hysteretic energy dissipation devices were introduced by incorporating low yield strength tapered longitudinal reinforcement, acting as a fuse connection between the wall panel and the foundation beam.

The geometry chosen for the walls was representative of a prototype four-storey building.

Comparisons between the hybrid wall system and a precast conventionally reinforced specimen are made.

Benefits of the hybrid structural system are highlighted in comparison with conventional monolithic construction.

ACKNOWLEDGEMENTS

This research was performed at the University of Canterbury Civil Engineering Department, New Zealand, under the guidance of Dr Jose Restrepo and Professor John Mander.

Special recognition to my supervisor Dr Jose Restrepo for his guidance, advice, and patience throughout the year.

Thanks must go to all the technical staff of the Civil Engineering Department's Structural Lab, in particular Kevin Wines, Richard Newton, and Stuart Toase. Special thanks to Morehu Rangi for his selfless and much needed help.

Appreciation goes to all my friends especially my fellow Masters colleagues, for all their support and understanding. Particular praise goes to Damon Ho for his technical advice, Luis Toranzo for his interest and good humour and Matthew Lander for his witty distractions.

I would like to thank the University of Canterbury for the graduate Scholarship I received which enormously helped me in the completion of my Masters year of study.

BBR Switzerland for their generous donation of the carbon fibre post-tensioning tendons used in the construction of the hybrid wall unit.

Construction Techniques for providing technical advice on prestressing aswell as being suppliers of the hydraulic post-tensioning rams.

Firth Industries for their interest in this project.

Jurban Naddef and all the people at Stresscrete for their advice as well as being suppliers of the steel fibre reinforced concrete used in the construction of the hybrid wall unit.

Special thanks goes to my family for their encouragement and love.

TABLE OF CONTENTS

LIST OF FIGURES

LIST OF TABLES

NOTATION

a	tapered length
$a/2$	position of the centroid of the compression longitudinal reinforcement assumed in design
a_y	height of taper where yielding will take place
A_g	gross cross-sectional area of unit
A_{sd}	area of tapered section of dissipator bar
A_{sp}	area of carbon fibre reinforced rods
A_r	aspect ratio
b_w	wall panel thickness
c	Neutral axis depth
d	fibre equivalent diameter (mm)
d_b	nominal bar diameter
d_{br}	diameter of the milled portion in an energy dissipator
e	eccentricity of main diagonal strut
E_c	Young's modulus of concrete
E_s	Young's modulus of steel
E_s'	strain hardening modulus of steel in the idealised stress-strain relationship
E_{sp}	elastic modulus of carbon fibre reinforced rods
f'_c	cylinder compressive strength of concrete
f_{su}	ultimate tensile strength of steel
f_t	tensile stress
f_t'	direct tensile strength of concrete
f_y	yield strength of steel
$\bar{f}_y$	mean yield strength of steel
F_{ed}	ultimate tensile force in a energy dissipation bar
H	summation of $H_{rock} + H_{ed}$
H_{ed}	lateral force required to form the bond mechanism
H_p	in-plane displacement at the top of the wall at the ultimate tensile stress of the energy dissipators

H_r	in-plane displacement at the top of the wall at the commencement of rocking
H_{rock}	lateral force required to form the rocking mechanism
H_u	in-plane displacement at the top of the wall at the expected fracturing of the energy dissipators
H_w	height of applied load
H_y	in-plane displacement at the top of the wall at the commencement of yield of the energy dissipators
I_g	gross section moment of inertia
l_w	wall panel width
k_{ed} and K_{ed}	elastic stiffness of energy dissipators
k'_{ed} and K'_{ed}	strain hardening stiffness of energy dissipators
K_p and k_p	stiffness of carbon fibre reinforced tendons
K_r	stiffness of rocking system
K_w	uncracked stiffness of wall panel
L	fibre length
L_{ed}	milled length of the energy dissipation bar
L_{sp}	unbonded length of carbon fibre reinforced rods
M_b	base moment
M_n	theoretical moment capacity obtained using the measured material properties and the equivalent rectangular stress block for concrete
OA	gap between top of reduced section and concrete
p_e	longitudinal reinforcement ratio
p_l	longitudinal reinforcement ratio at wall ends and centre
p_s	volumetric confinement reinforcing ratio
p_v	transverse reinforcement ratio
P	combined applied axial load + post-tensioning force
r	radius of chamfer
W	self-weight of wall panel
Δ	in-plane displacement at the top of the wall
Δ_e	elongation demand of energy dissipator
Δ_{ea}	elongation at tapered section of dissipator

Δ_{eLed}	elongation at reduced section of dissipator
Δ_p	in-plane displacement at the top of the wall at the ultimate tensile stress of the energy dissipators
Δ_r	in-plane displacement at the top of the wall at the commencement of rocking
Δ_u	in-plane displacement at the top of the wall at the expected fracturing of the energy dissipators
Δ_y	reference yield displacement in a unit designed using the emulation approach
Δ_y	in-plane displacement at the top of the wall at the commencement of yield of the energy dissipators
ε	strain
ε_s	steel strain
ε_{sh}	strain hardening of steel
ε_{ss}	surface steel strain
ε_{su}	uniform tensile strain of steel
ε_y	yield strain of steel
μ_Δ	displacement ductility = Δ/Δ_y
θ	drift angle
θ_y	reference yield drift ratio = Δ_y/H_w
θ_u	design drift angle
ϕ	curvature
ϕ_b	curvature at bottom of region of plastic rotation
ϕ_t	curvature at top of region of plastic rotation
λ_u	ultimate to yield strength ratio f_{su}/f_y

1 INTRODUCTION

1.1 GENERAL

Structural walls are a common and cost effective way of providing lateral force resistance to buildings in seismic areas of the world. They have been used successfully in New Zealand over a number of years in the construction of low and high rise reinforced concrete buildings.

Walls offer two major advantages over frame structures. First, they can efficiently limit seismic drift and, thus, limit damage to non-structural elements. Second, they are more stable with overturning due to P-Δ effects not occurring until displacements, typically much larger than those experienced in an earthquake, occur. The inherent stability of wall units was well illustrated during the 1988 Armenia, formerly USRR, earthquake (Wyllie, 1989), where even poorly designed and constructed precast wall buildings generally survived, whereas many frame buildings collapsed. Buildings where lateral force resistance was provided by walls also showed excellent performance during the 1985 Chilean Earthquake. (Wood et al, 1987)

One of the main disadvantages of conventional cast-in-place construction, or precast concrete construction designed to behave as "if monolithic", is that the walls are expected to be sacrificed in the potential plastic hinge regions. Significant structural damage and large residual lateral displacements are expected to occur with such systems. This would inevitably lead to expensive repairs and business downturn. Hence, like with other conventional systems the cost of consequences of damage after an earthquake may be significant to the building owner.

To reduce some of the adverse effects observed with traditional monolithic systems, Priestley and Tao, (1993) first proposed the idea of utilising unbonded prestressing in structures to provide the primary lateral force resistance. When the tendons are left unbonded and kept elastic during rocking the elastic restoring force will essentially eliminate residual lateral displacements. Since the concrete is not bonded to the tendons, much less cracking is induced than in monolithic walls that rely solely on bonded reinforcement to provide the lateral force resistance. The behaviour of such a

system can be described as being non-linear elastic. In these systems cosmetic damage is restricted to the bottom corners of the wall about which it rocks. Special reinforcing details can be provided in these areas to limit or eliminate concrete crushing. The main disadvantage of this purely non-linear elastic system is the lack of energy dissipation capacity. By incorporating low yield strength reinforcement between the wall unit and its foundation, a level of hysteretic damping can be introduced to reduce the response to seismic excitation, while still ensuring that the self-centring characteristics are preserved.

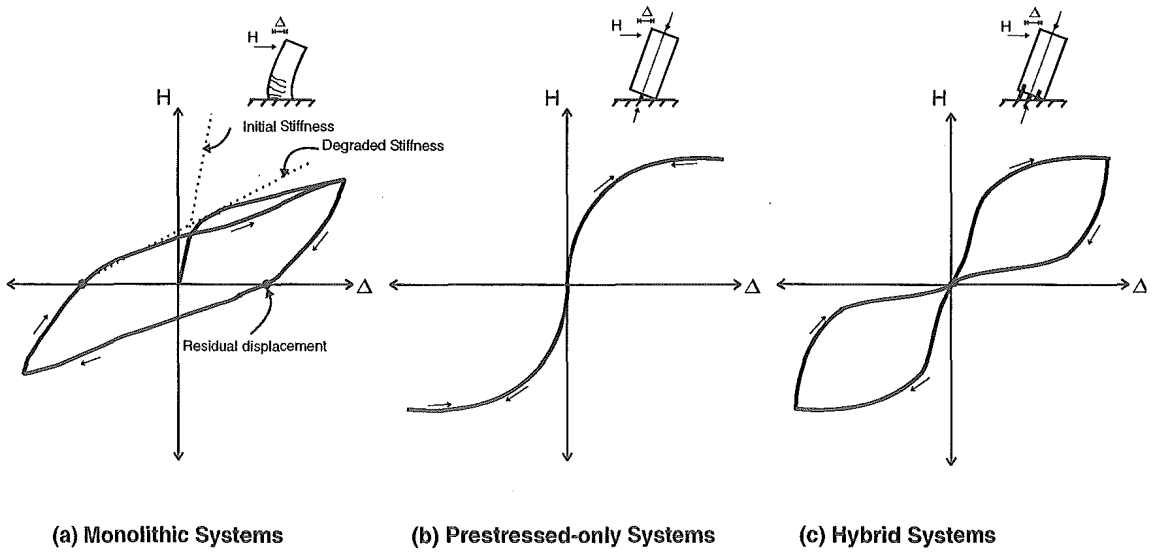

Figure 1.1 Hysteretic response of various structural systems.

Table 1.1 Comparison between conventional and hybrid wall systems.

SYSTEM PROPERTY	MONOLITHIC	HYBRID
Energy Dissipation Capacity	Excellent.	Good.
Special Reinforcing Detailing	In potential plastic hinge zones. Congested cages to confine the concrete, prevent longitudinal reinforcing from buckling, and to prevent shear failure.	Only required at wall ends and foundation beam where rocking takes place.
Dimensional Limitations	To prevent plastic hinge instability.	Minimum – based on elastic theory as wall panels remain essentially crack free.
Minimum Reinforcement Requirements	Can significantly increase the moment capacity at the critical region. This could result in larger foundations as a result of capacity design.	None.
Expected Post-Earthquake Repair Work	In plastic hinge zones repair work can vary from epoxy injection of 1mm wide cracks or less, to concrete replacement. Longitudinal bars could buckle and fracture. Permanent deformations.	Cosmetic repairs at most. Self-centring, permanent deflections are not expected.
Initial Cost	Competitive – widely used systems.	Competitive? Requires cost analysis.
Life-Cycle Cost	Competitive relative to other conventional systems. Repair work localised in few locations.	Expected to be very competitive.

Figure 1.1 and Table 1.1 clearly show the inherent benefits of hybrid systems, over that of monolithic and prestressed only systems. Monolithic systems can dissipate large amounts of energy, but this is provided though structural damage that lead to a degradation in the stiffness, as well as residual drift. Prestressed-only systems incorporating unbonded tendons behave non-linear elastically, thus, remain essentially damage free and have self-centring characteristics after unloading to large lateral displacements. They dissipate little energy, which is expected to lead to displacement demands larger than for those systems in which energy dissipation can take place. Hybrid systems combine the benefits of both providing a good level of energy dissipation, while remaining essentially damage free, with no residual drift.

As part of this research project a hybrid wall system was developed. A number of innovative materials were also utilised and investigated.

A significant portion of the design of the hybrid wall unit in this project utilised strut-and-tie modelling techniques in which statically admissible internal force flows are identified in order to establish the locations and quantities of steel reinforcement required to carry both tensile and compressive forces. This technique also allows one to check whether the compressive forces carried by the concrete are within acceptable levels. This type of approach replaces the requirement of designing a conventional reinforcing mesh such as that outlined in the New Zealand Concrete Structures Standard (NZS 3101, 1995).

Carbon fibre prestressing tendons replaced conventional prestressing tendons or rods. These tendons have a number of advantages over conventional prestressing. They behave elastically up until failure (i.e behaviour excludes a yield plateau). This has the benefit of reducing prestress loss due to creep, time losses, as well as that associated with permeant yield elongation. Corrosion resistance is another benefit. This is not greatly significant in the context of this research project, but would have greater implications for structures incorporating similar ideas in marine type environments such as in wharfs or piers.

Prior to obtaining the carbon prestressing rods initial investigations were directed towards utilising Dual-phase Composite Prestressing Steel ("DraCom strands"). Each strand contains 4 ordinary strength wires (400 MPa), and 3 high strength wires (1400 MPa). Further examination, however, cast doubt on the behaviour of this material under cyclic loading.

"Dramix" steel fibres (RC-65/35-BN) were added to the concrete mix design in an effort to improve crack control, and ease of the reinforcement cage in the wall panel. Emphasis was particularly paid to the un-reinforced regions of the wall.

It is believed that such a system, based on that outlined, could be constructed for a similar cost to that of a conventionally reinforced wall but perform much better under seismic loading requiring little or no repair after an earthquake event.

1.2 RESEARCH SIGNIFICANCE

If one were to ask a member of the public to give his/her perception about a seismically designed building, the general perception would be that the building would remain essentially undamaged and serviceable after a moderate to strong earthquake. This is in wild contrast to the view of the structural engineer whose main objective is to design a structure to remain essentially damage free given small frequently occurring earthquakes and to avoid building collapse and loss of life in a strong earthquake. This is normally achieved by designing ductile systems that are able to reduce the buildings response through energy dissipation the in plastic hinges. One major drawback of this approach is that the plastic hinge regions are part of the main structure. Consequently, the engineer accepts that parts of the structure itself are expected to be sacrificed. The discrepancy between the designers and lay community perspective's are well documented. For example Otani, (1997) reviewing the consequences of the 1995 Kobe earthquake in Japan says *"A significant gap existed between the expectations of structural performance by the building owner (people) and the structural engineer. The public should have been informed of the consensus of the engineer and researcher. The structural engineer should have explained the owner the expected performance of the building under various intensity earthquakes including the expected damage of non-structural elements."*

If, after a moderate or strong earthquake a building performs to the expectations of the design standard, the structure has probably deformed beyond the elastic limit and there has been little or no loss of life. The owner of the building is in most likelihood very unhappy given that a supposedly seismically designed building is now in need of moderate to large repairs, is temporarily unserviceable, or in some cases must in fact be condemned. There is an obvious gap between public expectation and the reality of current seismic design.

The effect of a large earthquake event on an economy, especially one in a developing country and equally to a hi-tech centre in a developed country, can be devastating, crippling a society that may take years to recover.

The structural engineers' role has historically focused on ensuring the safety of society while recognising the limitations that economics places on design. To design a structure elastically using conventional design methods and philosophies is not always economically viable. Engineers therefore, in general, have designed structures for reduced lateral forces and accepted damage in locations that are specifically designed for sufficient ductility. Uncoupling the energy dissipation mechanism from the structure is an ideal solution that was first thought and implemented through seismic isolation design. Seismic isolation is a relatively new method engineers have developed in order to circumvent this problem. This solution however has generally been restricted especially in New Zealand to nationally significant structures with little use pertaining to general commercial structures.

The hybrid wall unit tested as part of this research represents a simple alternative for seismic design. It uses the hardware commonly used for traditional construction systems but it suppresses damage from occurring within the structure, thus removing any post-earthquake repairability issues and associated business downturn.

1.3 SCOPE OF THE RESEARCH

The primary aim of this research was to develop a hybrid wall unit incorporating post-tensioned unbonded carbon fibre tendons rods and steel fibre reinforced concrete, and compare its behaviour with a precast concrete wall unit designed in accordance with the recommendations given in the Concrete Structures Standard (NZS 3101, 1995), for ductile monolithic wall systems.

The basis of this research project continues on from the advances made from the previous research work conducted by Rahman and Restrepo (2000) at the University of Canterbury. In particular the behaviour of Unit 3 tested by these researches is compared with the test results obtained for the two units tested in this project.

It is hoped that this research in part could help lead to the development of systems that not only provide significant life cycle cost benefits but are also cost competitive with more conventional systems in terms of the initial cost.

1.4 LITERATURE REVIEW

A literature review pertaining only to hybrid wall structures will be discussed in this report, a more comprehensive review having been completed by Rahman and Restrepo (2000).

1.4.1 Kurama et al. (1999)

Kurama et al. gave a series of design recommendations for precast concrete walls incorporating unbonded post-tensioning bars. These recommendations were based on over 200 dynamic time-history non-linear analyses of six, six-storey high prototype walls, conducted using a total of 15 design level and 15 survival level ground motion records.

Figure 1.2 illustrates the basic wall geometry and tendon layout chosen for the analyses. Horizontal joints representing each storey allow for gap opening and shear slip behaviour under lateral forces. Given that there is no restoring force to reverse shear slip and that it is difficult to control the magnitude of these displacements, which may occur during an earthquake, the researchers recommend that shear slip be prevented through proper design and detailing. A confinement ratio of 7.3% and a concrete compressive strength of 41.4 MPa were assumed. Performance criteria corresponding to the NEHRP design ground motion for a 500-year return period were defined by ensuring that no yielding of the post-tensioning bars or significant damage to the concrete in the precast unit. Failure at the survival level ground motions, corresponded to a 2500-year return earthquake. At this stage crushing of the concrete or fracture of the spiral confinement were defined as the performance objectives at this stage.

The location, unbonded length and initial stress of prestressing steel determine the lateral displacement at which yield occurs. Premature concrete is prevented by providing spiral reinforcement at the wall ends over a length equal to at least one-quarter of its length and over a height greater than or equal to the height of the first storey of the building.

The analyses show that higher modes do not have a significant influence on the lateral displacement, whereas the base shear demands are highly sensitive to these effects. The length of the gap opening at the wall panel-foundation interface, for a system compromising several precast units connected by unbonded prestressing steel, is found to independent on the intensity of the ground motion and the amount of initial prestress. The analyses showed that, compared to cast-in-place walls, unbonded post-tensioned precast walls undergo larger drifts but accumulate significantly smaller residual drifts during an earthquake.

Based on their studies, the authors recommend a wall height-to-length ratio equal to or larger than 3 to ensure flexural behaviour under lateral loading conditions. They also recommend that a conservative value of the coefficient of shear friction be used in design to avoid shear slip. Recommendations regarding the selection of wall design properties such as the initial stress in the post-tensioning steel, wall length, unbonded length of the post-tensioning steel, location of the post-tensioning steel, and amount of spiral reinforcement are also given.

This research summarises that unbonded post-tensioned precast walls provide a feasible alternative to conventional monolithic cast-in-place concrete walls in seismic regions.

1.4.2 Priestley et al., (1999)

Priestley et al. tested a five-storey precast concrete building, constructed to 60 percent scale, under pseudo-dynamic loading as the culmination of the 10-year PRESSS (Precast Seismic Structural Systems) research program. The building comprised of four different ductile structural frame systems in one direction of response and a hybrid structural wall system in the orthogonal direction, see Figure 1.3. The test structure was subjected to seismic input levels equivalent to at least 50% higher than those required for the Uniform Building Code (1997) seismic Zone 4. The behaviour of the structure was found to be extremely satisfactory, with only minimal damage in the wall direction. This in spite of being taken to drift levels up to 4.5%, more than 100% higher than the design drift level. The test validated the Displacement-Based Design approach used to

determine the required strength and confirmed the low damage and low residual drift expected from hybrid wall systems.

The wall remained essentially uncracked except at the base connection to the foundation where minor spalling was observed. The wall showed additional flexural cracking when subjected to a 4.5 percent out-of plane drift in the frame direction of response. However, these cracks closed up at the end of testing. As anticipated, the residual drift after the design level excitation was very low. In the wall direction, the residual drift was 0.06% after sustaining a peak drift of 1.8%.

1.4.3 Rahman and Restrepo (2000)

Research conducted by Rahman and Restrepo (2000) involved the testing of 3 half-scale precast concrete wall units, subjected to a quasi-static reversed cyclic loading regime. The reinforcement details, prestressing strand arrangement and loading regime were similar for all three walls. Conventional rectangular ties and longitudinal bars were used to reinforce each of the specimens. Figure 1.4 shows the general geometry and reinforcement of the final unit tested, Unit 3. The first specimen tested, Unit 1, was a prestressed-only system with no account made for gravity loads. A simple energy-dissipation device in the form of a standard reinforcing bar with a reduced diameter over a specified length was incorporated into the design of Units 2 and 3. Gravity load effects were simulated in Unit 3 by means of external post-tensioning. Each wall panel was conventionally reinforced, designed to perform satisfactorily up to 2.5% drift.

All three units tested were found to perform well. Damage to each of the three specimens was cosmetic and was concentrated at the toes of the wall where the rocking mechanism against the foundation caused large concrete compressive strains. High drift levels in excess of 2.5% were attained in all three specimens. The absence of residual drifts in the precast wall units was achieved through the near elastic behaviour of the prestressing strands. The energy dissipators were found to be very effective. Equivalent viscous damping ratios of up to 14% were obtained in the units that incorporated the energy dissipation devices.

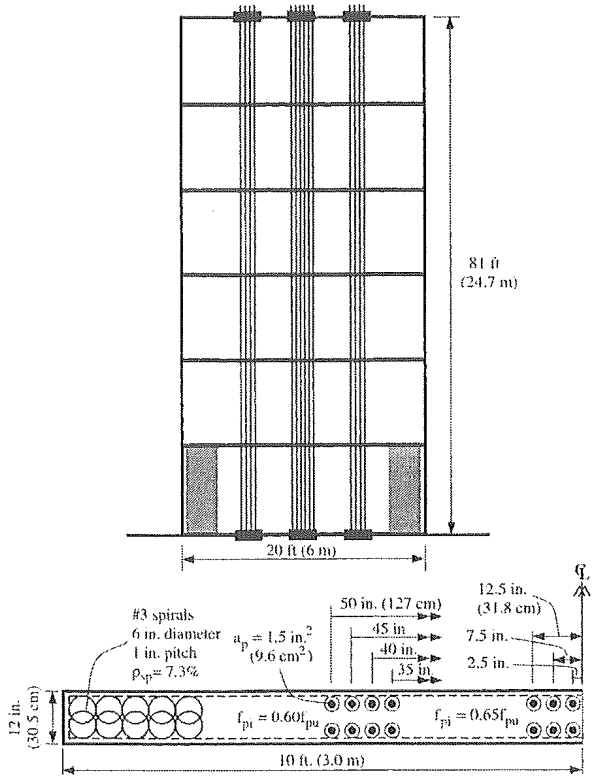

Figure 1.2 Basic geometry and tendon layout of a prototype wall analysed by Kurama et al. (1999).

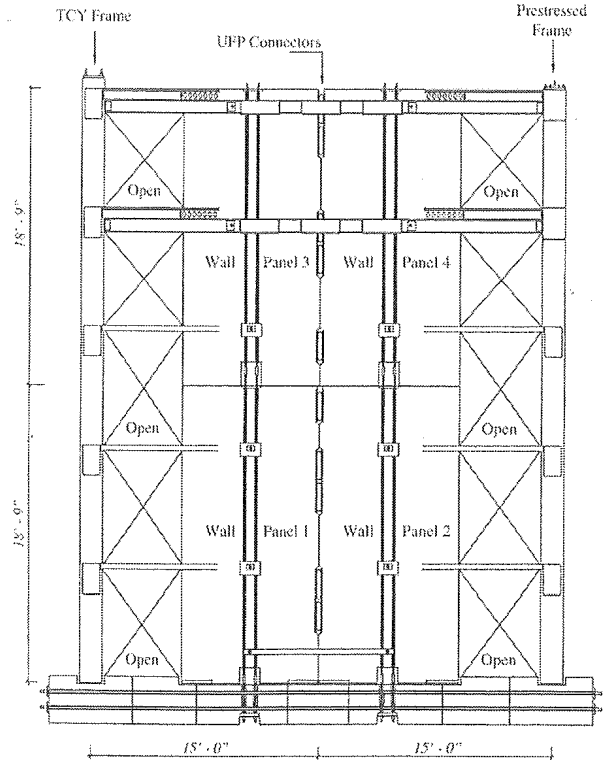

Figure 1.3 Jointed structural wall elevation of the PRESSS building tested by Preistley et al. (1999).

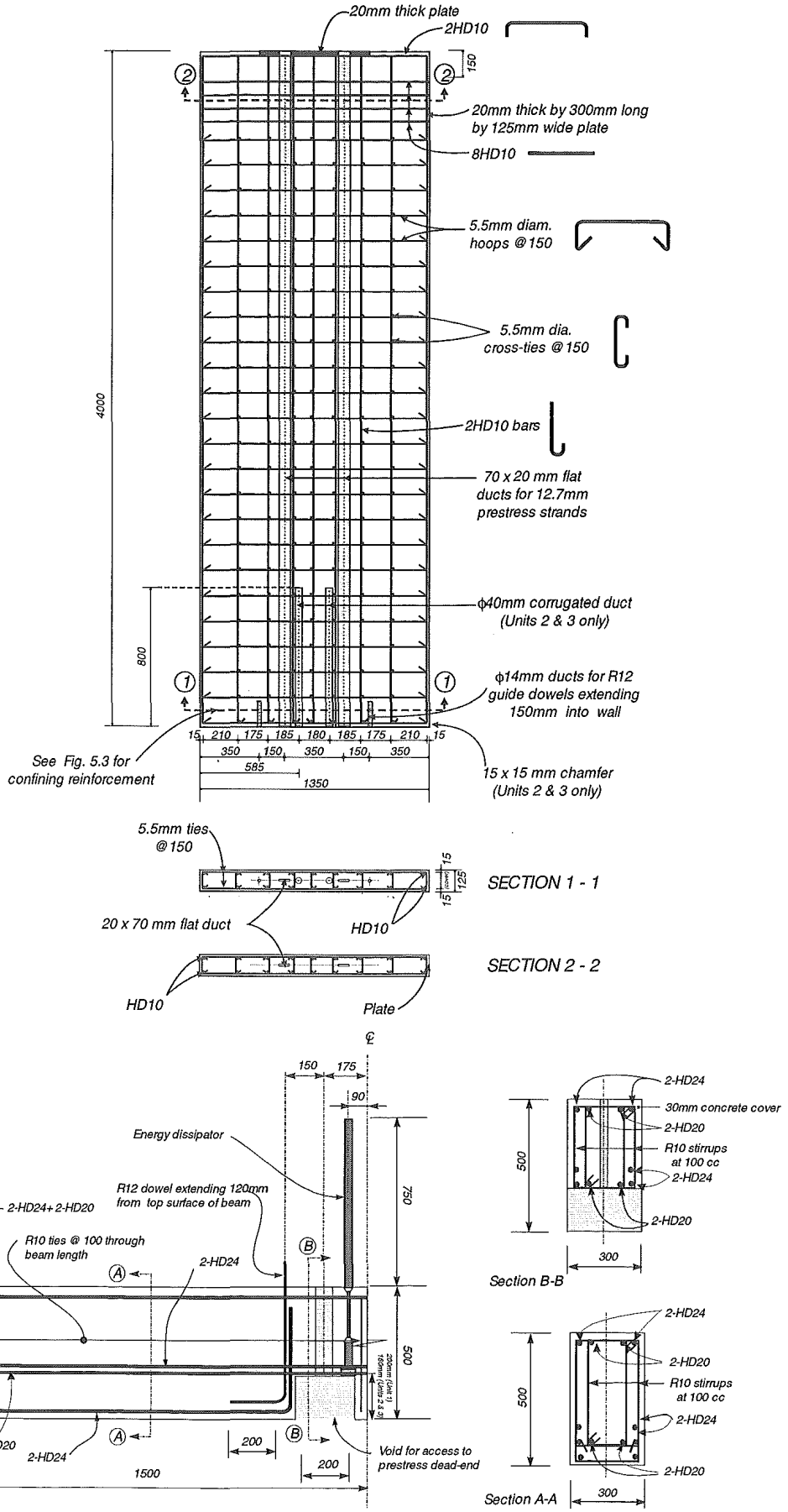

Figure 1.4 Reinforcement details of the hybrid Unit 3 tested by Rahman and Restrepo (2000).

2 DESIGN AND PREPARATION OF TEST UNITS

2.1 GENERAL

Two identical half-scale precast wall units were constructed as part of this research programme. The geometry chosen for the test units was taken from a prototype four-storey building. The basic dimensions of the units are presented in Figure 2.1.

The prototype and test wall normalised bending moment diagram's are similar as illustrated in Figure 2.2. Both walls have identical $M_b/(H.l_w)$ ratios in which M_b is the base bending moment H is the base shear force and l_w is the length of the wall. Given the nature of the single point quasi-static loading used, no account is given to the effects caused by dynamic loading or the higher modes of vibration.

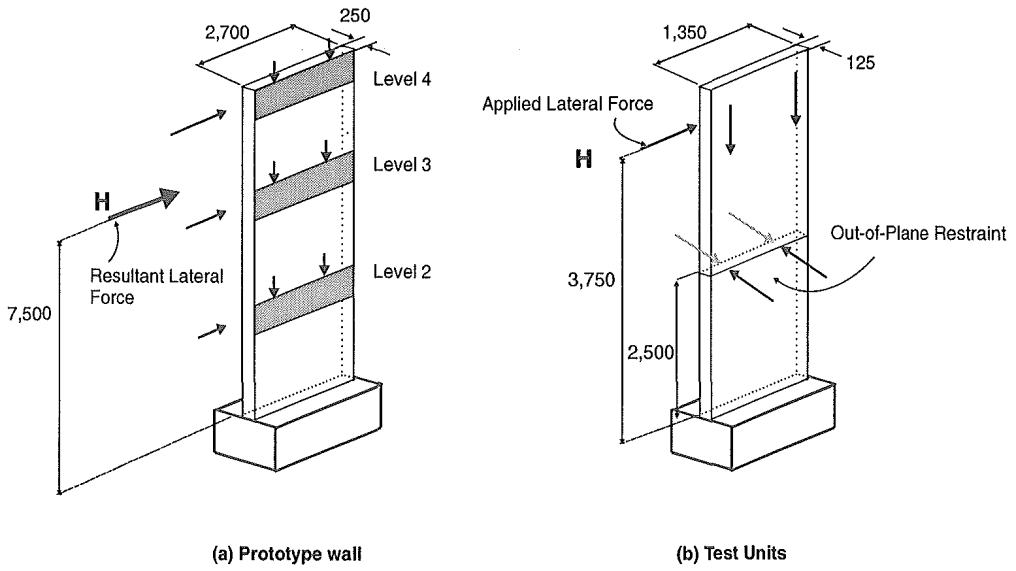

Figure 2.1 Basic geometry of test specimens.

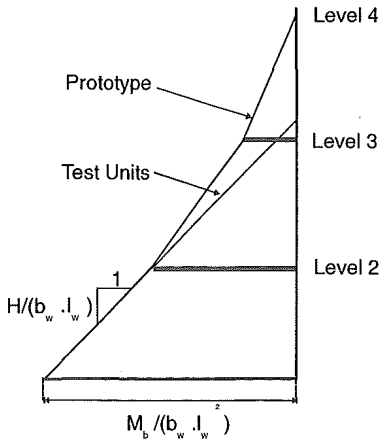

Figure 2.2 Normalised bending moment.

The first specimen tested, Unit 1, was a precast concrete structural wall designed following the Concrete Structures Standard (NZS 3101, 1995) recommendations for monolithic ductile walls. The main objectives for testing this unit were,

1. To provide a benchmark to compare the seismic behaviour of hybrid wall systems with that obtained from equivalent monolithic wall systems.

2. To observe the cumulative development of damage and residual displacements in the wall with increased lateral displacement levels.

3. To evaluate the performance of the wall-foundation connection which is vital for the performance of the unit as an equivalent monolithic system.

The second specimen tested, Unit 2, was a prestressed hybrid wall incorporating carbon fibre prestressing tendons, steel-fibre reinforced concrete, and steel energy dissipators. This unit was similar to a hybrid unit tested by Rahman and Restrepo (2000).

In the early conception of this research project it was decided that the simplest option of designing and constructing each unit would be to cast the foundations and walls separately.

According to the Concrete Structures Standard, Unit 1, was expected to have displacement ductility capacity of at least five. Unit 2 was explicitly designed to reach a roof drift ratio of at least 2.0%.

The aspect ratio of both walls measured from the base to the point of application of the horizontal force was, $A_r=H_w/l_w = 2.77$, the height-to-width ratio was, $H_w/b_w = 30$, where H_w is the height of the wall to the point of application of the lateral force and b_w is the width of the wall.

The specified concrete compressive strength for the wall panels and foundation beams was, f'_c = 40MPa. A maximum aggregate size of 10mm and slump of 120mm was specified for Unit 1. Both specimens were designed incorporating standard Grade 430 longitudinal reinforcement (HD), Grade 300 transverse reinforcement (R). Grade 500

steel, in the way of threaded reinforcing bars, was used to connect the wall panel and the foundation beam in Unit 1. The grade of the reinforcement in New Zealand refers to the 5% lower characteristic yield strength.

2.2 DESCRIPTION OF UNIT 1

2.2.1 Wall Panel Design

This unit was designed for ductile response in accordance with the requirements of the Concrete Structures Standard (NZS 3101, 1995). Using capacity design principles, an inelastic mechanism involving the development of a flexural plastic hinge at the base of the wall was chosen. The potential plastic hinge region was detailed for full ductility. Other regions in the unit were designed to remain elastic.

It was found during design of Unit 1 that several of the minimum requirements in the Concrete Structures Standard controlled the design. Examples of such limitations include minimum spacing between longitudinal bars, minimum longitudinal steel ratios and transverse bar spacings, particularly in the confinement region and potential plastic hinge zone (PPHZ). Because of minimum requirements concerning the spacing between longitudinal bars and the impossibility of sourcing small bar sizes, the strength of Unit 1 was calculated to be approximately 30% greater than that attained by Unit 3 tested by (Rahman and Restrepo, 2000), which was taken as a control unit.

Given that the primary objective of Unit 1 was to compare the behaviour of a conventionally designed wall to that of Unit 2 as well as previously tested post-tensioned hybrid walls, the requirements of the standard were strictly adhered to. No attempt was made to curb the capacity of Unit 1 by ignoring or overruling clauses.

The reinforcement layout of Unit 1 is illustrated in Figures 2.3 to 2.5. The ducting positions indicated correspond to those ducts placed in the foundation beam.

The Concrete Structures Standard did not require boundary elements for Unit 1, but did require provisions to be made for confinement of the concrete and anti-buckling of the longitudinal bars within the PPHZ. As a result, there was a concentration of

longitudinal reinforcement in the PPHZ at the wall ends and a concentration of transverse reinforcement, at the ends near the base of the wall. As shown in Figure 2.3 to Figure 2.5, Grade 430 – HD10 bars were used as longitudinal reinforcement and Grade 300 - R6 bars were used as transverse reinforcement. The longitudinal and transverse reinforcement ratios for this unit were p_e =0.84%, and p_v =0.25%, respectively. The longitudinal reinforcement ratios at the wall ends and at the centre were p_l=1.26% and p_l=0.57%, respectively. The volumetric confinement reinforcement ratio at the wall ends was p_s=1.90%.

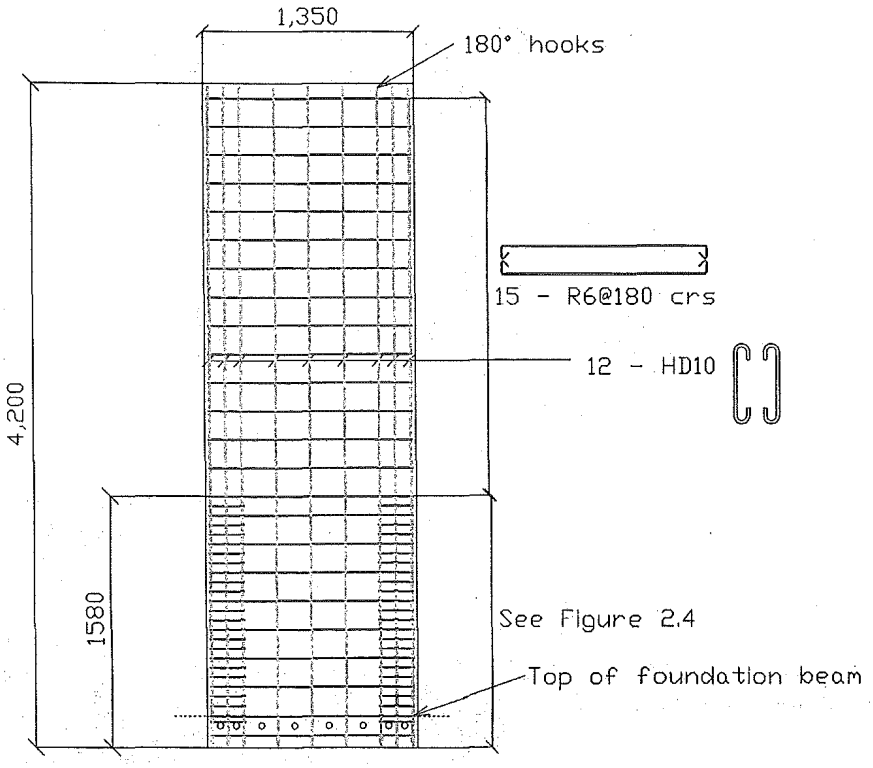

Figure 2.3 Unit 1 reinforcement layout.

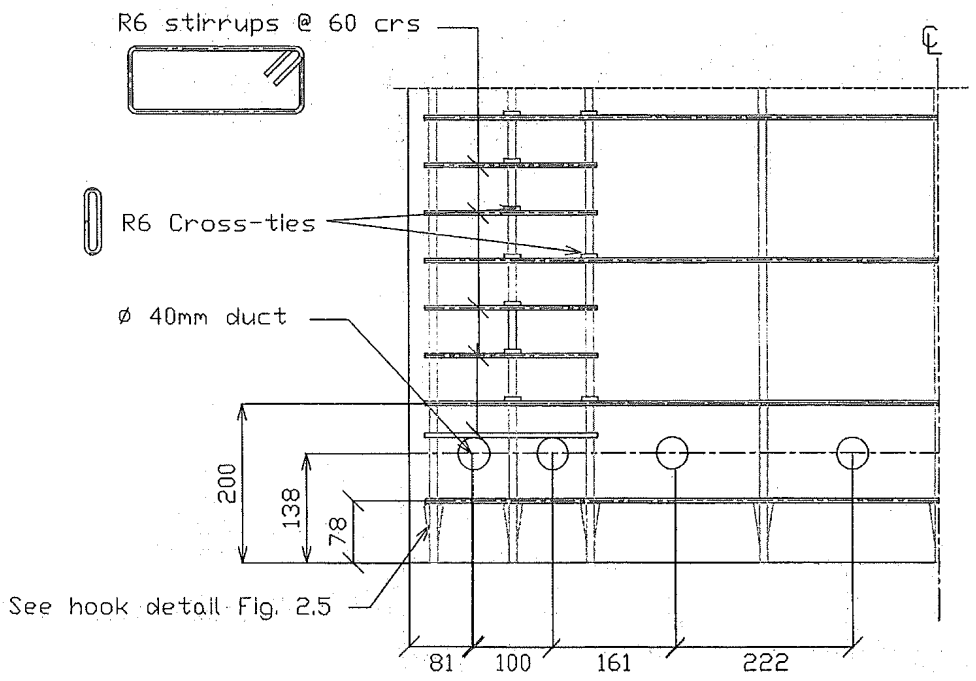

Figure 2.4 Detail of duct and stirrup layout.

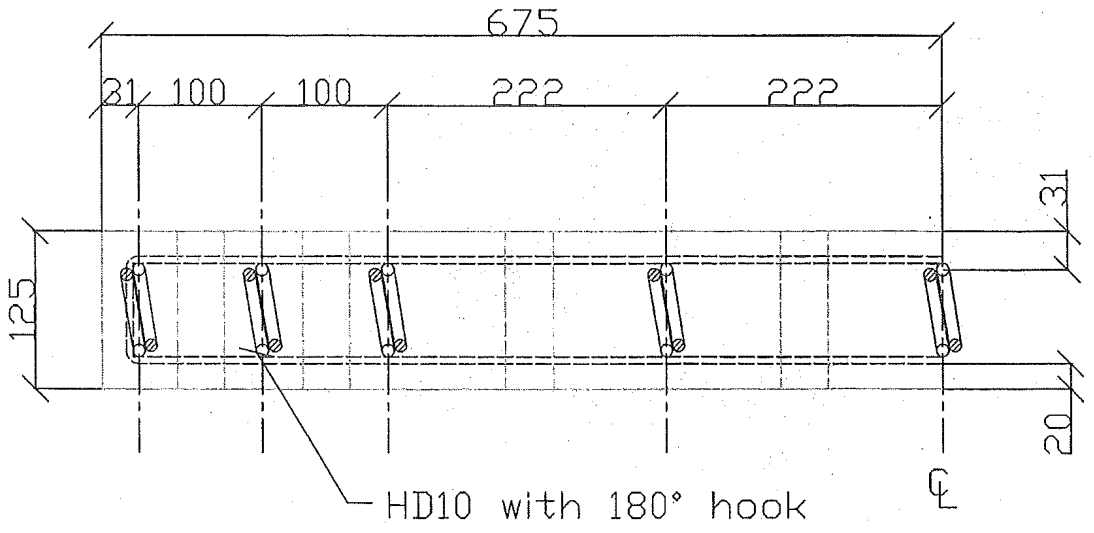

KEY

⌀ Hook Extension

O Longitudinal bar

Figure 2.5 Cross-section showing longitudinal reinforcing layout.

Not shown in the above reinforcement layouts are the attachments and connection plates to which the lateral and axial loads were applied. These details are explained in section 3.

2.2.2 Foundation Beam Design

Actions for the foundation beam were obtained from the flexural over-strength that was expected to develop at the wall base. These over-strengths were determined from a moment-curvature analysis of the section using $\bar{f}_y$ = 460 MPa as the average yield strength of the Grade 430 reinforcing steel as well as allowing for strain hardening effects. The longitudinal and transverse reinforcement in the beam were designed for the largest bending moment and shear force. That is, no attempt was made to curtail the longitudinal reinforcement nor to change the spacing of the stirrups. As will be explained later, the amount of transverse reinforcement provided in the foundation beam was controlled by the transfer mechanism that allowed for a shallow anchorage of the wall into the foundation beam.

Height restrictions imposed by the crane located within the laboratory eliminated the use of starter bars to connect Unit 1 with the foundation beam. It was concluded that a recess be made in the foundation within which the wall would eventually sit. Such a connection detail has been used in the past in New Zealand, (CAE, 2000). A minimum recess depth was calculated from the basic deformed bar development length for hooked bars in tension given by the Concrete Structures Standard (NZS 3101, 1995). In this way the longitudinal bars running the length of Unit 1 would essentially act as starter bars, provided that the grout used to hold the wall within the recess supplied sufficient shear resistance. The depth of this recess was also restricted by limitations imposed by the crane, where the height of the wall plus the recess depth approached the crane's height limit.

Calculations at this stage showed that shear transfer through cohesion alone would not be sufficient to reliably transfer wall actions into the foundation. To ensure that Unit 1 acted essentially as a monolithic cantilever, Grade 500 threaded bars were utilised. These bars ran horizontally within ducting through the foundation, into the wall, and back into the foundation. Circular 40mm diameter steel ducting was used through which 16mm threaded bars were subsequently grouted. A schematic diagram of this system is shown in Figure 2.6.

The threaded bars equilibrate the horizontal component of the struts formed when the wall is subjected to a lateral loading. Stirrups specially placed within the foundation, that are superfluous to the shear design, take up the vertical component of these struts. Figure 2.7 shows the transfer of these forces. Note that for this strut-and-tie model to work, it must be ensured that a shear failure does not occur at any of the grouted concrete interfaces. For this reason 2mm amplitude roughening was specified for both the wall panel and within the foundation beam recess. The 2mm amplitude is the result of approximately scaling the 5mm roughening which would normally be specified for the full-scale prototype.

The magnitude of the "pull-out" force was based on the ultimate strength of each of the longitudinal bars within Unit 1. As can be seen from Figure 2.8 each threaded bar was placed essentially half way between adjacent longitudinal bars. In this way under ultimate load each threaded bar would carry identical forces. This allowed the same size threaded bar and number of stirrups to be used throughout the interface of shear transfer. Figure 2.9 illustrates the design actions and corresponding reinforcing layout of the foundation beam for Unit 1.

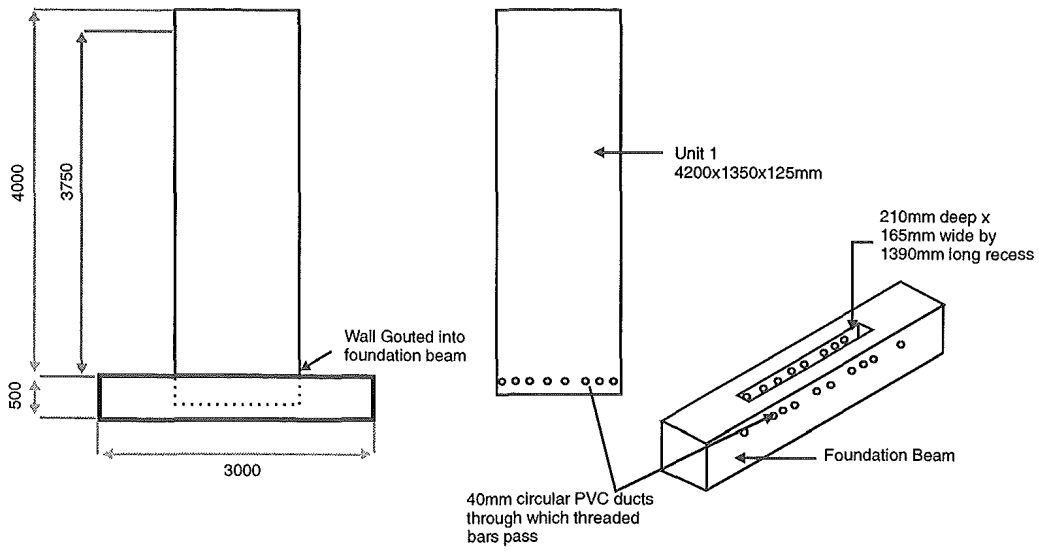

Figure 2.6 Unit 1 connection detail.

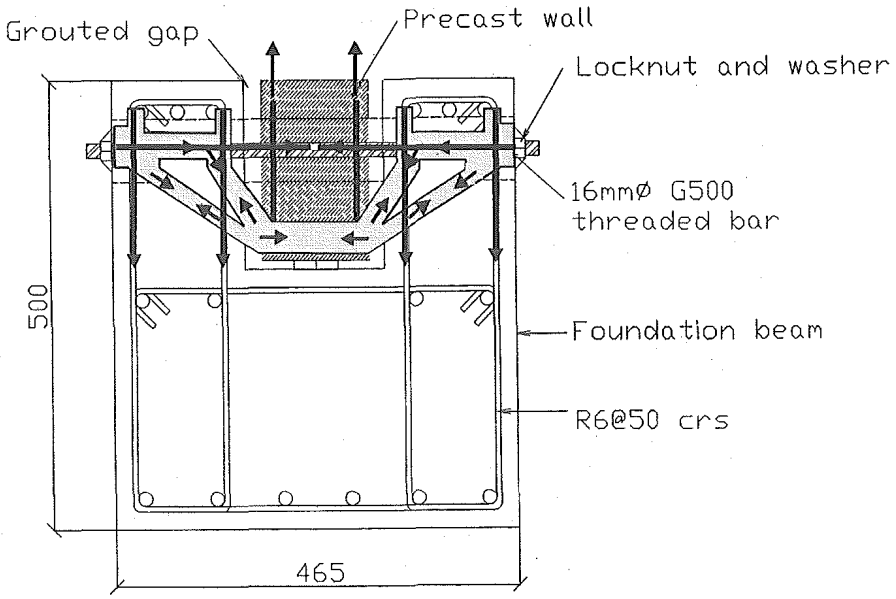

Figure 2.7 Wall panel-foundation beam internal force-flow in the transverse direction.

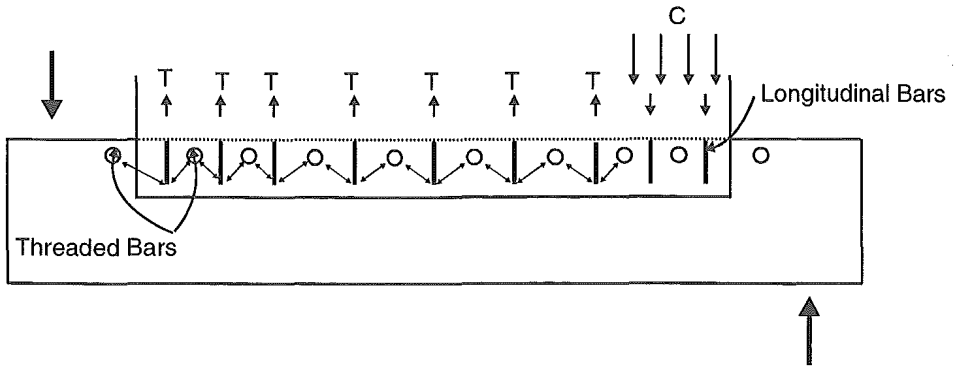

Figure 2.8 Wall panel–foundation beam internal force-flow in the longitudinal direction.

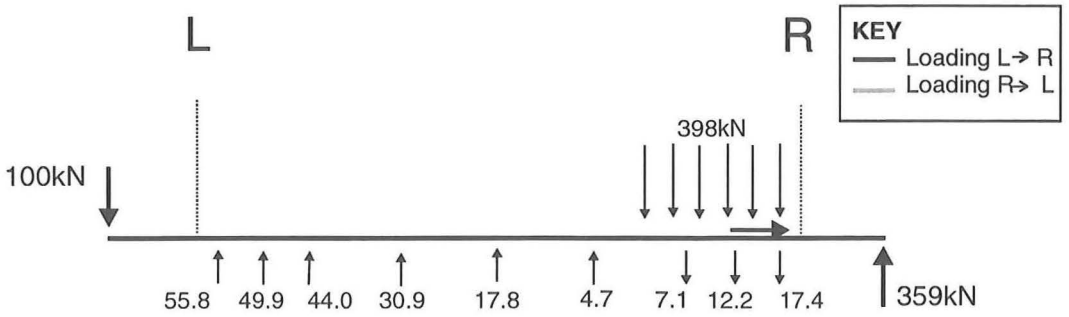

(a) Design actions (lateral force acting left to right)

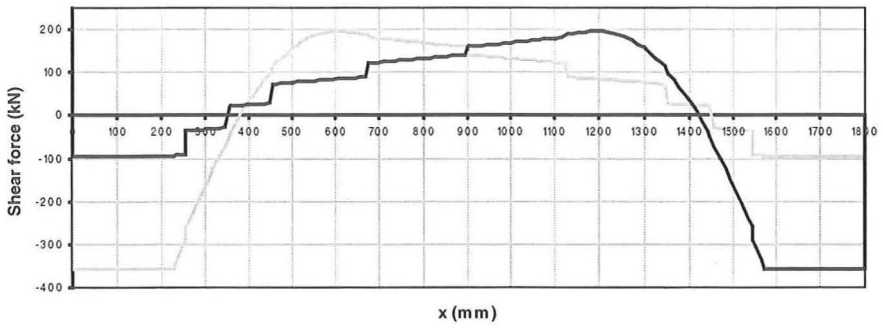

(b) Shear Force Diagram

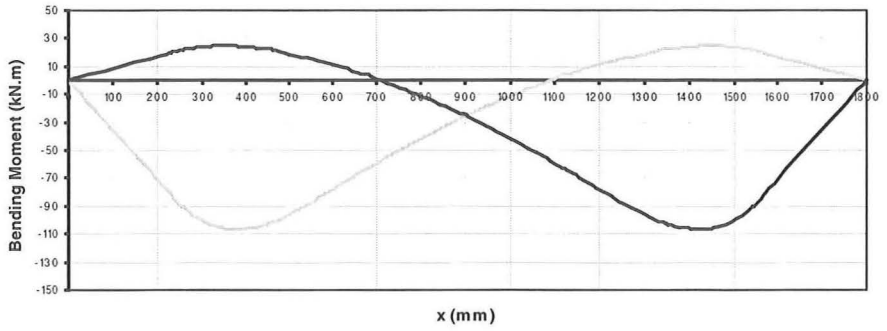

(c) Bending Moment Diagram

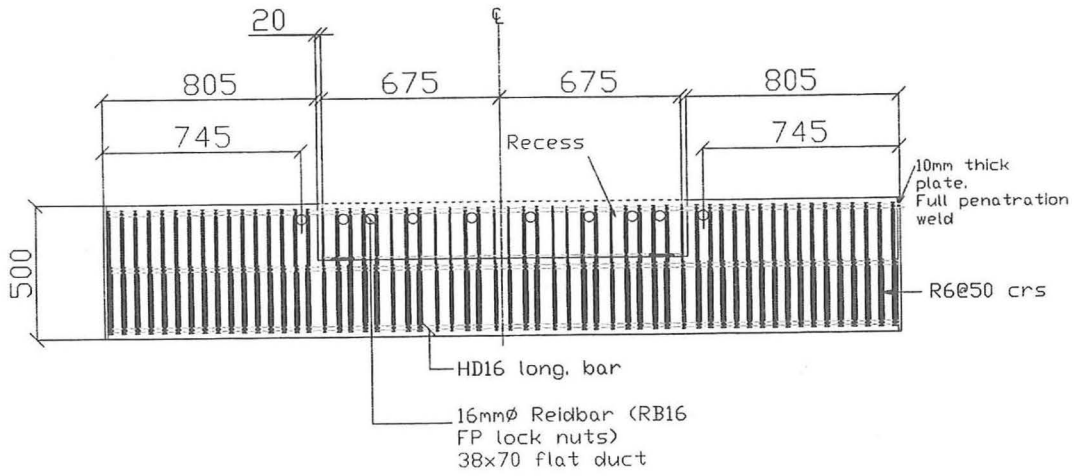

Figure 2.9 Design actions and reinforcement layout of foundation beam for Unit 1.

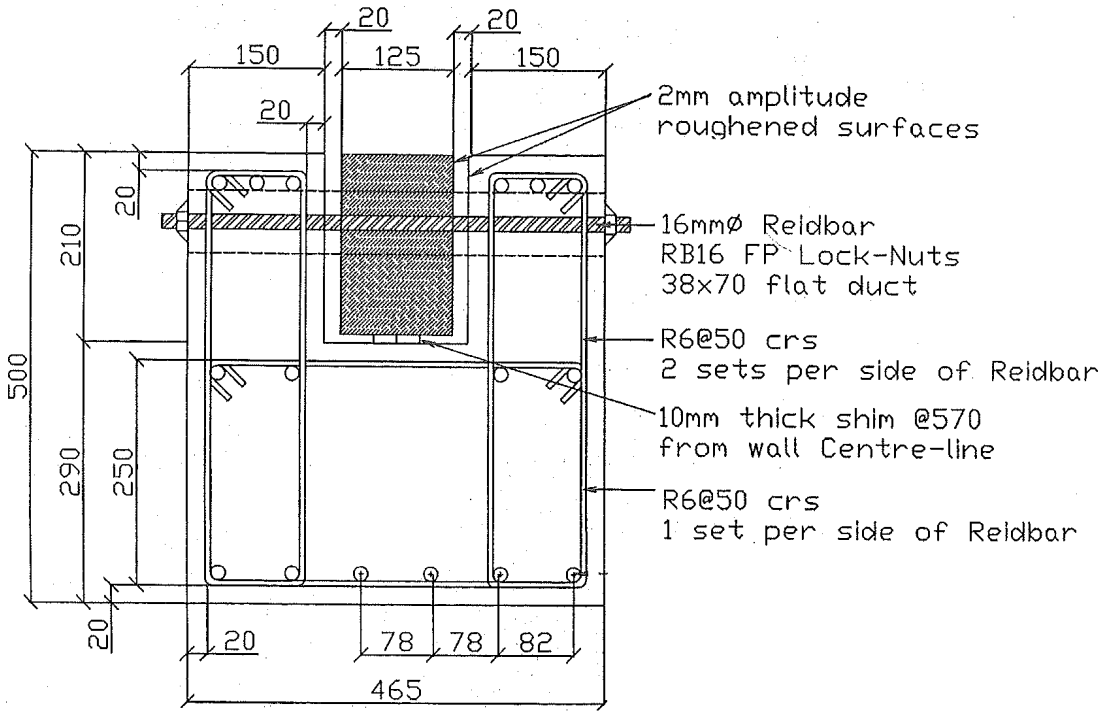

(a) Cross-section through recess

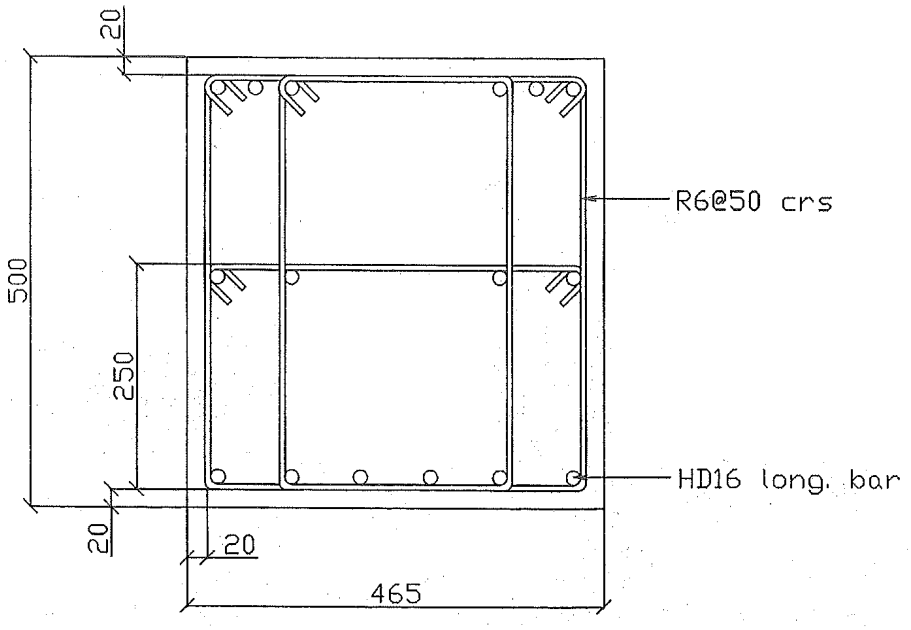

(b) Cross-section outside recess

Figure 2.10 Cross-sectional details of the foundation beam for Unit 1.

2.2.3 Construction

Construction began with the fabrication of the foundation beam. The HD16 longitudinal bars were initially welded to a 10mm thick baseplate with R6 transverse reinforcement hoops added and spaced accordingly. Once the transverse hoops had been fed on, spaced, and sufficiently tied into place the remaining baseplate was tack-welded into position. At this stage the ducting was located and tied into position. Much care was taken over the position of these ducts as small tolerances were required in order to successfully pass the threaded bars through the wall. Figure 2.11 shows the completed cage during a final check on the spacing and location of the ducting.

A collapsible box was made that would create the required recess once the concrete was cast. Figure 2.12 shows the foundation beam just prior to casting. The beam was cast upside-down in order to help position the recess. The collapsible box used to form this recess can be clearly seen.

Figure 2.11 Completed cage of the foundation beam for Unit 1.

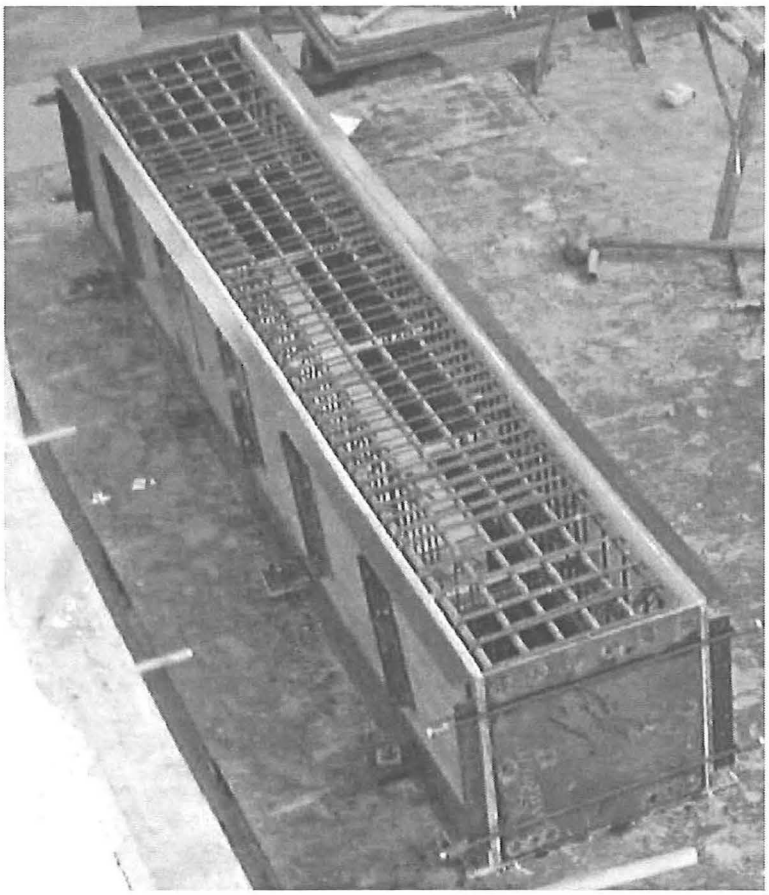

Figure 2.12 Unit 1 foundation beam showing wall recess.

Casting of the foundation beam and subsequent casting of the other units was performed on a steel casting bed. Testing was performed within an adjoining laboratory requiring that the specimens be transported by flat bed truck and craned into their final positions.

Figure 2.13 shows the wall panel mid way through the steel tying operation. Note the closer stirrup spacing within the confinement region of the PPHZ as well as the extra stirrups and longitudinal reinforcement provided for anti-buckling purposes at the ends of the wall. The central longitudinal reinforcement has yet to be threaded and tied into position.

Figure 2.14 shows Unit 1 just prior to the casting operation. Illustrated are the braces holding in position the ducting and lifting anchors. Prior to placing the cage onto the casting bed strain gauges were placed on both external most longitudinal bars, a description of which is provided in section 3.3.4.

As with the foundation beam, close attention was placed on correctly locating the ducting through which the horizontal threaded bars were to be fed through. Special braces were made to locate these ducts as well as to prevent them from moving during the casting operation. Similar braces were made for the ducts used for bolting the external brackets, which applied axial load, to the wall.

Unit 1 and its corresponding foundation beam were cast together on the steel casting bed. A retarding agent was sprayed on the bed to prevent the concrete from bonding to the deck while curing.

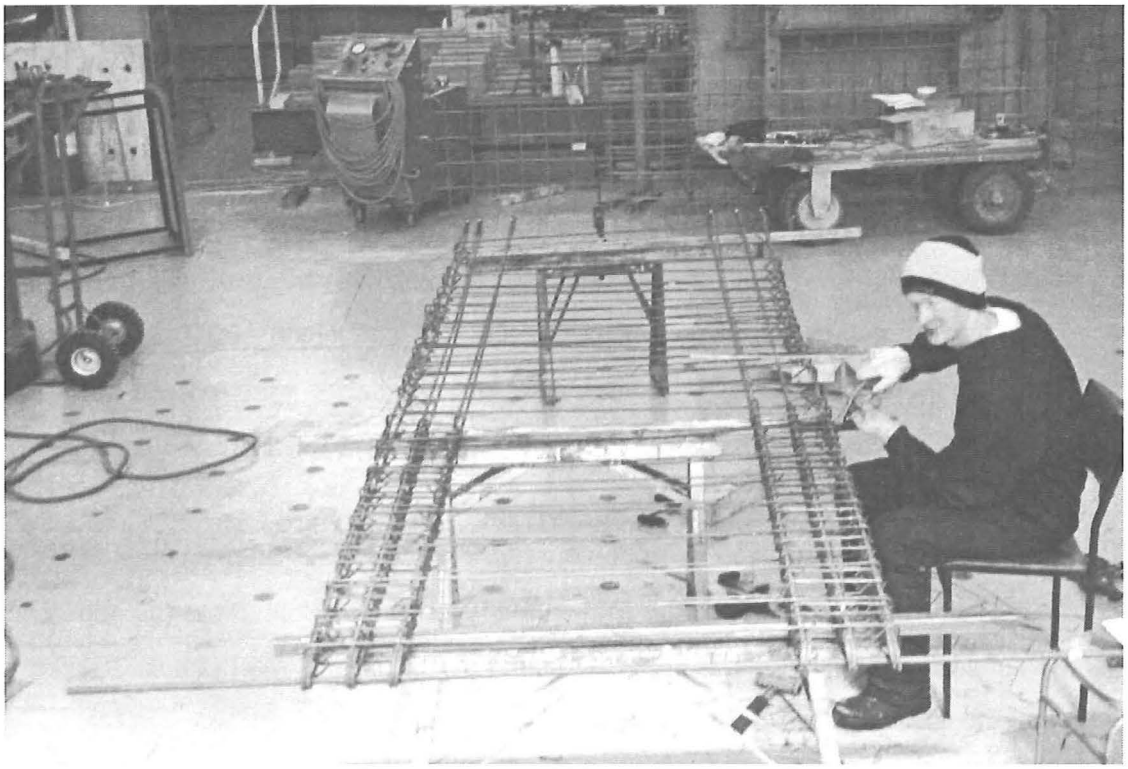

Figure 2.13 Reinforcing cage of the wall for Unit 1 mid-way through the steel tying operation.

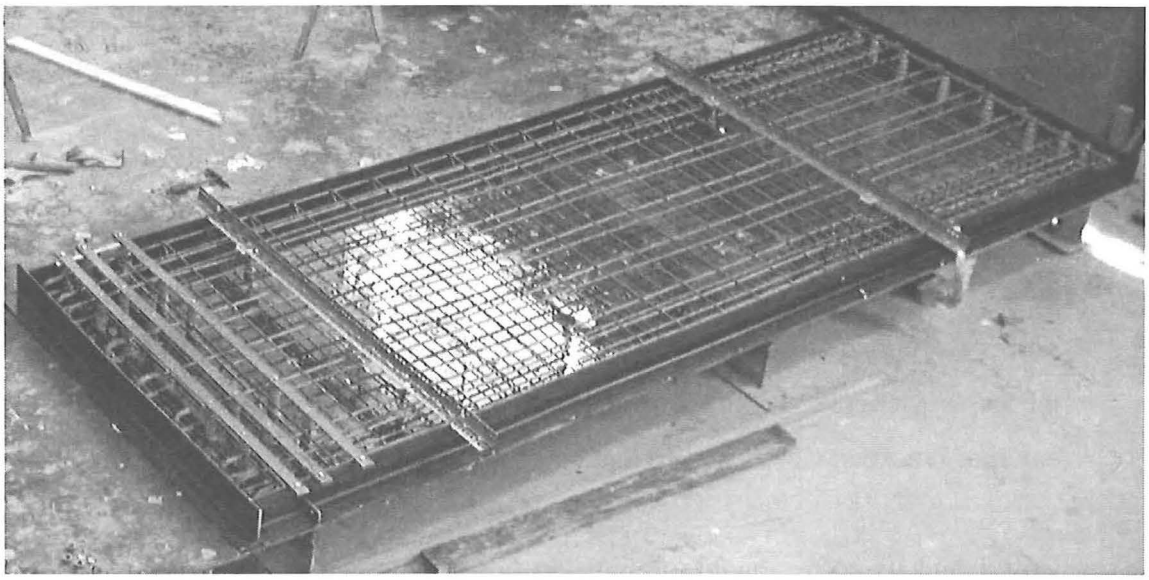

Figure 2.14 Wall panel of Unit 1.

Concrete was specified to have a cylinder strength of f'_c = 40 MPa with a slump between 100-120mm and maximum aggregate size of 10mm. On arrival slump tests were performed on the mix, which revealed a 80mm slump. Superplasticiser was added to increase the workability of the mix, eventually providing a very workable 110mm slump concrete. Concrete vibrators were used to ensure no voids were entrapped within the specimens. Wooden floats were used to level both the wall and foundation, with steel finishing floats used once the concrete had sufficiently bled and set. Once the concrete had sufficiently hardened, wet hessian sacks were placed on top of the specimens and covered with plastic sheeting for 12 days to ensure proper curing.

The foundation beam was stripped of its formwork 5 days after casting and lifted into position. Figure 2.15 shows the foundation beam in position. Note the gap beneath the beam where the specimen is supported by two 10mm thick steel plates. The recess cast into the unit can also be clearly seen.

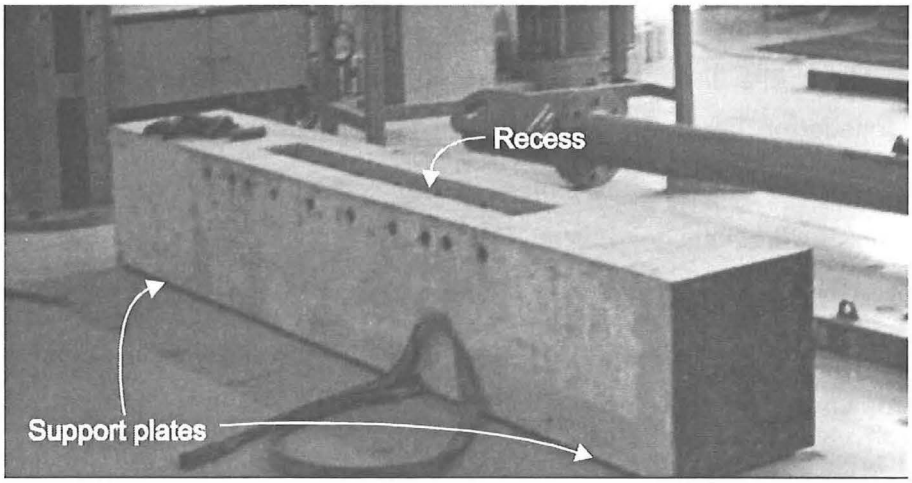

Figure 2.15 Unit 1 foundation beam showing cast in recess.

Care was required during the lifting operation of the wall panel to avoid cracking. Four lifting anchors were cast into in the face of the wall allowing it to be loaded horizontally onto a flat bed truck for transportation to the testing laboratory. The suction between the bed and the wall was overcome through initially lifting the wall from the top two lifting eyes only.

Prior to lifting the wall panel, concrete cylinder tests were performed to ensure that the concrete had obtained sufficient strength to prevent cracking of the specimen. Tests revealed that both the wall and foundation beam had an average compressive strength of 39.5 MPa after 9 days. This was higher than expected given that the 28 day strength specified was 40MPa.

Both the recess and the wall panel were mechanically roughened prior to the wall panel being placed within the recess. The wall panel was seated on two 10mm thick steel plates placed on the bottom of the recess. The plates left a gap that let the grout flow beneath the wall during the grouting operation. Having checked that all the ducts lined up, the threaded bars were passed through and locked into place using washers and locknuts. At this stage the wall for safety reasons required an out of plane lateral support which was provided thorough restraining beams on the test rig (refer to section 3.1).

Figure 2.16 shows Unit 1 shortly after the completion of the lifting operation. Steel sections holding the foundation beam to the strong floor can be seen. These prevented the foundation beam from lifting once lateral loading was applied to the wall panel. The plate to which the hydraulic ram connects as well as the ducts through which the prestressing brackets bolt can also be seen.

Grouting of the recess was the final step in the construction of Unit 1 prior to the instrumentation being placed. The grout utilised was Conbextra GP. Bleed holes were drilled at the ends of the ducts to prevent the entrapment of air. The grout was poured from the top of the recess down the sides of the wall. Wet hessian sacking was placed on top of the grouted joint and left there for 3 days. Figure 2.17 shows the last stages of the grouting operation. The bleed holes are clearly visible on top of the foundation beam.

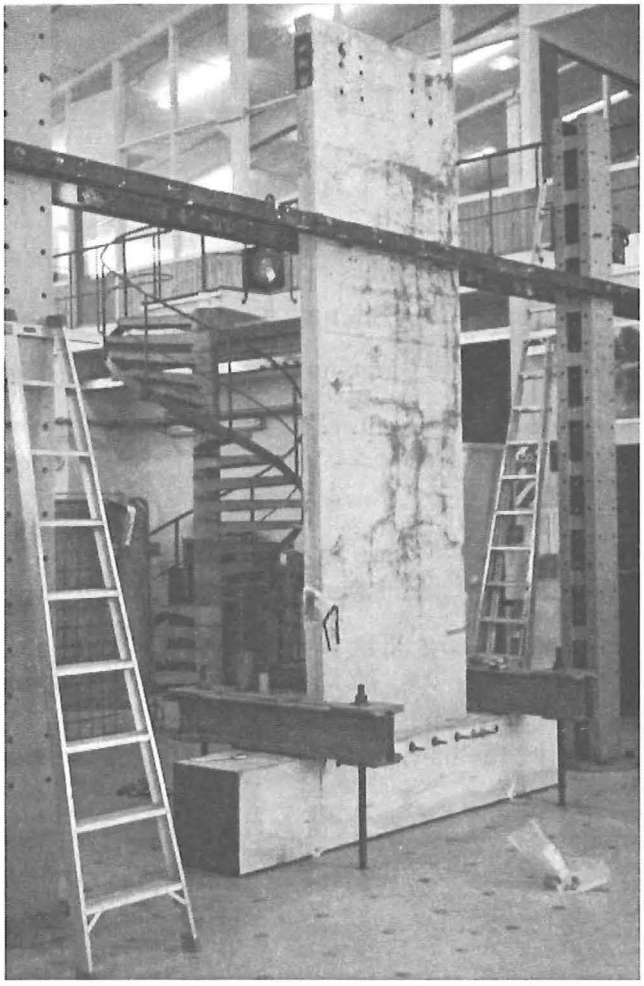

Figure 2.16 Unit 1 fully erected.

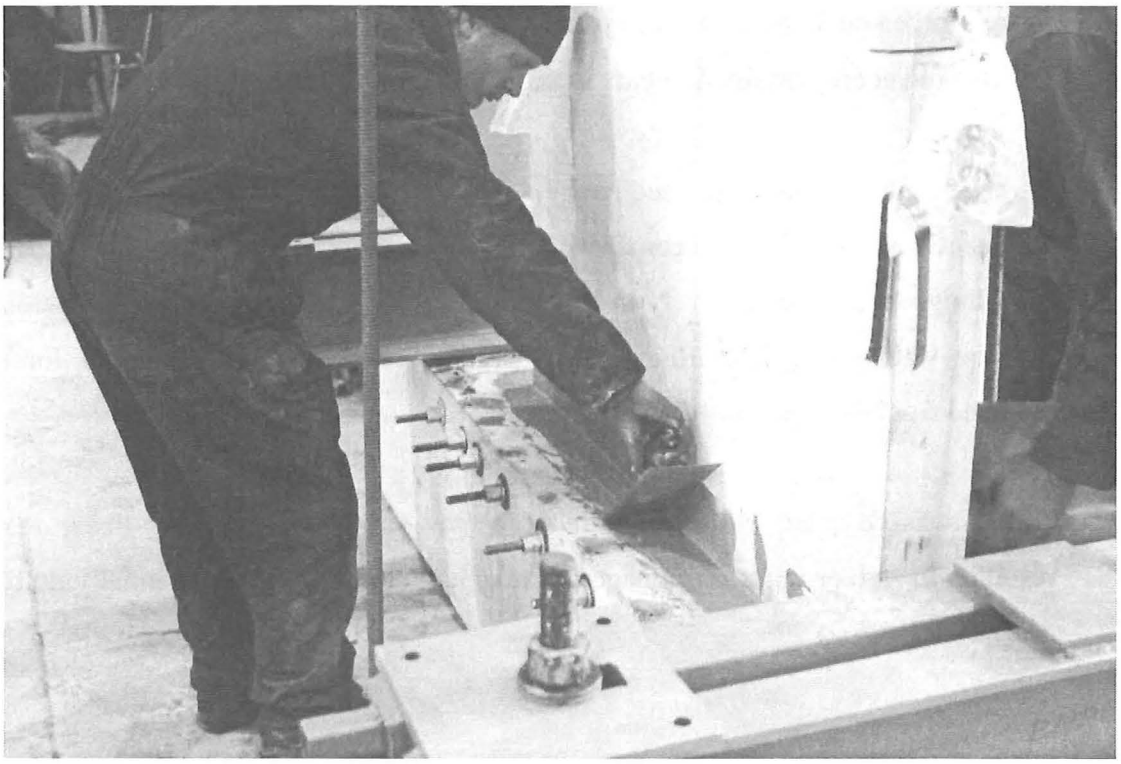

Figure 2.17 Finishing of grout prior to addition of wet hessian sacking.

2.3 DESCRIPTION OF UNIT 2

2.3.1 General

Unit 2 incorporated a number of new design ideas and philosophies not utilised in conventional seismic design. Features of Unit 2 included the use of,

- Carbon fibre prestressing tendons,
- Steel-fibre reinforced concrete for improved crack control, and ease of the reinforcement cage in the wall panel.
- Tapered energy dissipating bars to provide hysteretic damping.

No code requirements were used in the design of Unit 2. First principles were utilised to ensure the lateral displacement chosen for design was achieved. Strut-and-tie modelling was used extensively in the design and analysis of both the foundation beam and the wall panel. Reinforcing was placed according to the internal force flow obtained from the strut-and-tie model developed.

Unit 2 was designed with the main objectives of obtaining a non-linear response, resulting in zero or minimal damage to the unit, and in achieving essentially no residual drift.

2.3.2 Wall Panel Design

In the design of Unit 2 the following criteria were considered:

- To remain undamaged under 2.0% lateral displacement,
- to self-centre after cyclic loading,
- to provide a satisfactory level of hysteretic damping,
- to be cost comparable will conventional construction systems.

The basic design of Unit 2 was relatively straight forward, the particular system developed is outlined further in section 2.3.2.1.

In detailing Unit 2 it was intended that the reinforcing cage could be manufactured as two independent units (an upper and lower portion), requiring only to be brought together at the commencement of casting. The lower portion it was envisaged could be constructed and hot-dip galvanised within a precast type facility, and later spliced to the upper portion which could be constructed at the same location or on site.

The lower portion of the reinforcement cage contains a significant amount of welding. Therefore, construction within a precast facility is ideal given better quality control than that provided on site, as well as the specialist equipment such as galvanising baths that can be facilitated. For multiple units these benefits are further increased.

A steel fibre reinforced concrete mix was utilised in order to provide better crack control, particularly in areas of little of no reinforcement. "Dramix" steel fibres (RC-65/35-BN) (40kg/m^3) were added to the concrete mix design that specified a 28 day strength of 40MPa and maximum 13mm aggregate size. The dosage of fibres was taken from that utilised by Whiteside (2000) in his research into thin wall units.

The reinforcing layout developed is far from the conventional reinforcing schemes that comply with today's design standard. Emphasis was placed on carrying the design level of 2.0% lateral drift through well established internal force flows. This method significantly cut down the amount of steel reinforcement necessary, as well as reducing the level of detailing required particularly at the base of the wall. This reduction in the detailing is also a product of the hybrid system, where the non-linear elastic deformations are provided by the opening of the joint at the wall base rather than through plastic deformations occurring within the wall panel itself.

Two ducts each containing three 5.5mm diameter carbon fibre tendons provided the prestressing for Unit 2. These tendons behave elastically up until failure as well as being resistant to corrosion. This benefit has greater implications for systems incorporating similar ideas in marine type environments.

To provide a reasonable level of hysteretic damping tapered, steel bars were incorporated at the wall panel-foundation beam connection. These tapered longitudinal bars act as a fuse connection between the wall and the foundation, as shown by Rahman

and Restrepo (2000). Yielding of these bars dissipates energy and reduces the walls' response to excitation. The design and requirements of these tapered bars is further outlined in section 2.3.2.2. The energy dissipation bars were partially grouted within a SHS cast into the wall unit. Forces developed within these bars were transferred though bond to the SHS's, which intersected with diagonal reinforcement, that equilibrated these tensile and compression forces back to the base of the wall. A clearer description of the internal force flows is given in section 2.3.2.1.

The initial level of prestressing, in the carbon fibre tendons was $0.46f_{pu}$, where f_{pu} is the tendon's ultimate tensile strength. This level of prestress was calculated in order to keep the induced stress, due to rocking, under $0.85f_{pu}$ at 2.5% lateral drift. An additional requirement of the post-tensioning force was to ensure that, in conjunction with the externally applied axial load, that these forces were great enough to yield the tapered dissipating bars once the lateral force was removed, (Rahman and Restrepo, 2000). Provided that the combined post-tensioning and the externally applied axial load is greater than the force required to compress the dissipators back to their original geometry the joint between the wall and foundation beam will essentially close upon the removal of the lateral load. Conversely, the greater the level of prestressing the larger the dissipating devices that can be used, thus maintaining a relatively constant damping level in the system. The reinforcement layout of Unit 2 is illustrated in Figures 2.18 to 2.21.

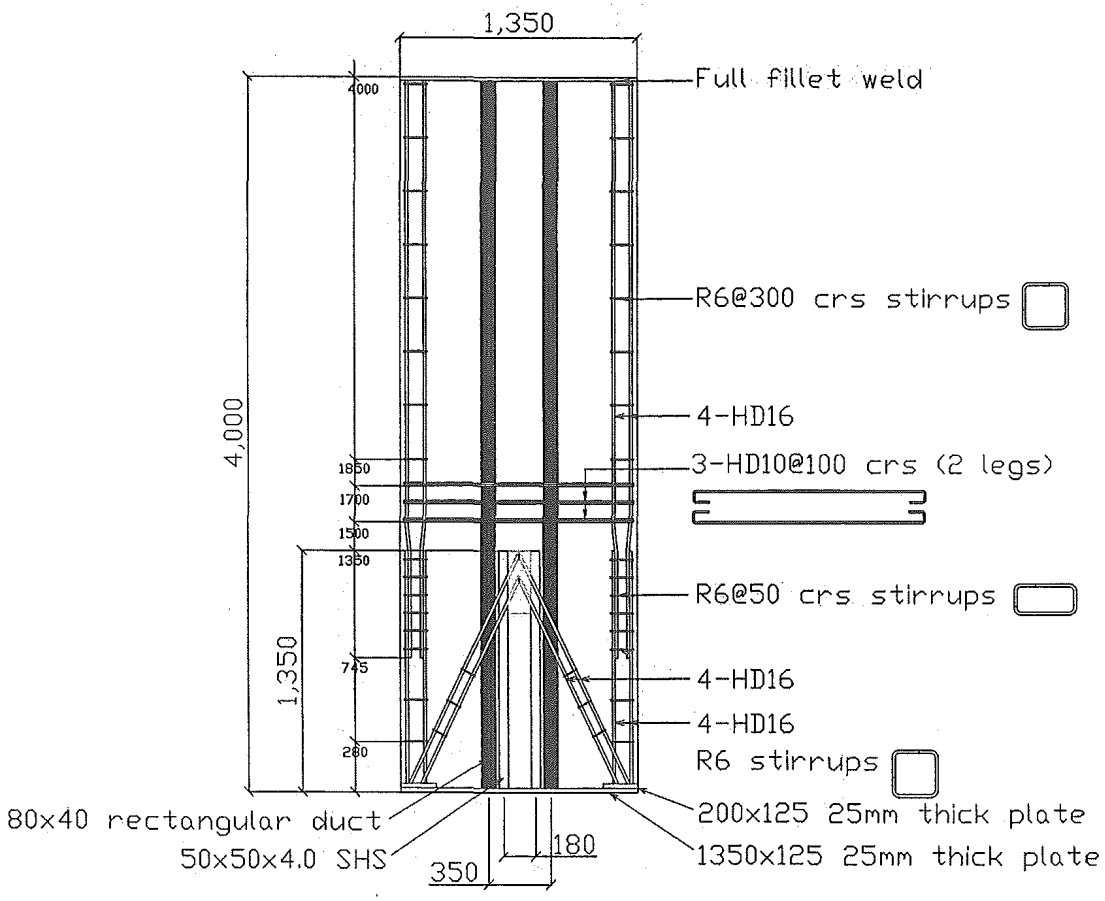

Note: All stirrups have 90 hooks.

Figure 2.18 Wall panel reinforcement layout in Unit 2.

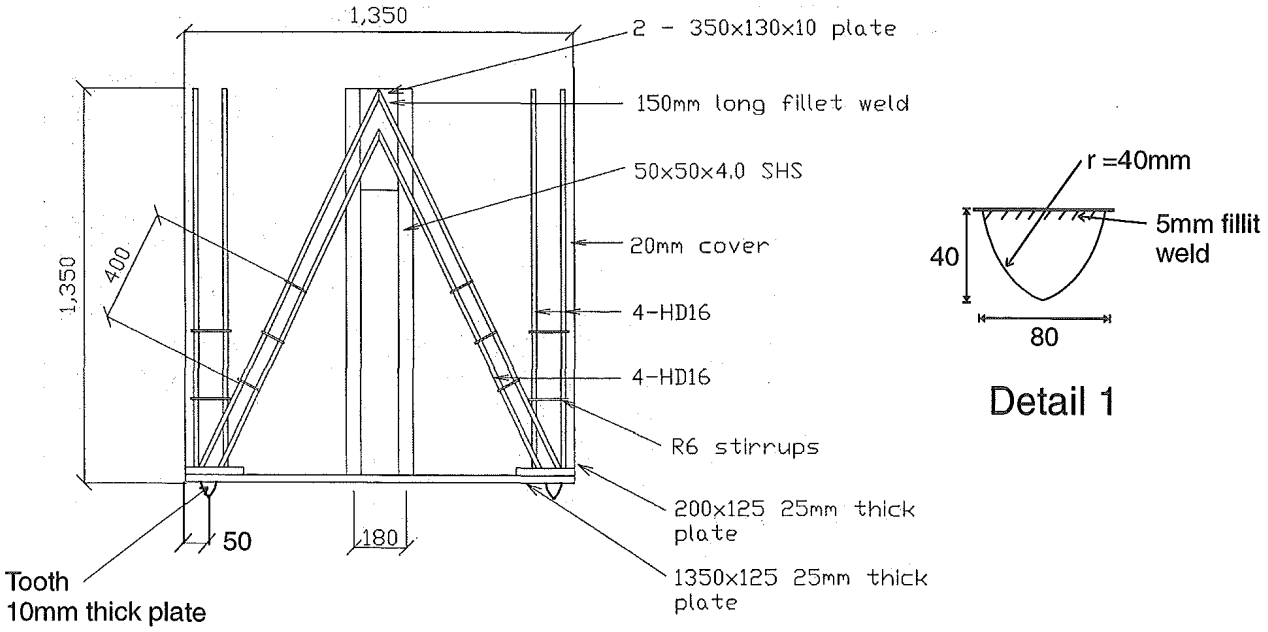

See Detail 1

Figure 2.19 Detail of lower segment of the wall panel of Unit 2.

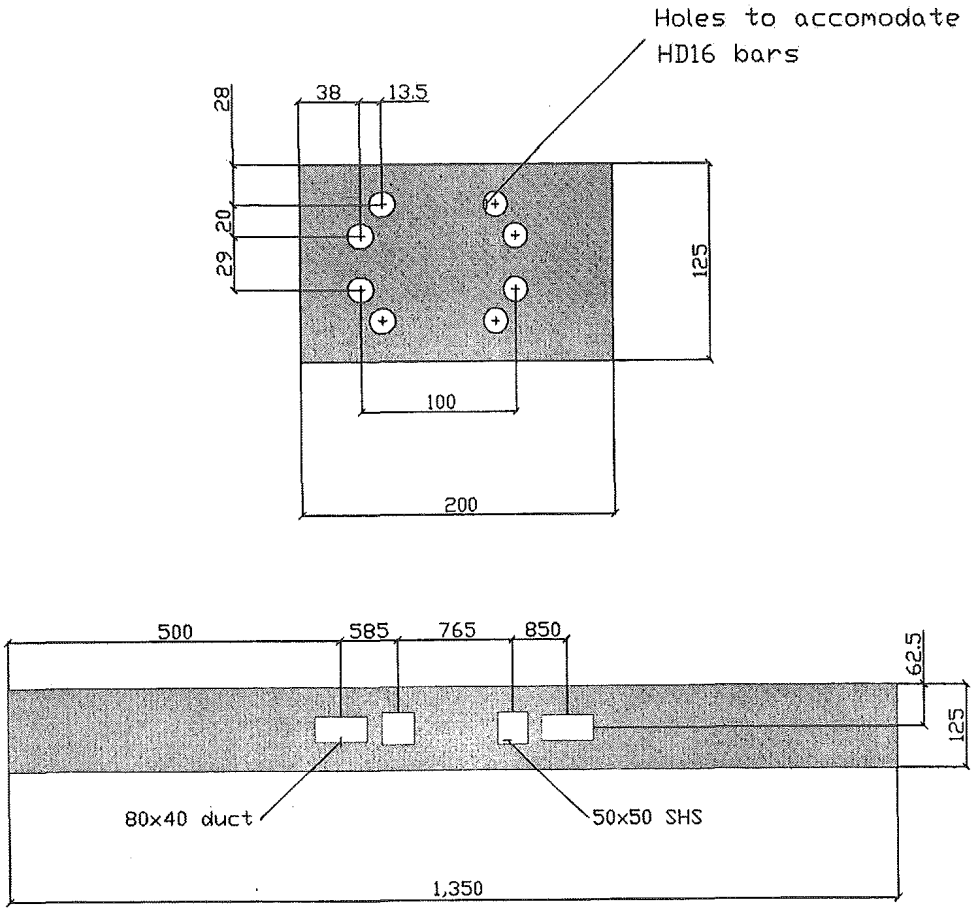

Figure 2.20 Bottom plate detail for the wall panel of Unit 2.

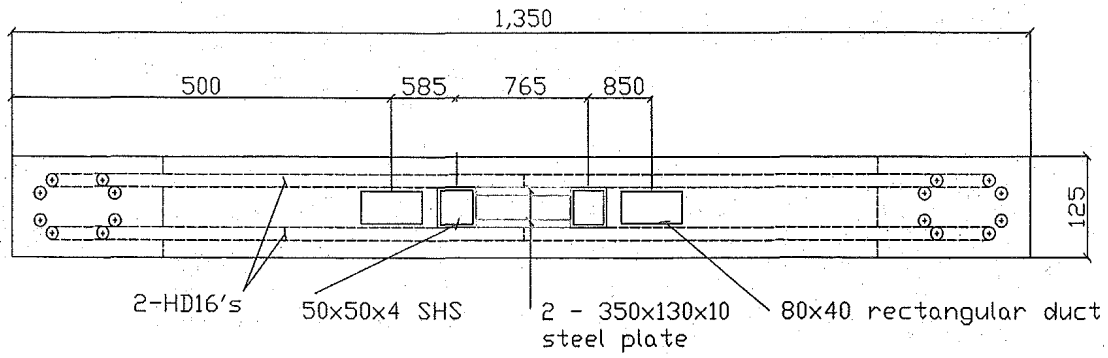

Figure 2.21 Cross-section showing diagonal and longitudinal reinforcing layout.

2.3.2.1 Internal force flow analysis

The flow of internal forces within the wall panel of Unit 2 at the maximum level of drift was obtained using strut-and-tie modelling. It was assumed that the internal force flow results from two independent and additive mechanisms.

- **Rocking Mechanism** - Equilibrating the lateral force component due to the applied axial load plus the panels self weight.

- **Bond Mechanism** - Equilibrating the lateral force component resulting from the development of the ultimate tensile strength of the dissipators.

The force flow of these components is illustrated Figure 2.22.

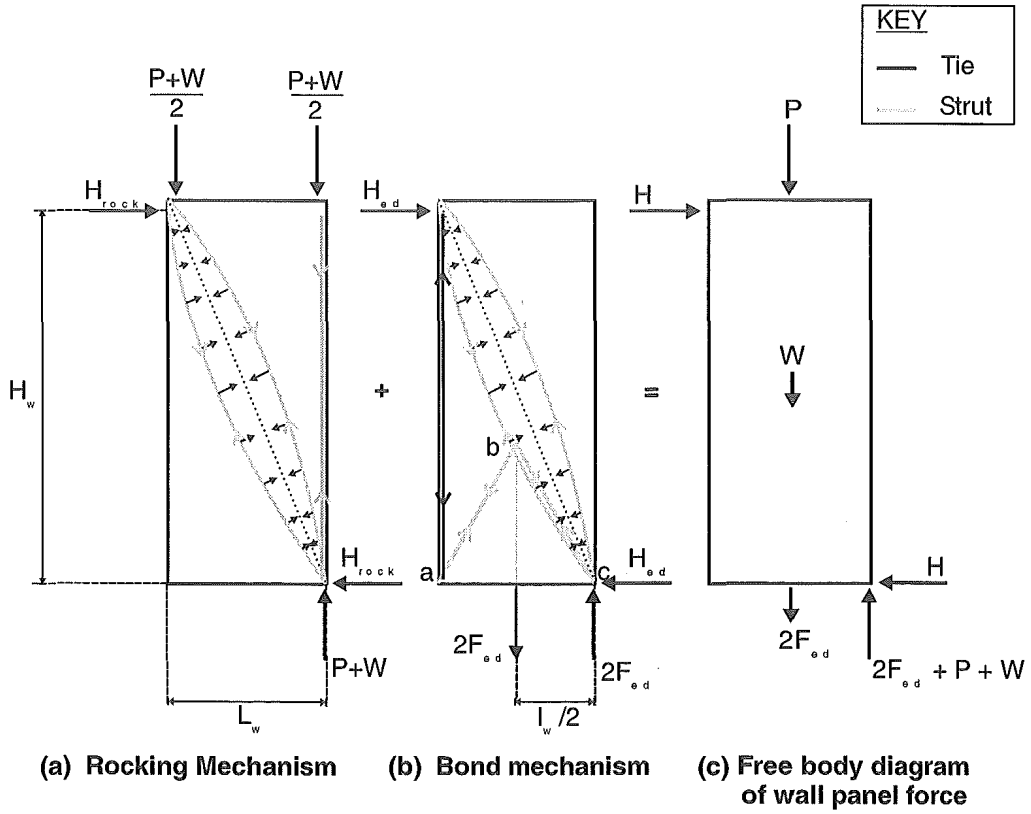

Figure 2.22 Internal force flow of the rocking and bond components of lateral force.

Anchorage at all joints was provided though welded connections. These being between the longitudinal steel and the top and bottom steel plates, as well to steel plates at the node connection between the diagonal reinforcement bars. From the mechanisms illustrated, the lateral forces H_{rock}, H_{ed} and, thus, H can be calculated.

$$H_{rock} = \frac{l_w}{H_w}\left(\frac{P+W}{2}\right) \qquad (2.1)$$

$$H_{ed} = F_{ed}\left(\frac{l_w}{H_w}\right) \qquad (2.2)$$

$$H = H_{rock} + H_{ed}$$

$$H = \left(\frac{l_w}{H_w}\right)\left(\frac{P+W}{2} + F_{ed}\right) \qquad (2.3)$$

For simplicity the location of the resulting forces at the wall end is assumed to be at the outer fibres. This is reintroduced later in section 2.3.3, in modelling the theoretical response.

Both mechanisms are statically determinate which makes them easy to solve for and combine through simple hand calculations. The volume of reinforcement can be determined from the magnitude of the internal force flows. The ties were designed conservatively by assuming that the reinforcing steel carried the entire tensile force. The contribution of the concrete in the compressive force transfer in struts ab and ac, see Figure 2.22 (b), was conservatively ignored. It was assumed that the concrete would prevent bar buckling in compression given that cracking and spalling was not expected.

The only strut assumed to carry force through concrete action was the diagonal strut that runs between the location of the applied lateral force and the corner about which the wall panel rocks. The main concern through this region was not crushing of the strut but the possibly of tensile failure. Details of this strut are illustrated in Figure 2.23.

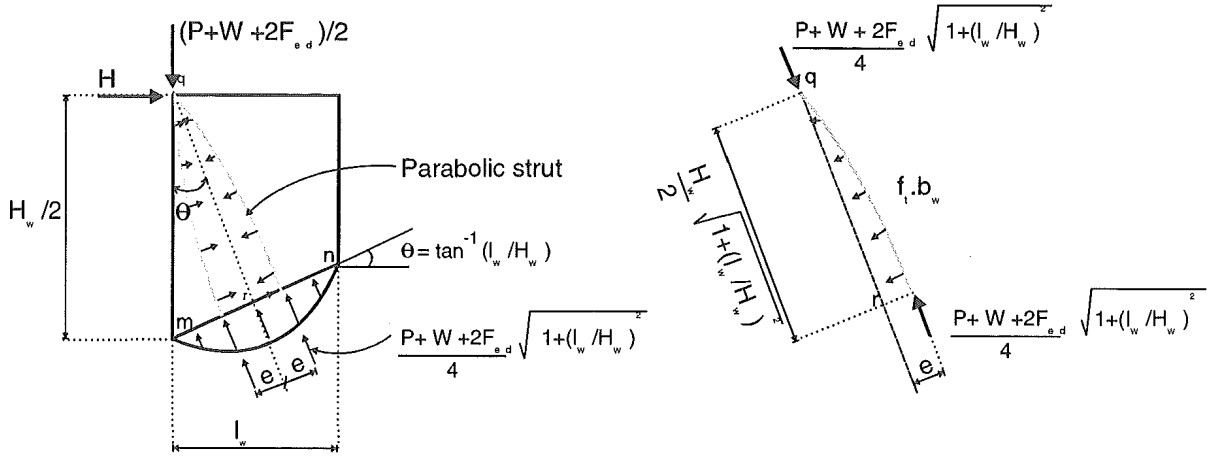

(a) Internal Force flow

(b) Free body diagram of parabolic strut

Figure 2.23 Model illustrating tensile forces along the main diagonal strut.

Figure 2.23 (a) assumes that the main strut spreads out towards the wall panel's mid-height and, as a result, tensile stresses develop in the panel.

Figure 2.23 (b) shows a free body of one of the curved struts forming the main diagonal strut. For simplicity this strut is assumed to have a parabolic shape and an eccentricity e with respect to the diagonal at the wall panel's mid-height. A uniformly distributed tensile force of magnitude $f_t.b_w$, where f_t is the tensile stress in the concrete and b_w is the wall panel width, is needed to equilibrate the parabolic struts.

The tensile stress f_t is found by taking moments about node q in Figure 2.23 (b).

$$\frac{f_t b_w}{2}\left\{\frac{H_w}{2}\sqrt{1+\left(\frac{l_w}{H_w}\right)^2}\right\}^2 = \frac{P+W+2F_{ed}}{4}\sqrt{1+\left(\frac{l_w}{H_w}\right)^2}\quad e \qquad (2.4)$$

Rearranging Equation 2.4 for f_t gives,

$$f_t = \frac{2(P+W+2F_{ed})e}{b_w H_w \sqrt{1+\left(\frac{l_w}{H_w}\right)^2}} \qquad (2.5)$$

Equation 2.5 requires e to be estimated. It is likely that the compressive stress distribution through section m-n be non-linear, with compressive stresses approaching zero at the wall panel edges. This implies that e is bounded and cannot exceed the value found if the stress distribution were rectangular. Hence,

$$e \le \frac{l_w}{4\cos(\theta)} = \frac{H_w}{4}\sqrt{1+\left(\frac{l_w}{H_w}\right)^2} \qquad (2.6)$$

Now substituting Equation 2.6 into Equation 2.5, results in,

$$f_t \le \frac{P+W+2F_{ed}}{2b_w H_w} \qquad (2.7)$$

The theoretical tensile stress in the concrete obtained from Equation 2.7 can now be compared with the direct tensile strength of concrete, f_t, in order to establish a demand/ capacity ratio. The direct tensile strength of concrete is usually taken as (Collins and Mitchell, 1991),

$$f'_t = 0.33\sqrt{f'_c} \qquad (2.8)$$

For which the demand/capacity ratio is,

$$\frac{f_t}{f'_t} \le \frac{P+W+2F_{ed}}{0.66 b_w H_w \sqrt{f'_c}} \qquad (2.9)$$

Equation 2.9 yielded a demand/capacity ratio of less than 0.25 for Unit 2.

In spite that the demand/capacity ratio in the main diagonal strut was low, an alternative internal force flow was enabled to provide an extra level of safety for the unit. Figure 2.24 below shows how the addition of an extra tie provides an alternative load path. The reinforcement comprising this tie was sized to carry the entire shear force if required. A number of stirrups were incorporated in the design, appropriately spaced in order to help funnel a portion of the applied load though this path.

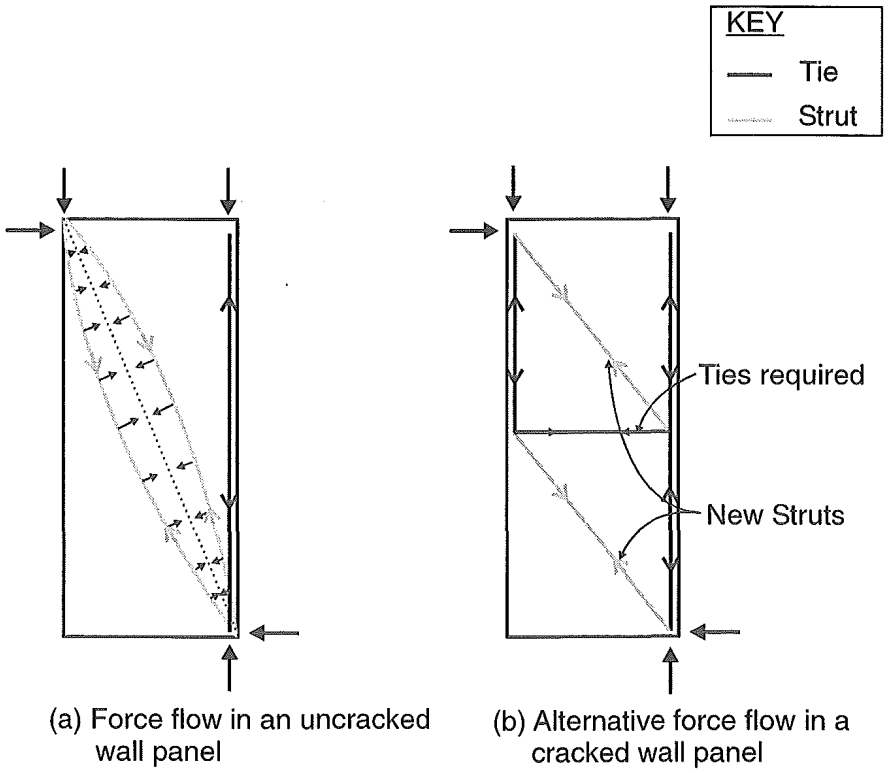

Figure 2.24 Alternative internal force flow in the wall panel under lateral loading.

2.3.2.2 Design of Energy Dissipators

The design of the tapered energy dissipators for Units 1 and 2 of Rahman and Restrepo (2000) mainly involved sizing the tapered diameter and length in order to withstand 2.5% drift while providing an adequate level of hysteretic damping. The design also required for the prestressing tendons to yield these bars back in compression once the lateral load was removed. This closes the gap at bottom of the wall essentially self-centring the unit.

It was found in Unit 2 of Rahman and Restrepo (2000) that one of the dissipators fractured under cyclic loading of less than 2% drift. This failure was unexpected and highlighted the need for further development in the design of these devices. Part of this research project was to take a closer look at the design of these tapered dampers in order to obtain a clearer idea on their behaviour and suggest guidelines in their design. The geometry of a typical tapered dissipator bar is shown in Figure 2.25.

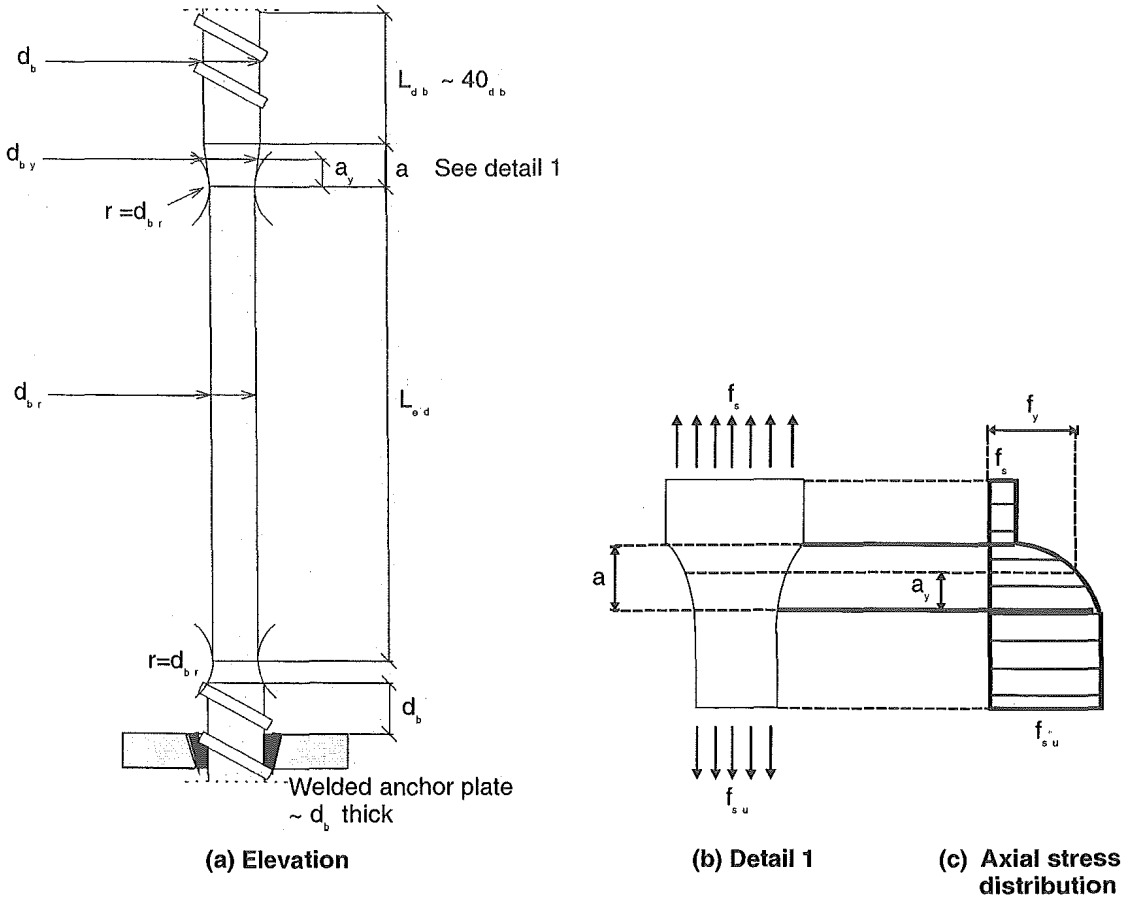

Figure 2.25 Geometry of a typical tapered dissipator bar.

A section of the bar is milled down to a diameter, d_{br}, over a length, L_{ed}. The reduced diameter is such that the milled portion can attain its ultimate tensile strength while the virgin portion of nominal diameter d_b, remains elastic. The milled portion of the bar is cast or grouted into the foundation beam. Since the foundation beam is designed to remain elastic, the milled portion of the bar can extensively yield in tension and compression within the tensile strain domain. Buckling of the bar is precluded by the cementitious matrix surrounding the milled portion of the bar. This requires the bar to be adequately anchored at both ends. The upper portion of the bar is grouted into a duct or tube in the wall panel. The length is usually equal to the basic development length, l_{db}. Anchorage to the lower portion of the dissipator is provided with the aid of a welded steel plate, given that the foundation beam is relatively shallow. The critical aspects in the design of these energy dissipators are the tolerances of the milled portion and the tapering radii at the ends of the milled portion. As far as the first aspect is concerned it is noteworthy to mention that lathes work under different tolerances and can be human dependent. The ratio between the maximum and minimum diameter in the section should not be greater than 2%, and the maximum diameter should never occur at the lower end of the milled section. This is because bond may develop in this region and as a result the strain distribution could be far from uniform as assumed in design. The second critical aspect is discussed, using mathematical expressions in the following pages.

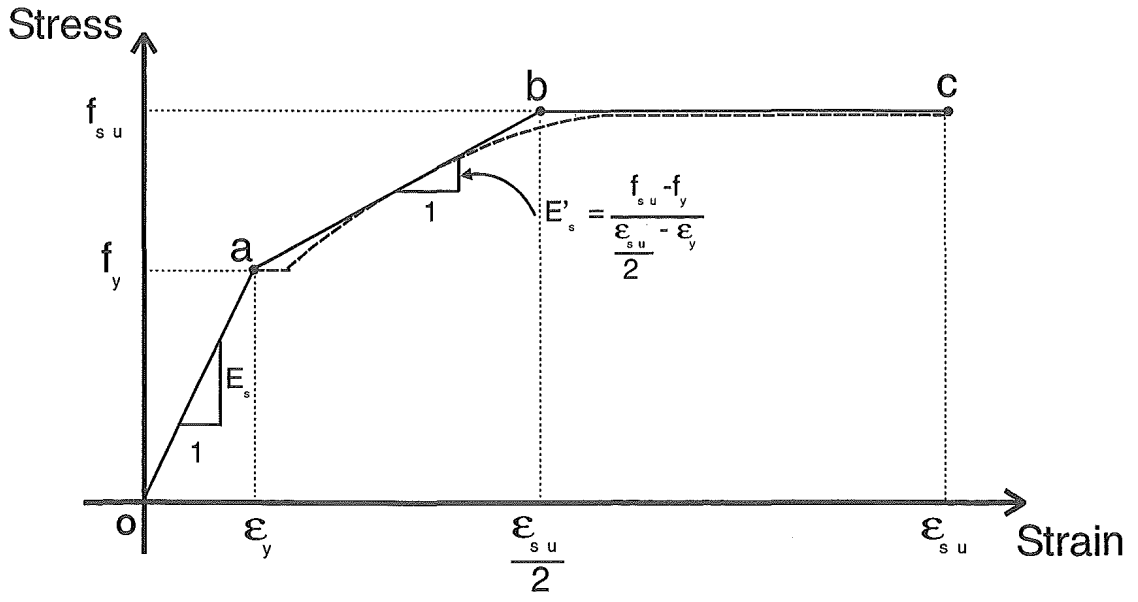

Figure 2.26 Idealised stress-strain behaviour of steel.

The main principles behind the design of the energy dissipators are:

- To ensure the original section of the bar used for manufacturing the energy dissipation remains elastic.

- To ensure that the milled portion of the bar can extensively yield in tension and compression. This requires the dissipators to be adequately anchored.

Figure 2.26 shows the monotonic stress-strain relationship for mild steel used in manufacturing of an energy dissipator. The relationship can be idealised with a tri-linear response. The first part of the response, see line oa in Figure 2.26, represents the response within the elastic range. Line ab in Figure 2.33 represents the strain hardening behaviour, while line bc represents the behaviour up to the onset of necking at point c.

The aim of the design of the energy dissipator is to ensure the milled portion of the bar be subjected to an average longitudinal strain of no more than $0.5\varepsilon_{su}$ at the design drift θ_u, and that the longitudinal strain at the surface of the dissipator be less than $0.75\varepsilon_{su}$. Note that the second requirement results from the fact that the dissipator will be subjected to bending when the wall rocks over the foundation. This is clearly shown in Figure 2.27. Caution must be taken to minimise or suppress any sliding shear across the wall panel foundation beam joint as sliding imposes kinking in the energy dissipators. In the analytical work that follows it is assumed that sliding does not occur.

Following the rational discussed in the previous paragraphs, the diameter of the milled section of the bars should be such that,

$$d_{br} \leq \frac{d_b}{\sqrt{\lambda_u}} \qquad \textbf{(2.10)}$$

Where λ_u is the ratio between the ultimate tensile and the yield strengths. For dissipators in which $d_{br} < d_b/\lambda_u$ yield will penetrate into the tapered end regions over a distance given by,

$$a_y = \frac{\sqrt{\lambda_u} - 1}{\frac{d_b}{d_{br}} - 1} a \qquad (2.11)$$

Note Equation 2.11 assumes that the tapered ends are conical.

The extension of the dissipators, Δ_e, can be approximated by the following expression if elastic deformations are ignored,

$$\Delta_e = \int_0^{ay} \varepsilon_{s(y)} dy + 0.5\varepsilon_{su} b = \Delta_{ea} + \Delta_{eLed} \qquad (2.12)$$

Equation 2.12 also assumes that inelastic deformations are negligible in the lower taper of this region. Bond between the dissipator and the concrete is expected to occur as a result of direct bearing.

The evaluation of the integral in Equation 2.12 requires a relationship that accounts for the variation of the longitudinal strain along the taper.

Let, the diameter at the distance y from the end of the milled portion of the bar be, $d_b(y)$.

$$d_b(y) = d_{br} + \frac{d_b - d_{br}}{a} y \qquad (2.13)$$

The cross-sectional area, $A_{sd}(y)$, associated with this diameter is,

$$A_{sd}(y) = \frac{\pi}{4}(d_b(y))^2 = \frac{\pi}{4}\left(d_{br} + \frac{d_b - d_{br}}{a} y\right)^2 \qquad (2.14)$$

The axial stress, $f_{s(y)}$, can be determined by dividing the maximum force expected to develop in the dissipator by $A_{sd}(y)$,

$$f_s(y) = \frac{{d_{br}}^2 \lambda_u f_y}{\left(d_{br} + \frac{d_b - d_{br}}{a} y\right)^2} \qquad (2.15)$$

Where: $\lambda_u f_y \geq f_s(y) \leq f_y$

The axial strain $\varepsilon_s(y)$ can be obtained from the strain-hardening stress-strain relationship shown in Figure 2.26 as,

$$\varepsilon_s(y) = \left(\frac{{d_{br}}^2 \lambda_u}{\left(d_{br} + \frac{d_b - d_{br}}{a} y\right)^2} - 1 \right) \frac{0.5\varepsilon_{su} - \varepsilon_y}{(\lambda_u - 1)} + \varepsilon_y \qquad (2.16)$$

Now,

$$\int_0^{a_y} \varepsilon_s(y)dy = \frac{-{d_{br}}^2 \lambda_u \left(\frac{0.5\varepsilon_{su} - \varepsilon_y}{\lambda_u - 1} \right)}{\left(d_{br} + \frac{d_b - d_{br}}{a} y\right)} \frac{a}{d_b - d_{br}} \Bigg|_0^{a_y} - \frac{\left(0.5\varepsilon_{su} - \varepsilon_y\right)}{\lambda_u - 1} y \Big|_0^{a_y} + \varepsilon_y y \Big|_0^{a_y} \qquad (2.17)$$

Given that the dissipators' rotate as well as elongate when a lateral displacement is applied, surface strains also have to be considered. Figure 2.27 shows the idealised behaviour of a dissipator at the design drift angle, θ_u. Figure 2.28 illustrates the undesirable event of bar bearing, this potential problem arises when the tapered length of the dissipator is relatively long.

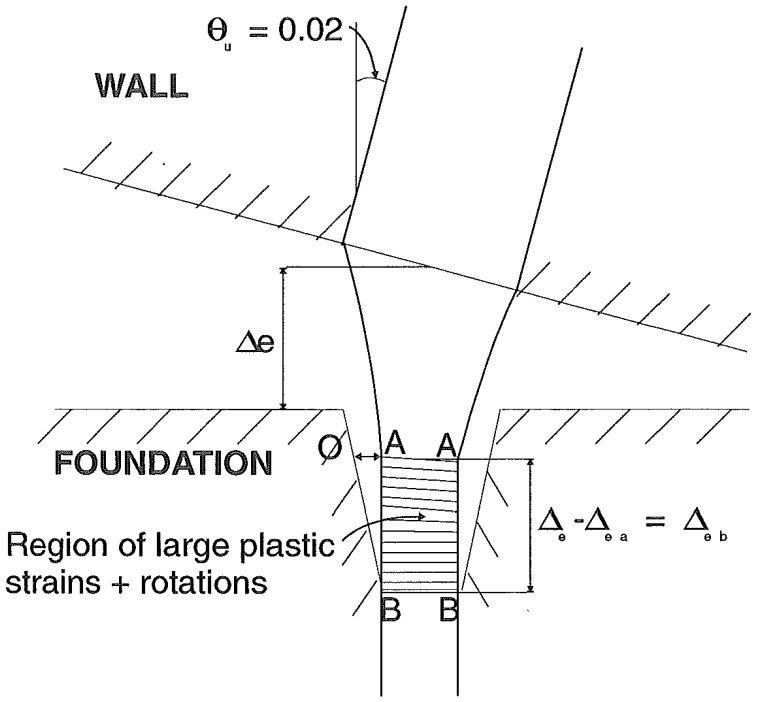

Figure 2.27 Bending of energy dissipator due to rocking action.

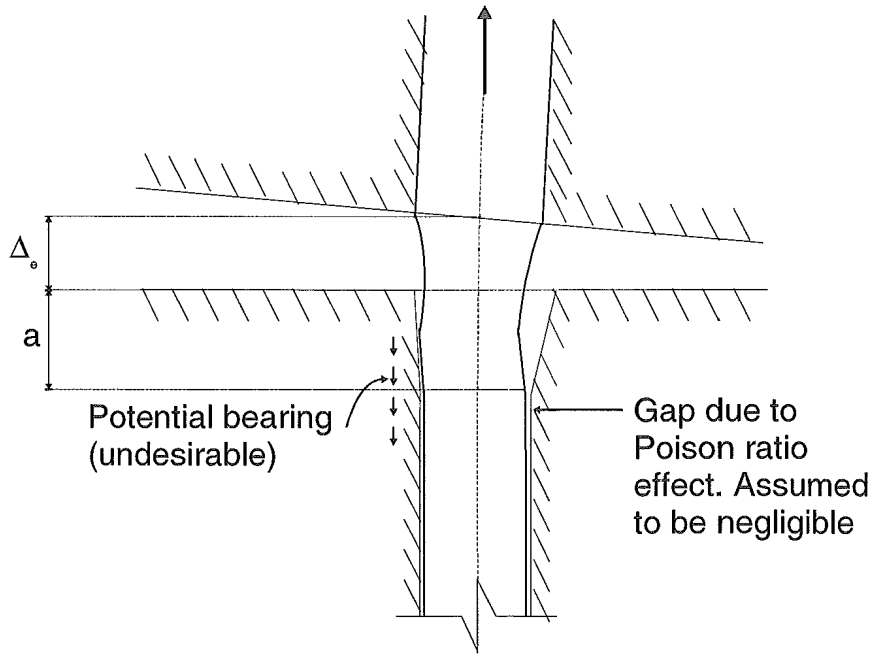

Figure 2.28 Bearing of energy dissipator due to rocking action.

Figure 2.29 is a simple model that describes the expected displacement and curvature distribution that the energy dissipator would expect to experience for a given level of drift. The model conservatively assumes that the entire rotation takes place within the milled portion of the energy dissipator. This is flexural deformations in the tapered end are ignored. This results in a conservative estimation of the surface strain at the end of the milled section. It is also assumed that at the lower end of the taper the rotation in the milled portion of the dissipator is zero.

Let Δ_e the axial deformation occurring within the milled portion of the dissipator and Δ_{ea} be the axial deformation in the taper. ϕ_t and ϕ_b are the curvatures at the milled portion of the dissipator at sections AA and BB shown in Figure 2.27.

The deflected shape shown in Figure 2.29 can only occur if the dissipator does not bear against the concrete . That is valid only if the distance OA in Figure 2.27 is greater than zero,

$$OA > (\Delta_{ea} + a)\theta_u \qquad (2.18)$$

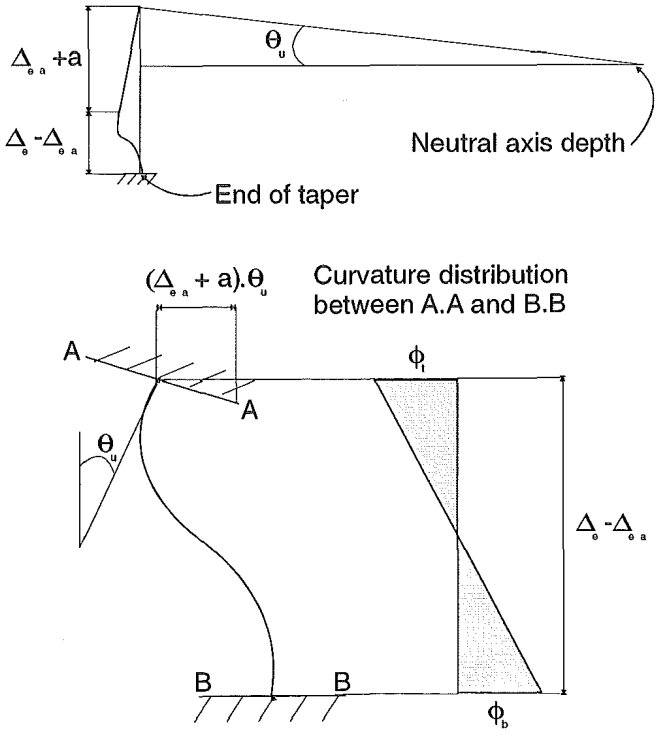

Figure 2.29 Model expressing expected displacement and curvature of dissipator.

The rotation θ_u can be obtained by integrating the curvature diagram. Uncoupling the tensile and compressive components, respectively, results in,

$$\theta_u = \phi_t(\Delta_e - \Delta_{ea}) - (\phi_t + \phi_b)\frac{(\Delta_e - \Delta_{ea})}{2} \quad (2.19)$$

and

$$(\Delta_{ea} + a)\theta_u = \frac{\phi_t}{2}(\Delta_e - \Delta_{ea})^2 - (\phi_t + \phi_b)\frac{(\Delta_e - \Delta_{ea})^2}{3} \quad (2.20)$$

Both ϕ_t and ϕ_b are unknowns for a given drift. Given Equations 2.19 and 2.20 these variables can be solved for simultaneously. Equation 2.21 was obtained through substituting ϕ_b as the subject.

$$\phi_b = \frac{2\theta_u}{(\Delta_e - \Delta_{ea})} - 6\frac{(\Delta_{ea} + a)}{(\Delta_e - \Delta_{ea})^2}\theta_u \quad (2.21)$$

ϕt can subsequently be solved for given that it is the last unknown.

Figure 2.30 shows the strain profile components at the cross-section AA. The maximum surface strain, ε_{ss}, can be defined as,

$$\varepsilon_{ss} = 0.5\varepsilon_{su} + \phi_t d_{br}/2 \quad (2.22)$$

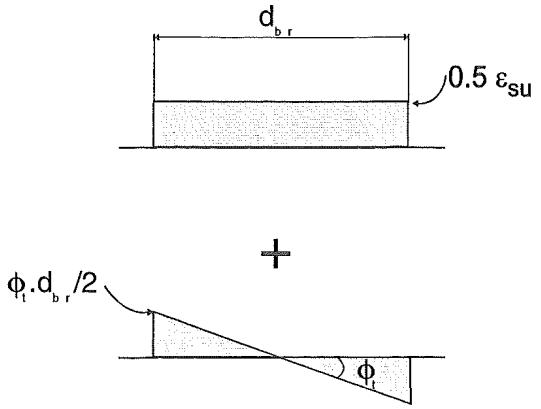

Figure 2.30 Strain profile through cross-section A-A.

With the equations of strain and geometric limitations due to bearing established various dimensions and aspect ratios were tested in order to find an efficient design. The following criteria were assumed:

At $\theta_u = 0.02$

$d_{br}/d_b = 16/20$

$0.5\varepsilon_{su} = 0.08$

$\varepsilon_y = 465/200{,}000 = 0.00233$

$\lambda_u = 1.4$

and

$\varepsilon_{ss} \leq 0.75\ \varepsilon_{su}$

The length of the taper was varied between 0.2b and 1.2b. The final design is shown in Figures 2.31 and 2.32.

Appendix C shows an example of the Microsoft Excel spreadsheet used in the design the energy dissipation bars. Comparison with the energy dissipator used in Unit 3 of Rahman and Restrepo (2000) is made.

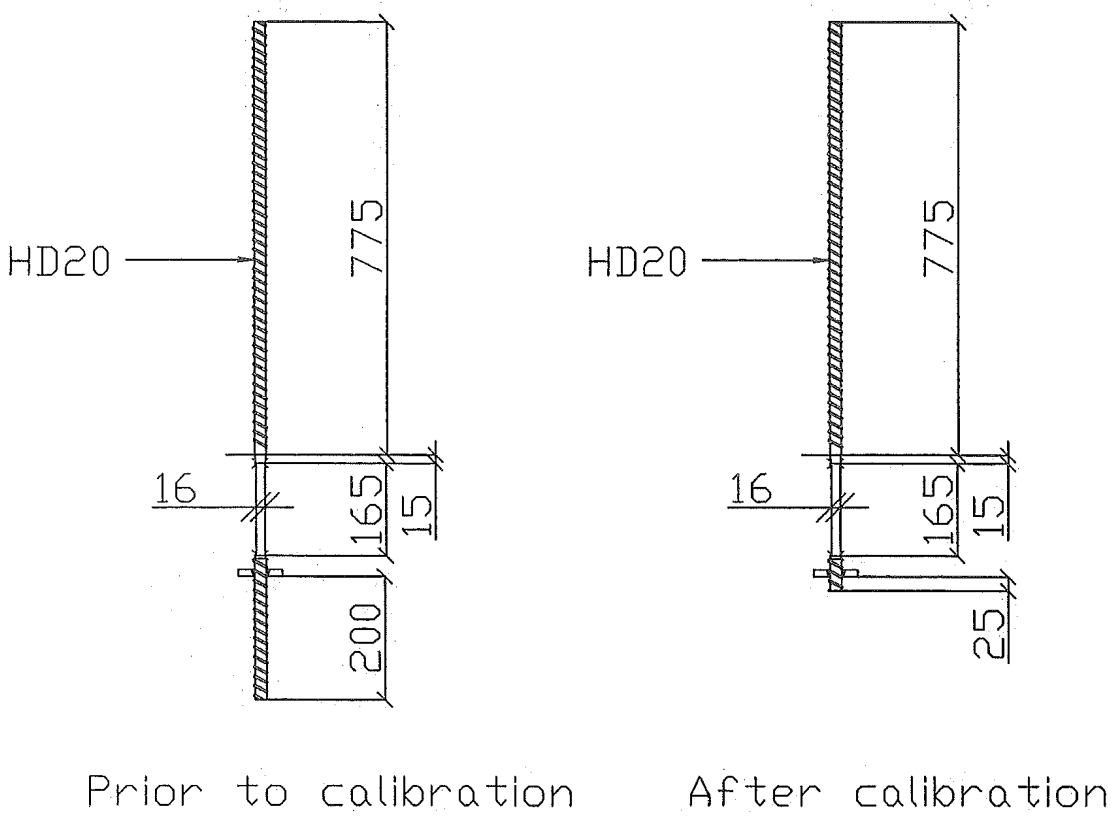

Figure 2.31 Geometry of energy dissipator.

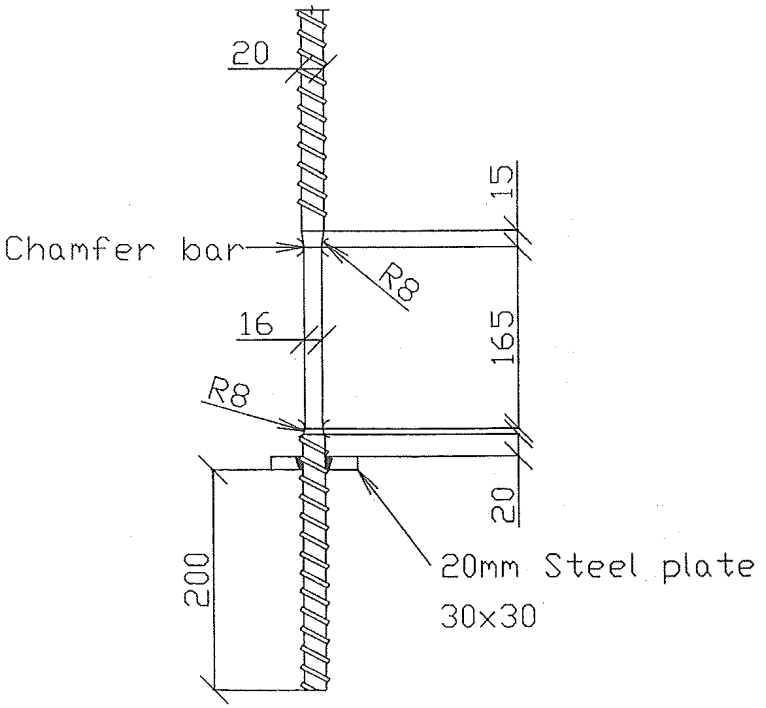

Figure 2.32 Detail of the tapered section.

2.3.3 Theoretical analysis of the response of Unit 2

Figure 2.33 plots the idealised lateral force versus lateral displacement response of a hybrid wall such as Unit 2. This figure also shows the responses of a rocking system and of a system prestressed with unbonded tendons that does not incorporate energy dissipators. The response of all these systems are somehow related and can be established with a single mathematical formulation, as shown later. In the initial stages of loading, the wall panel deforms primarily by flexure and shear. At this stage there is no contribution to the lateral displacement from deformations in the joint at the base of the wall. At point a, the extreme fibre of the joint located at the base of the wall is decompressed. Further loading results in a gradual opening of the joint, and as a result, in a gradual reduction in stiffness, see the dotted line ab in Figure 2.33. When the gap in the joint is sufficiently wide, the energy dissipators attain the elastic limit and yield, see point b in Figure 2.33. At this point, the stiffness of the wall is reduced further. If the stress-strain relationship of steel is idealised as shown in Figure 2.26, the stiffness of the system at loading beyond point b is related to the strain hardening stiffness in the energy dissipators plus the stiffness of the tendons. At point c, the energy dissipators reach the plateau associated with the ultimate tensile strength, see Figure 2.26. Hence, the remaining stiffness left in the system is solely due to the presence of the tendons that remain elastic. At point d the energy dissipators reach the limiting strain and are expected to fracture at any displacement beyond this point. The quadri-linear representation given by the lines oa, ab, bc, and cd is expected to provide a good representation of the backbone response of a hybrid system such as Unit 2.

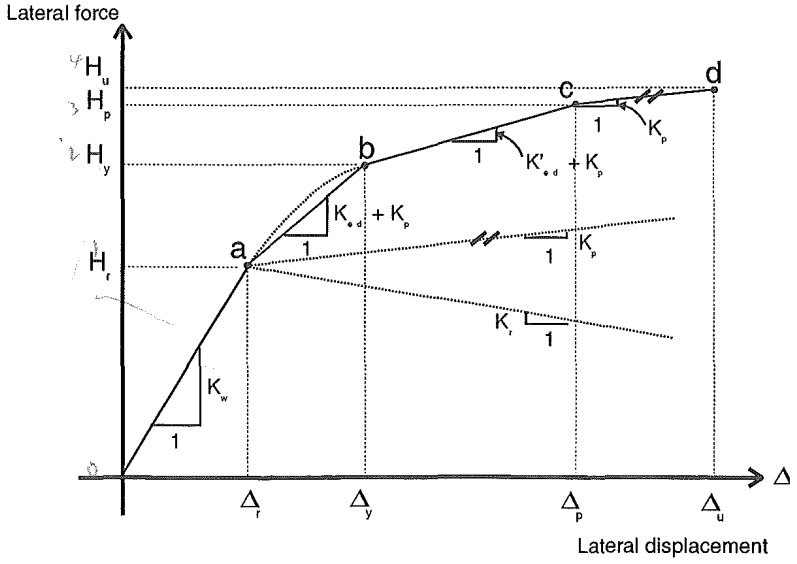

Figure 2.33 Load Displacement behaviour of Unit 2.

The lateral force, H_r, causing decompression at the extreme fibre at one of the lower corners of the wall can be determined from elastic theory. In this case the presence of reinforcing steel in the wall will be ignored for simplicity. Thus, from Figure 2.34,

$$H_r = (P+W)\frac{l_w}{6H_w} \qquad (2.23)$$

Where P and W are the prestressing force after losses and gravity load actions at the base of the wall panel, respectively.

The lateral displacement, Δ_r, at the top of the wall, where the force H_r acts, is obtained by combining the flexural and shear deformations occurring within the wall panel. Using elastic theory, assuming the wall panel is uncracked and that the shear modulus of concrete is $G_c = 0.4E_c$, the following expression is obtained for Δ_r,

$$\Delta_r = \left\{1+\frac{3}{4}\left(\frac{l_w}{H_w}\right)^2\right\}\frac{H_w^{\,3}}{3E_cI_g}H_r \qquad (2.24)$$

Where E_c is the concrete Young's modulus and I_g is the gross section second moment of area.

When the wall is loaded towards point b, see Figure 2.33, the neutral axis depth migrates towards the extreme fibre in compression. The resulting compressive force at the base of the wall approaches the extreme compressive fibre. At ultimate load, the resulting force will be very close to the centroid of the compression longitudinal reinforcement as assumed in design. If the position of the resulting force is assumed to remain constant when loading through points b to d, the analysis of the response of the wall can be represented as the superposition of a prestressed-only and a energy dissipation-only mechanisms, see Figure 2.35. Moreover, in the response of the hybrid wall tested the P-Δ effect caused by gravity load can be ignored. This results in $K_r = 0$ in Figure 2.33. The tangential stiffness K_{ed}, K'_{ed} and K_p depicted in Figure 2.33 can be determined using the mechanical model shown in Figure 2.35 as,

$$K_{ed} = k_{ed}\left(\frac{\frac{l_w - a}{2}}{H_w}\right)^2 = \frac{1}{4}\frac{E_s \sum A_{sd}}{L_{ed}}\left(\frac{l_w - a}{H_w}\right)^2 \quad (2.25)$$

$$\bar{K}'_{ed} = k'_{ed}\left(\frac{\frac{l_w - a}{2}}{H_w}\right)^2 = \frac{1}{4}\frac{E'_s \sum A_{sd}}{L_{ed}}\left(\frac{l_w - a}{H_w}\right)^2 \quad (2.26)$$

and

$$K_p = k_p\left(\frac{\frac{l_w - a}{2}}{H_w}\right)^2 = \frac{1}{4}\frac{E_{sp} \sum A_{sp}}{L_{sp}}\left(\frac{l_w - a}{H_w}\right)^2 \quad (2.27)$$

Where a/2 is the position of the resultant compressive force at the base of the wall, measured from the extreme fibre in compression; E_s is the elastic modulus of steel; E'_s is the strain hardening modulus of steel in the idealised stress-strain relationship shown in Figure 2.26; A_{sd} is the area of a single energy dissipator; E_{sp} is the elastic modulus of the carbon fibre tendons; A_{sp} is the total area of the tendons and L_{sd} is the tendon's unbonded length.

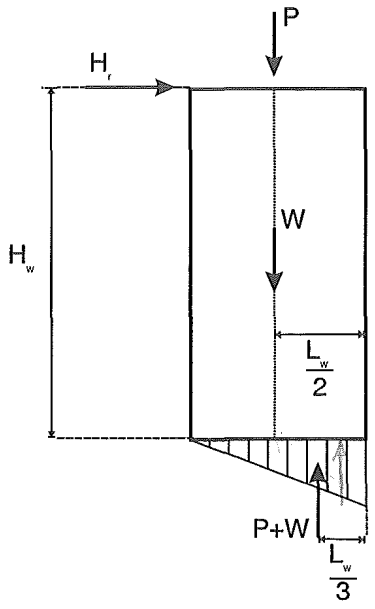

Figure 2.34 Free body diagram of a hybrid wall under a single point lateral load at the onset of rocking.

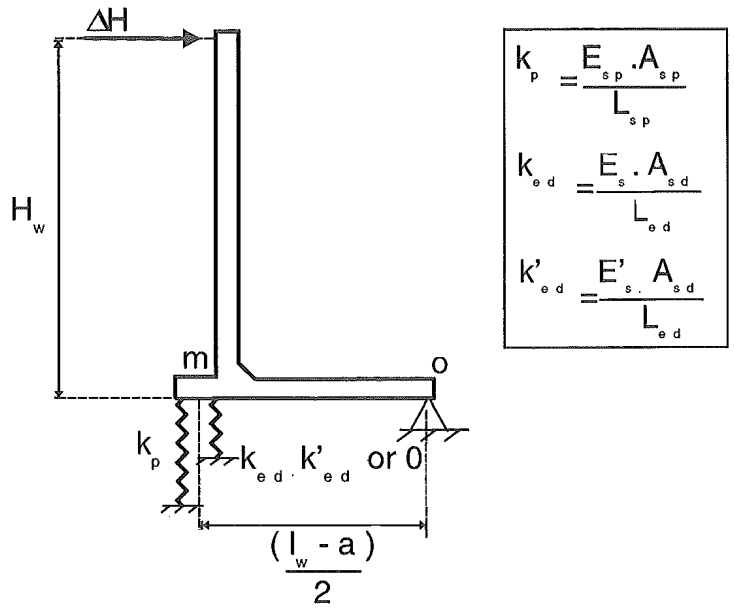

Figure 2.35 Lateral force resisting mechanisms in the hybrid wall after the commencement of rocking

Point b, associated with the development of yield in the energy dissipators, is described by the lateral force H_y and lateral displacement Δ_y given by,

$$H_y = (K_{ed} + K_p)(\Delta_y - \Delta_r) + 3H_r\left(1 - \frac{a}{l_w}\right) \qquad (2.28)$$

and

$$\Delta_y = 2\frac{f_y}{E_s} L_{ed} \frac{H_w}{(l_w - a)} + 3\Delta_r\left(1 - \frac{a}{l_w}\right) \qquad (2.29)$$

By substituting Equations 2.25, 2.27 and 2.29 and simplifying, Equation 2.30 is obtained.

$$H_y = \frac{1}{2}\frac{l_w - a}{H_w}\left(1 + \frac{E_{sp}}{E_s}\frac{L_{ed}}{L_{sp}}\frac{A_{sp}}{\sum A_{sd}}\right) f_y \sum A_{sd} + 3H_r\left(1 - \frac{a}{l_w}\right) \qquad (2.30)$$

Point c in Figure 2.33, at the development of the ultimate tensile strength in the energy dissipators in the idealised stress-strain relationship shown in Figure 2.26, can be determined similarly to point b. The force H_p and displacement Δ_u are given by the incremental equations,

$$H_p = (K'_{ed} + K_p)(\Delta_p - \Delta_y) + H_y \qquad (2.31)$$

and

$$\Delta_p = 2\frac{f_{su} - f_y}{E'_s} L_{ed} \frac{H_w}{(l_w - a)} + \Delta_y \qquad (2.32)$$

The tangential stiffness between points c and d in Figure 2.33 equal to K_p. This means that the lateral force in this region of the backbone curve is given by,

$$H = K_p(\Delta - \Delta_p) + H_p \qquad (2.33)$$

The quadri-linear representation detailed in this section was found to provide a very good representation of the backbone response of Unit 2. The theoretical response of Unit 2 is plotted in Figure 4.32 in section 4.3.2.

2.3.4 Foundation Beam Design

The foundation beam of Unit 2 followed similar design objectives as those expressed previously for Unit 1. The aim being to ensure that, apart from the energy dissipating bars, the foundation remained elastic.

Given that carbon fibre tendons have very seldom been used in seismic design in the world, it was thought prudent that they be recoverable and undamaged after testing was completed. Recesses were therefore cast into the foundation within which the prestressing anchors sat without the necessity of grouting them in place. Having the recesses open also helped in the placement the tendons given they were delivered with anchor sleeves epoxied at their ends. These recesses however caused an internal force flow discontinuity within the beam that required the development of a strut-and-tie model in order to establish a statically admissible force flow to which a reinforcement layout could be assigned. The strut-and-tie model developed is discussed later on in this section.

Flat plates were introduced into the design onto which the lower corners of Unit 2 would bear when rocking. These plates were placed at the top of the foundation beam and the bottom of the wall in order to help prevent crushing of the compressed corner concrete. By having a hard surface to bear upon it was hoped that stiffness degradation caused by residual strains developing in the compressed concrete could be avoided or minimised.

Slots were cut into the plates cast into the foundation beam to allow a gear shaped tooth welded to the base of Unit 2 to pivot in and out as the wall rocked, see Figure 2.19. The function of these teeth were to act as a guide and prevent the wall from becoming dislodged under repeated cyclic loading. Figures 2.36 to 2.38 show the final reinforcement design of the foundation beam. Note the inclusion of rectangular ducts for the prestressing tendons, the 50mm diameter circular ducts into which the tapered dissipator bars were grouted, the 100mmx465mm plates onto which Unit 2 beared, and the recesses within which the prestressing anchors were located.

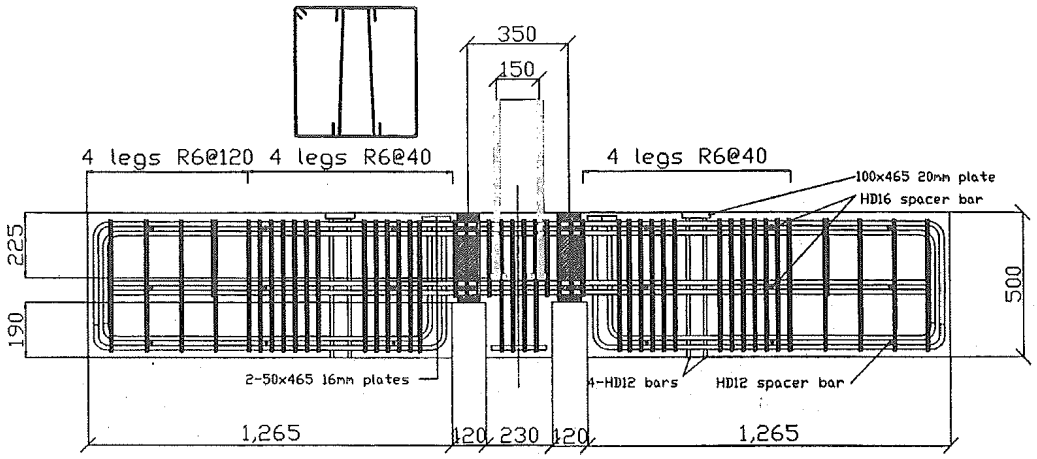

Figure 2.36 Reinforcement layout of Unit 2 foundation beam.

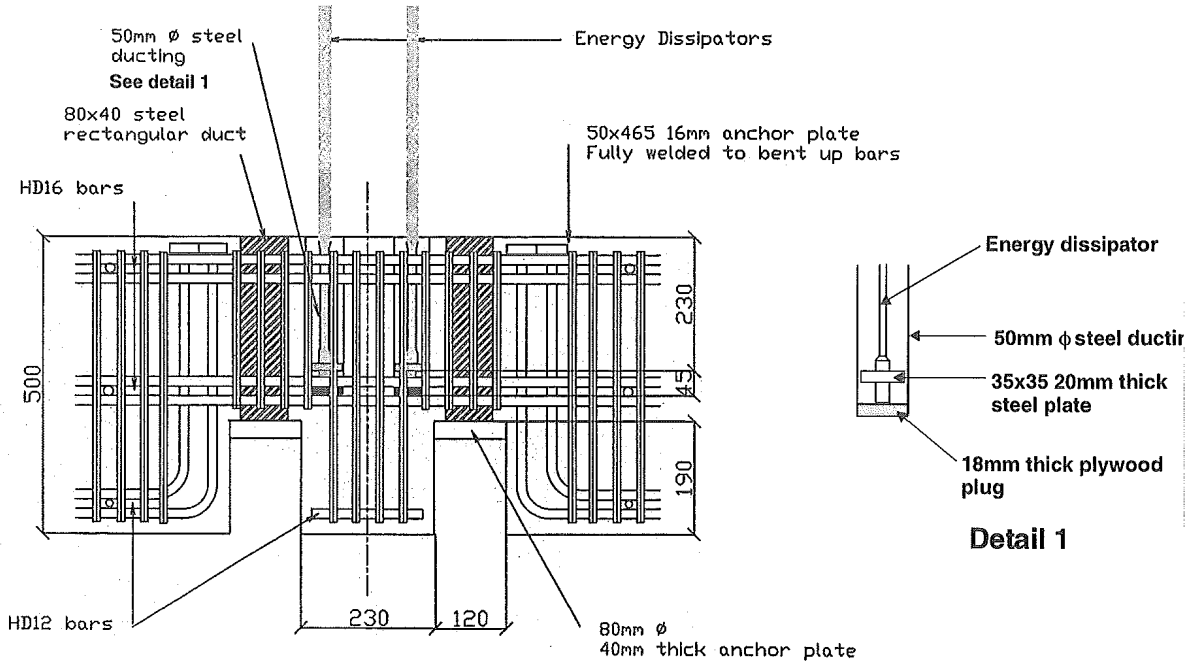

Figure 2.37 Detail showing prestressing and dissipator duct layout.

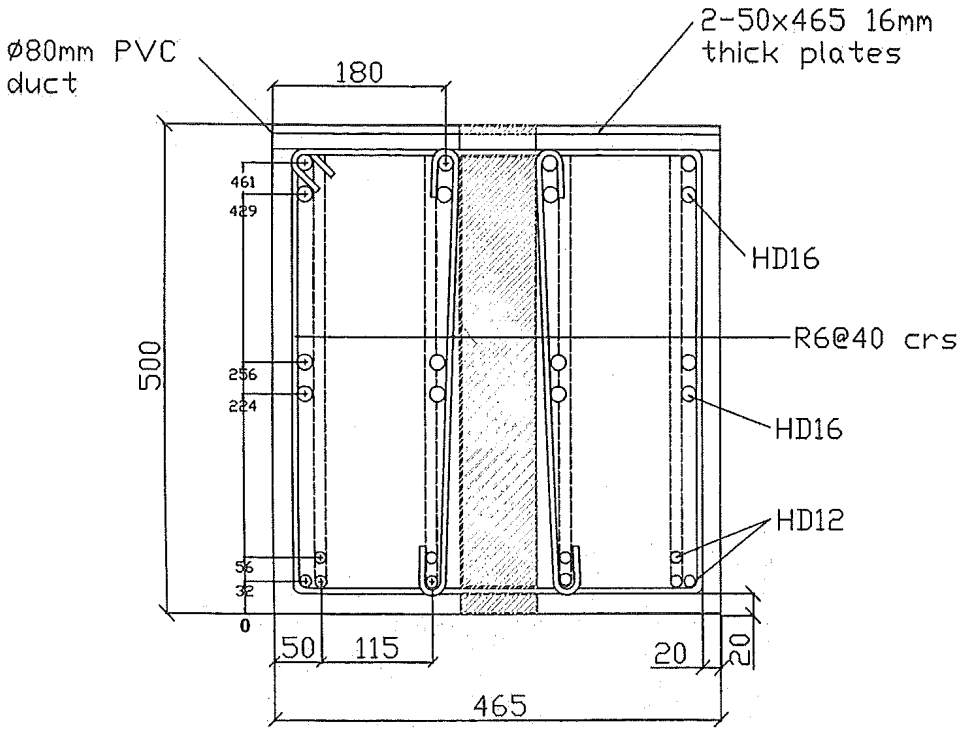

(a) Typical cross-section through beam

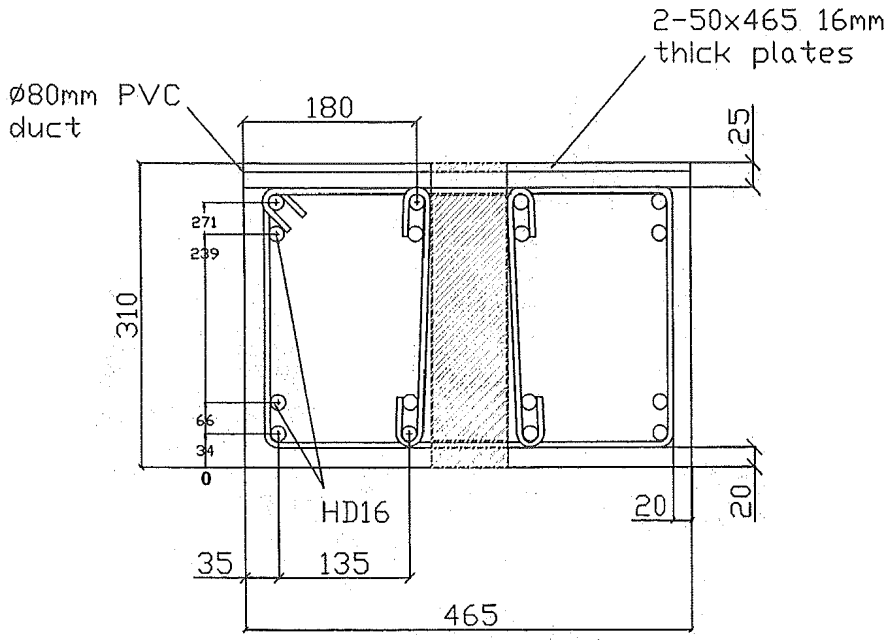

(b) Cross-section through recess

Figure 2.38 Cross-sectional details of the foundation beam for Unit 2.

The nature of strut-and-tie modelling reveals several possible statically admissible solutions. However, there are some solutions more efficient than others. The analysis of the strut-and-tie model, for the foundation beam, was rather complicated given the geometric irregularities of the beam. There were two load cases considered,

1. Theoretical lateral force estimated at 2% drift.

2. Internal forces developed in the unit as a result from zero lateral forces upon a large drift demand. This load case is referred to here as the static load case.

Figures 2.39 and 2.40 describe the strut-and-tie models developed.

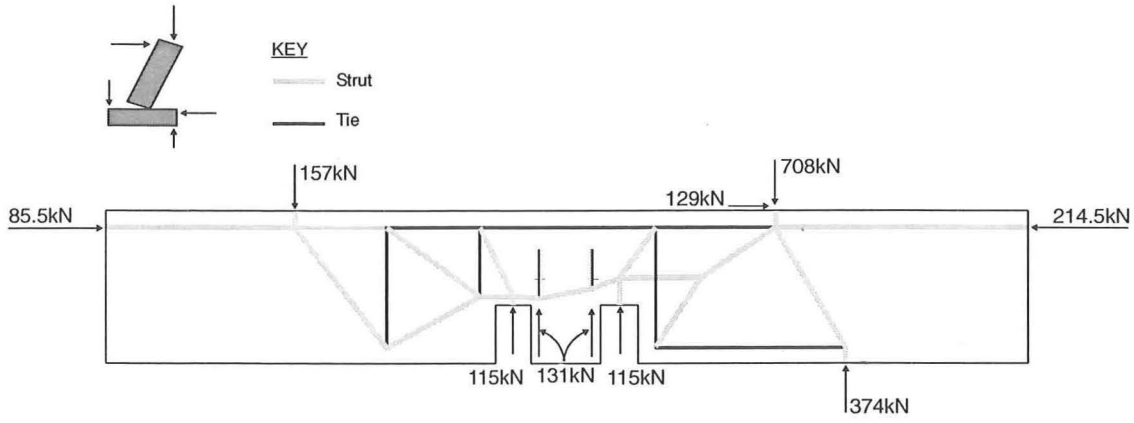

Figure 2.39 Strut-and-tie model for Unit 2 under left-to-right lateral loading.

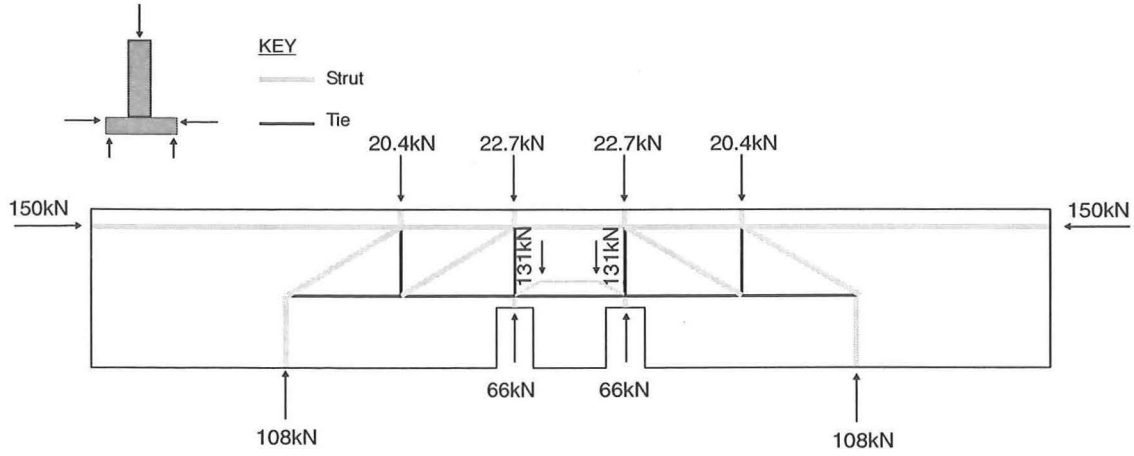

Figure 2.40 Strut-and-tie model for Unit 2 upon unloading from a large drift cycle.

Appendix A provides the design actions and resultant strut-and-tie forces, for both load cases analysed.

The static load case was analysed to establish the magnitude of the struts formed due to compression of the energy dissipators. Vertical running reinforcement was provided by bending the bottom longitudinal bars up 90°. These bars were anchored at the top of the foundation beam through welding to an anchor plate. These anchor plates are clearly shown in Figure 2.37. The horizontal forces at the foundation beam ends are equilibrated by hydraulic rams placed at these locations.

A review on the compressive strength of the struts was performed to ensure that concrete crushing would not occur. Appropriate ratios of longitudinal and transverse reinforcement were placed in the tie locations, with adequate development lengths and anchorage provided. As it will be discussed in section 4.3.2, failure to develop the 131kN energy dissipation compressive force in the static load case, had a significant effect in the energy dissipation capacity of this unit.

2.3.5 Construction

The construction of the foundation beam for Unit 2 was similar to that required for Unit 1. HD12 and HD16 bars were used as the longitudinal reinforcement while R6 hoops and stirrups were utilised as transverse reinforcement.

The recesses within which the prestressing anchors eventually sat were made through the construction of two collapsible boxes that were removed once the foundation had been cast. The finished reinforcement cage is shown in Figure 2.41. The plates upon which Unit 2 rocked, and the welded plates required for anchoring the bottom bent-up bars are clearly visible in this figure. The 50mm diameter ducts for grouting the energy dissipator bars are also visible.

Given the identical geometry for both Unit 1 and 2, the original formwork from the initial unit was reused. As end plates were not used in the construction of the second foundation beam, a small amount of extra formwork was required. As with Unit 1 both the casting of the beam and wall unit were completed in a single operation, using two different admixtures.

The construction of wall panel initially required that the top and bottom steel plates to be profile cut. This was done to incorporate the prestressing and energy dissipator ducts as well as to enable the longitudinal reinforcement to be anchored. This process was rather labour intensive given that the laboratory facilities were fairly limited in completing such a task. This was far and away the most expensive procedure in the construction of Unit 2. The efficiency and cost of this step could have been largely reduced if completed in a specialist facility with the appropriate equipment. Additional savings could be made if the operation was completed on a larger scale with a number of units involved.

As described in section 2.3.2 the wall panel was constructed in two separate portions. The lower portion included the baseplate, the corner reinforcement plates, the SHS's for grouting of the energy dissipators, the diagonal reinforcement and the lower portion of the longitudinal reinforcement. The upper portion contained the top plate, and remainder of the longitudinal and horizontal reinforcement.

Construction of the lower portion of the wall panel commenced with the welding of the diagonal and lower portions of the longitudinal reinforcement to the corner reinforcement plates. Figure 2.42 shows these bars being positioned prior to the welding operation. Once completed the corner reinforcement plates were fillet welded to the base plate.

The square hollow sections were then cut to size with two 10mm thick plates welded at the top, connecting them. These plates created the surface to which the diagonal reinforcement was welded establishing a load path for the transfer of force developed within the energy dissipators. The ducts were then welded to the base plate. Figure 2.43 shows the completed lower portion of the wall following the longitudinal bars being welded into position, and stirrups tied.

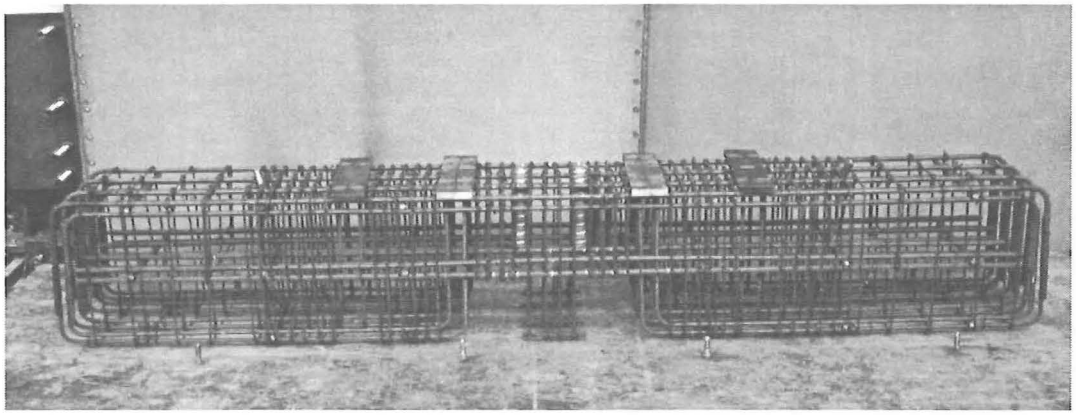

Figure 2.41 Reinforcing cage for the foundation beam of Unit 2.

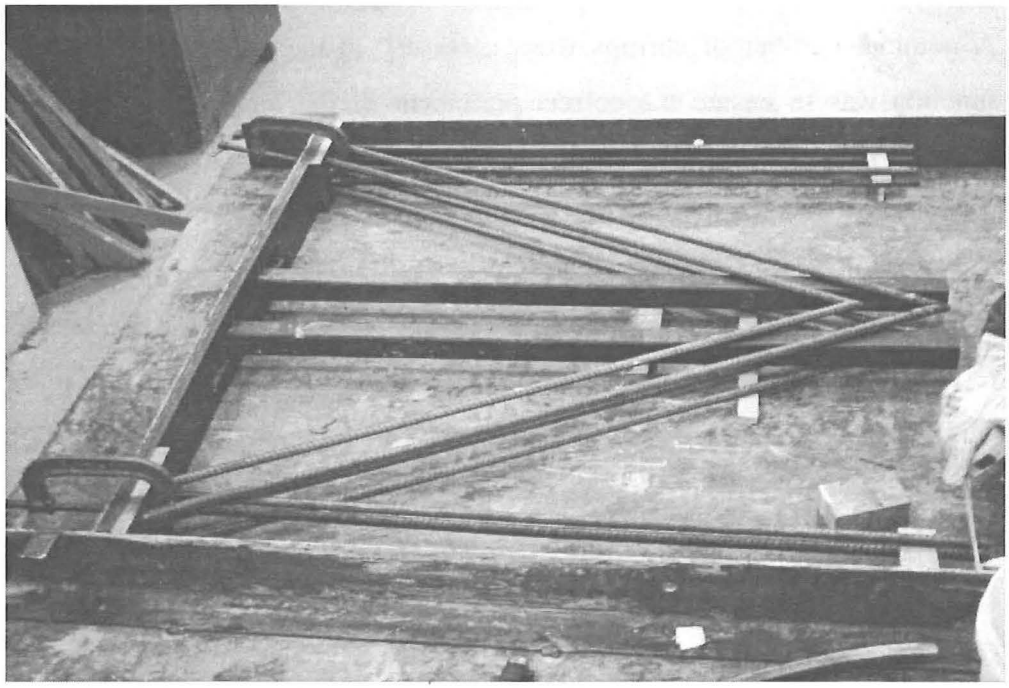

Figure 2.42 Diagonal and longitudinal bars prior to being fillet welded to the base plate.

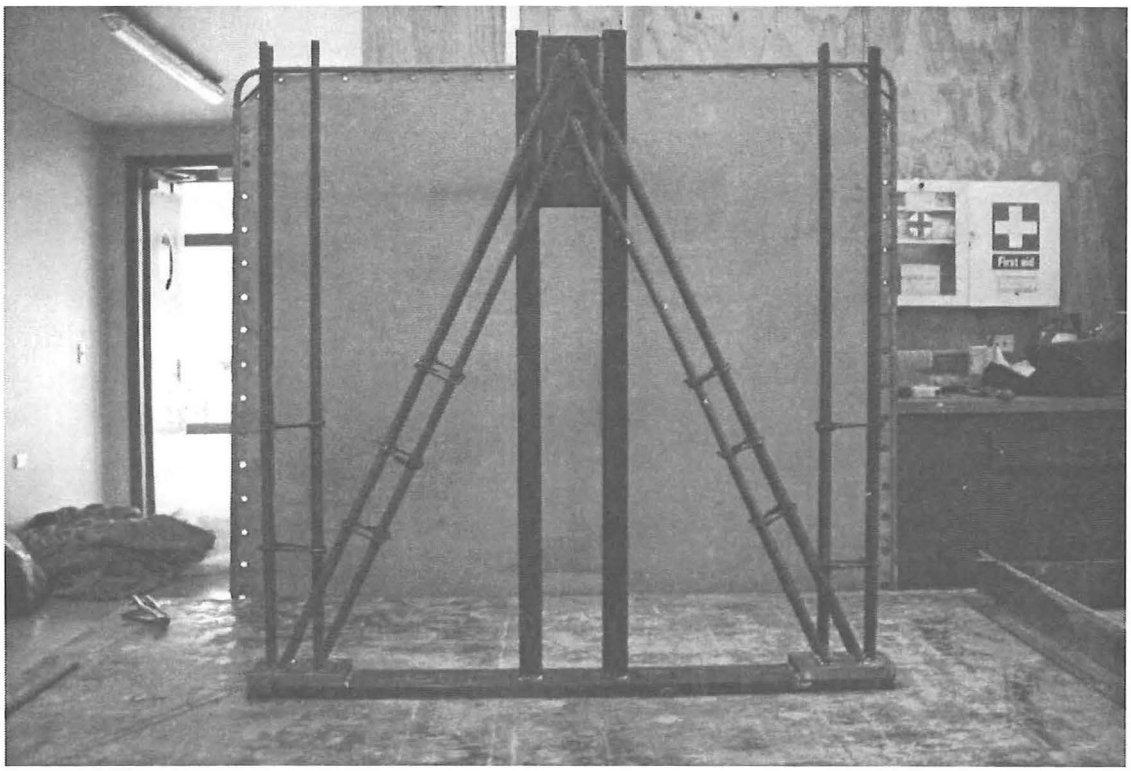

Figure 2.43 Completed lower portion of the wall panel cage for Unit 2.

A nominal number of stirrups were necessary in the construction of Unit 2. Their function was to ensure the correct placement of the longitudinal bars in addition to increasing the stability of the cage prior to casting. Strain gauges were then attached to the lower longitudinal and diagonal reinforcement, as outlined in section 3.3.4.

Construction of the upper section of the wall commenced with the main longitudinal reinforcement being welded to the top plate. Four HD10 stirrups were placed at 50mm centres positioned directly above the splicing development length.

The top half of the wall was placed within the steel angle formwork and subsequently spliced to the lower portion. The casting bed had been sprayed with a concrete retardant prior to this operation. The braces used previously during the construction of Unit 1 to position the lifting eyes and ducts for the external prestressing brackets were then attached. Figures 2.44 and 2.45 illustrate the final stages in the construction of the wall panel of Unit 2 prior to the casting operation.

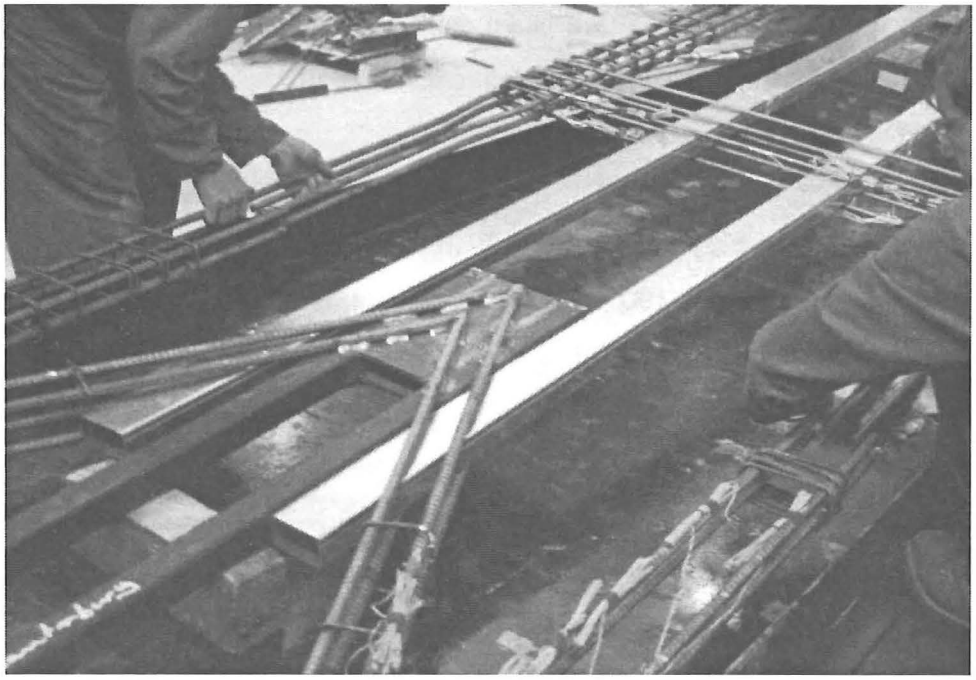

Figure 2.44 Splicing of top and bottom portions of the wall panel cage for Unit 2.

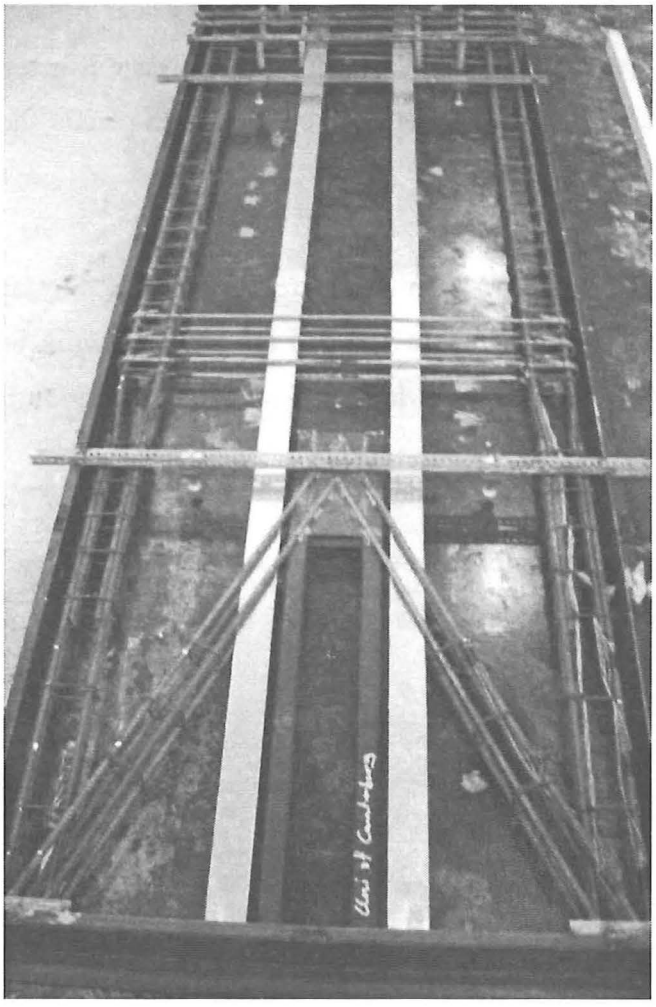

Figure 2.45 Completed wall panel cage for Unit 2.

Given that both the foundation beam and wall panel were designed according to two different admixtures two separate deliveries were made. These deliveries were spaced two hours apart with the wall panel cast first.

The mix design prescribed for the wall unit required a minimum concrete strength of f'_c = 40 MPa, a slump of 100 -120mm, maximum aggregate size of 13mm, and Dramix steel fibres (RC-65/35-BN) at a dosage of 40kg/m^3. On arrival slump tests were performed on the mix which revealed an 80mm slump. Workability was improved with the addition of superplasticiser.

The mix design prescribed for the foundation beam required a minimum concrete strength of f'_c = 40 MPa, a slump of 100 -120mm, and maximum aggregate size of 10mm. Slump tests revealed a 100mm slump, thus no superplasticiser's were required. The actual casting operation was very similar to that of Unit 1 described in section 2.2.3. The concrete was adequately vibrated and later finished with wooden and steel floats. Once the concrete had sufficiently hardened wet hessian sacks were placed on top of the specimens which were then covered with plastic sheeting to ensure adequate curing conditions.

Given that the casting operation was performed prior to the statutory holidays it was not until 16 days after the concrete was cast that the formwork was removed and cylinder tests performed. At this stage the wall panel and foundation beam were stripped of all formwork.

Once free of the formwork the two tooth-shaped plates were welded to corners of the wall baseplate. Figure 2.46 shows one of these teeth offset 50mm from the corner of the unit.

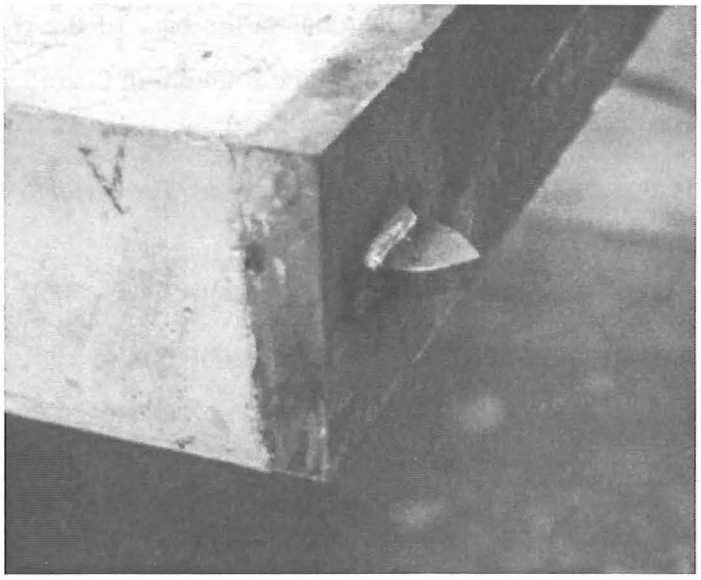

Figure 2.46 Western-corner guiding tooth.

The lifting and erection of Unit 2 was identical to those methods employed for Unit 1, outlined in section 2.2.3. Given height restriction of the crane Unit 2 was lifted with the carbon fibre tendons and tapered dissipator bars inside the wall panel. These were positioned into place prior to the unit being grouted to the foundation beam. Grouting of the tapered dissipator bars was undertaken using Conbextra GP. This was accomplished in two stages with the ducting within the foundation being cast prior to that within the wall.

Post-tensioning of the carbon fibre tendons required two 53mm diameter centre hole rams. This size centre-hole was necessary given the triangular tendon layout (refer Figure 2.47) required in order to avoid clashing of the epoxied steel anchors. Figure 3.10 shows one of these anchors in detail. Upon the rams, hollow tubes acting as spacers were placed with load cells positioned atop of these. Given that the carbon fibre tendons were delivered with anchors attached to both ends, 80mm diameter 40mm thick slotted plates were machined with which to anchor the post-tensioning force. A protective cage was constructed that topped the tendons in case of failure. Figure 2.48 shows the completed post-tensioning system positioned on top of the wall panel.

To prevent a sharp kinking of the tendons at the base of the wall panel, rubber inserts were machined to fit the ducting within the foundation beam. Figure 2.47 models this insert and illustrates the symmetric layout of the rods within the duct. Also shown in this figure is one of the slotted steel plates that were used to anchor the prestressing tendons.

Details concerning the prestressing and instrumentation of Unit 2 are outlined in section 3.3. Figure 2.48 shows Unit 2 prior to testing.

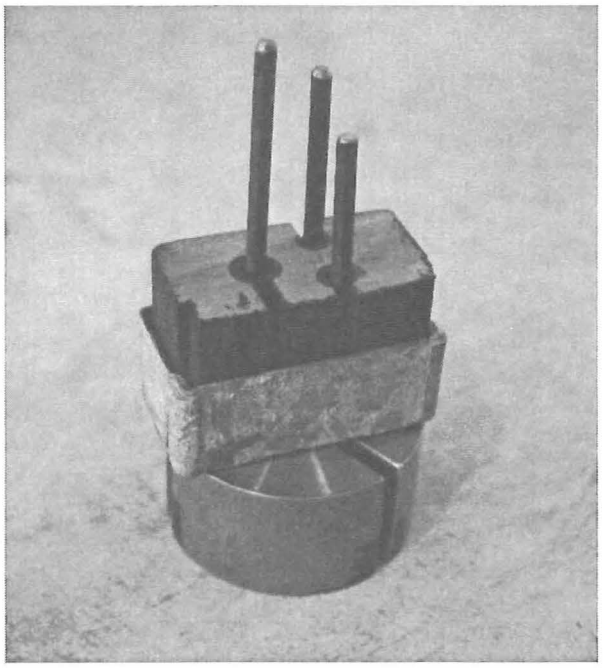

Figure 2.47 Basic foundation insert for post-tensioning rods.

Figure 2.48 Completed Unit 2 prior to testing.

3 EQUIPMENT AND INSTRUMENTATION

3.1 LOADING ARRANGEMENT

The restraint and loading frame used by Rahman and Restrepo (2000) was reused for the tests carried out in this programme. The main loading frame consisted of a steel column bolted to a CHS stay. These two elements were bolted down to a 750mm thick strong floor.

Two RHS were bolted either side of each unit spanning the loading and restraint columns of the test rig at two thirds the height of the wall. These provided resistance to both out-of-plane deformations and twist. These stabilising beams modelled the actions of the diaphragms, which prevent out-of-plane buckling. This was achieved through bolting two nylon pads (both north and south faces) to the restraint beam. A 1mm gap was initially set that separated these pads from corresponding steel sheets epoxied to the wall.

The foundation beams were secured to the laboratory strong floor through the use of two large double channel sections and 32mm high-strength hold down bolts, spaced 1800mm apart. These sections provided restraint against overturning of the foundation beam once lateral force was applied to the wall.

3.2 APPLICATION OF LOADS

Hydraulic rams and actuators were utilised for both the application and restraint of loads imposed upon each unit. These being in most cases identical or very similar to those used by Rahman and Restrepo (2000). The relative positions of which are shown schematically in Figure 3.2.

The lateral load applied to both Unit 1 and 2 was supplied thought the use of a ±450mm stroke double-acting hydraulic actuator, (330kN compression and 440kN tension) see actuator A1 in Figure 3.2. This actuator was bolted to the steel column of the main

loading frame at a height 4.25m from the strong floor (3.75m from the base of the wall). Connection to the wall was provided via the load cell through a pin connection. This consisted of a 20mm thick plate cast into the each unit to which 10mm deformed bars extending the width of the wall were welded.

Equivalent gravity load was simulated via externally post-tensioning two 23mm diameter threaded high-strength bars situated both sides of each unit. A constant axial load of 100kN per bar was provided by two centre-hole rams, see rams R2 and R3 in Figure 3.2. A pin connection attaching the post-tensioned bars to the strong floor allowed the external bars to rotate with the units as they were subjected to lateral displacements. Details of this connection as well as that of the frame-wall connection are given in Figures 3.3 to 3.5. A constant axial load was achieved through the use of computer controlled hydraulic valves which kept the axial load constant despite the elongation and shortening of the threaded bars under cyclic loading.

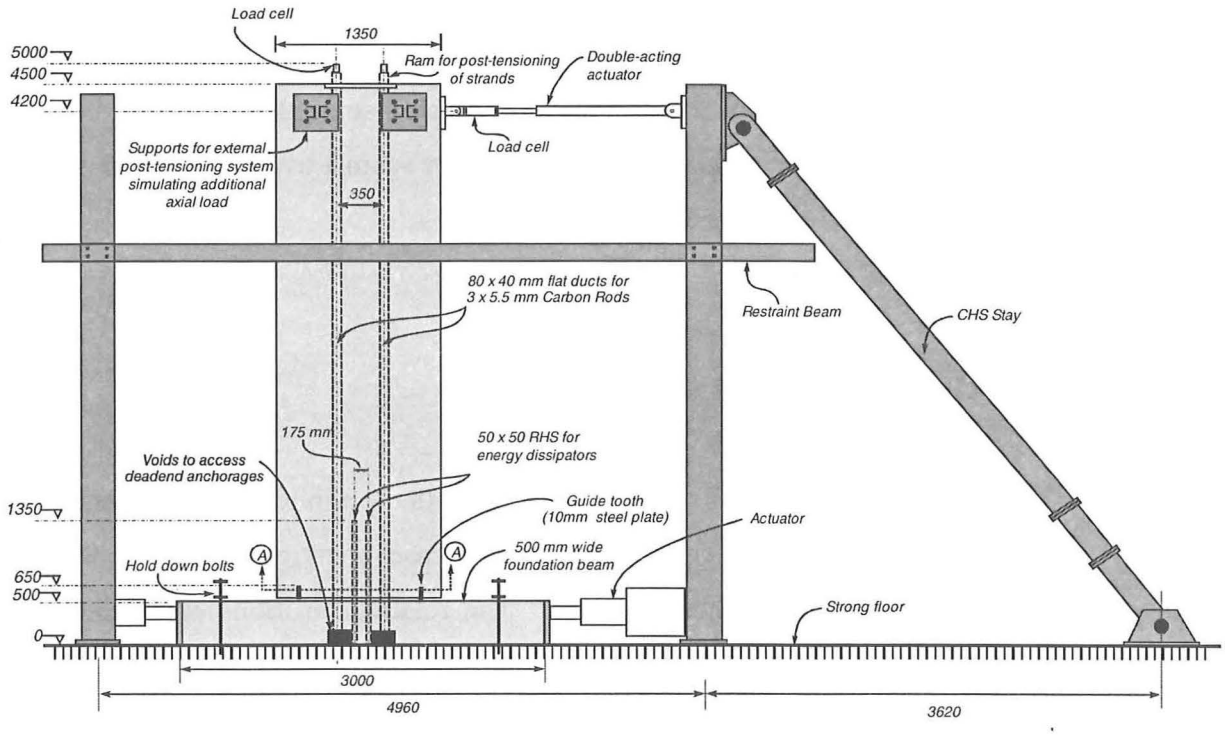

Figure 3.1 Schematic representation of test rig (Rahman and Restrepo, 2000).

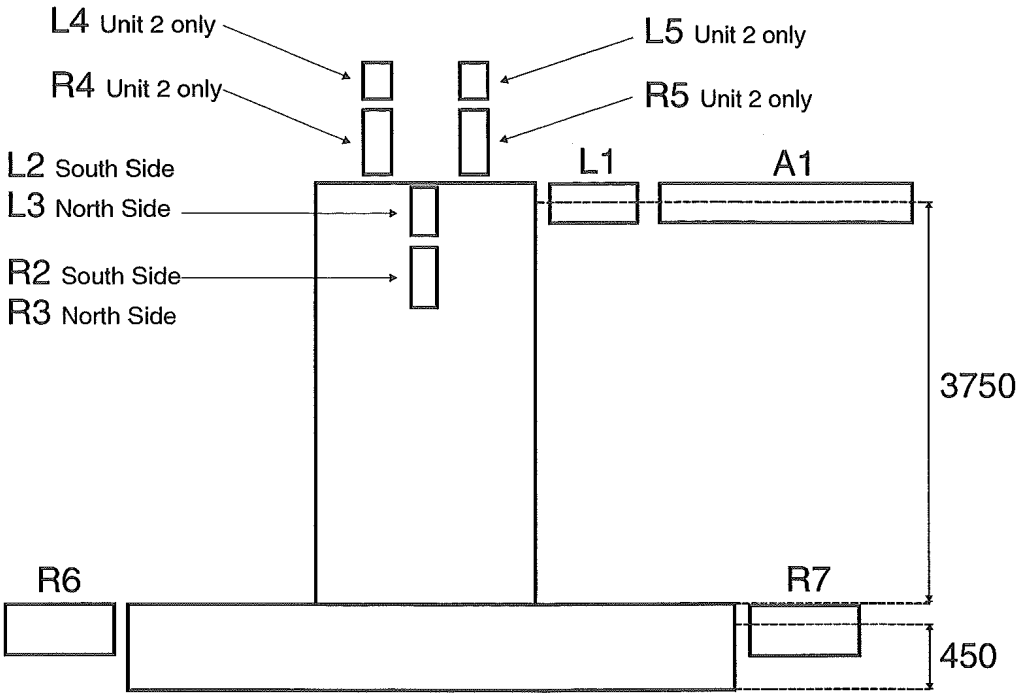

Figure 3.2 Schematic representation of the loading arrangement.

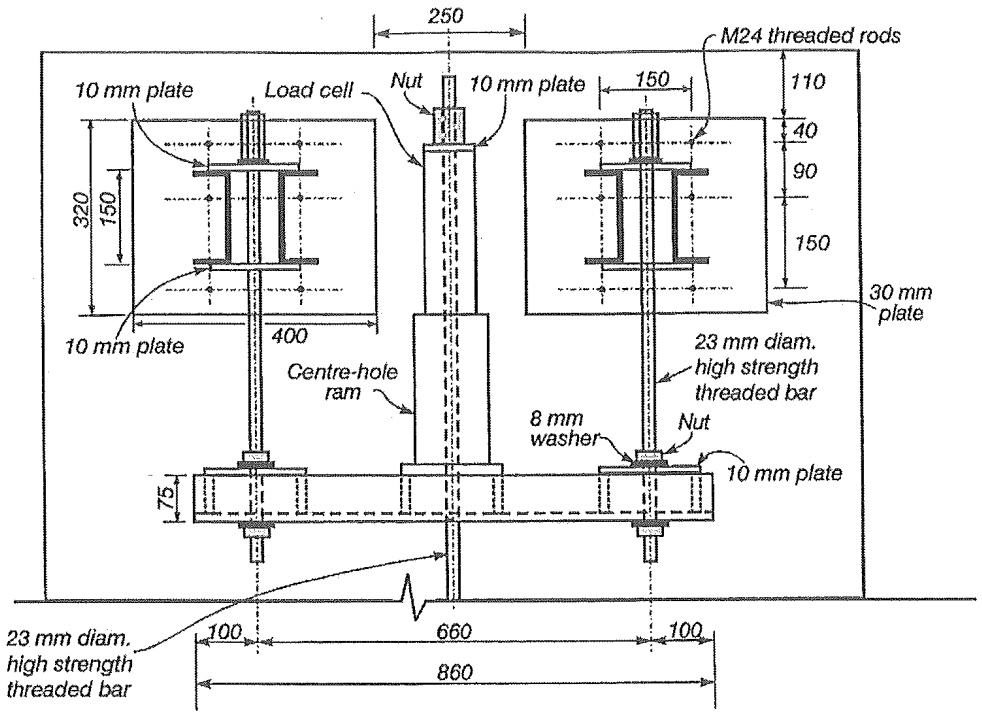

Figure 3.3 Detail of external post-tensioning arrangement used (Rahman and Restrepo, 2000).

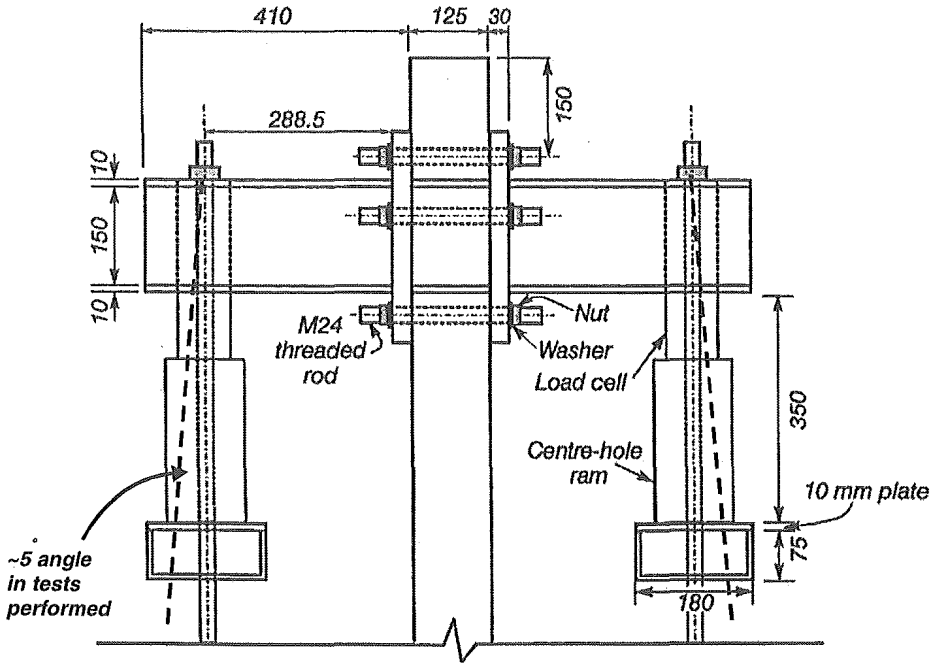

Load frame-wall connection detail

Figure 3.4 Side-view of external post-tensioning arrangement at top of units (Rahman and Restrepo, 2000).

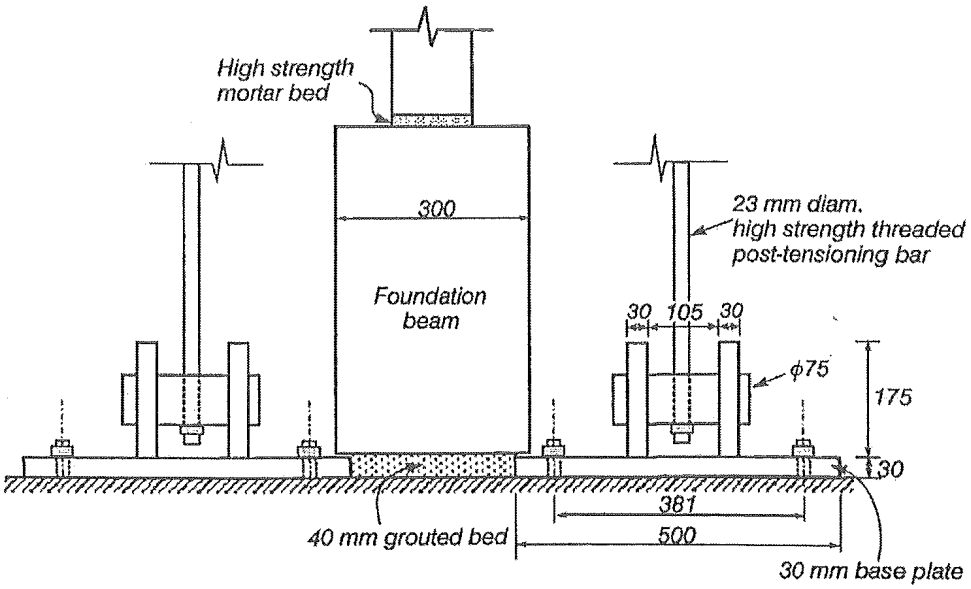

Strong-floor connection detail

Figure 3.5 Strong floor connection detail (Rahman and Restrepo, 2000).

Unlike in the Rahman and Restrepo tests, the external prestressing bars were not mounted vertically but approximately 5^{o} to the wall. This solution was necessary given that the strong floor bolts, that normally would have been used, were covered by the foundation beam. The width of the foundation beam being greater than that used by these researchers. This angle was slight therefore no alteration to the prestressing force was required in order to composite for the horizontal component of the load.

Post-tensioning of Unit 2 was provided by two 600kN capacity centre-hole hydraulic rams placed atop the wall, see rams R4 and R5 in Figure 3.2. A protective cover was placed above the wall in the case of failure of a rod or anchor. An initial post-tensioning force of 22kN per tendon (66kN per duct) was provided. Figure 2.48 in section 2.3.5 shows the completed post-tensioning apparatus.

Centre-hole hydraulic rams were mounted either end of the foundation beam located 250mm above the strong floor, see rams R6 and R7 in Figure 3.2. These were placed in order to prevent sliding of the foundation beam relative to the test floor on the application of lateral load. For both units these rams were stressed using a common line to150kN and locked prior to testing. These rams bore against the Western and Eastern columns of the loading frame. Bearing plates consisted of 10mm mild steel, cast into the foundation for Unit 1, and 20mm plates placed at either end of the foundation beam for Unit 2.

3.3 INSTRUMENTATION

3.3.1 Data Acquisition System

All measurements of displacement and strain recorded during the testing procedures were obtained through Data Logging Serial Boxes manufactured by the Civil Engineering Electronics Department. These serial boxes convert the output from the instrumentation to a digital signal which was then converted and recorded by a software program, Universal Data Logger (UDL), written by the Electronics Department. This software was set during experimentation to display in real time the hysteretic response of Lateral Load versus Displacement. Data was recorded through user-defined trigger conditions. Typical trigger values used were: Lateral Displacement of ±1kN; Lateral Displacement ±0.5mm.

3.3.2 Load Cells

All load cells were calibrated using an Avery universal testing machine. The in-plane horizontal load applied through the hydraulic ram was measured by a 440kN load cell mounted between the hydraulic ram and the pinned connection plate, see loadcell L1 in Figure 3.2. The axial load applied through the twin centre hole hydraulic rams set each side of the wall was measured through two 150kN load cells, mounted between the hydraulic ram and the lock nut on the external prestressing bars, see loadcells L2 and L3 in Figure 3.2. The prestressing force in Unit 2 was applied through the two centre hole hydraulic rams set atop the wall. The force exerted was measured by two 300kN load cells, mounted between the hydraulic rams and the anchor plate, see load cells L4 and L5 in Figure 3.2. The force applied by the centre-hole ram at the foundation beam ends was monitored through a pressure gauge.

3.3.3 Displacements

Figure 3.6 shows the deployment of instrumentation used to monitor displacements and deformations in Units 1 and 2. The in-plane lateral displacement of each unit was monitored by two linear potentiometers aligned with the actuator providing the lateral force. A 300mm linear potentiometer, see P22 and P15 in Figures 3.6 (a) and (b), respectively, measured the entire lateral displacement regime. An additional 30mm spring loaded potentiometer was attached in parallel to increase the resolution of the readings at the low amplitude displacements, see P21 and P14 in Figures 3.6 (a) and (b), respectively.

For Unit 1 the role of potentiometers P1 to P16 were as follows,

Potentiometers P1 to P10:	To obtain rotation and average curvature of the wall panel.
Potentiometers P11 to P16:	To obtain shear displacements, including sliding shear at the wall panel-foundation beam interface (P15 and P16 anchored at the foundation beam).

For Unit 2 the role of potentiometers P1 to P12 were as follows,

Potentiometers P1 and P6:	To obtain rotation and average curvature of wall panel (expected to be negligible).
Potentiometers P7 and P8:	To obtain the base rotation caused by the opening of the joint. These were also used to calculate the average strains in the energy dissipators and additional strain in the carbon fibre tendons due to rocking.
Potentiometers P10 to P12:	To obtain the rotation and average curvature of the foundation beam.

Note that no diagonal potentiometers were placed in the wall panel of Unit 2 as shear deformations were expected to be small due to the wall panel being designed to behave essentially uncracked.

Horizontal movement (sliding) of the foundation beams with respect to the test floor was measured using a 30mm travel linear potentiometer, see P20 and P13 in Figures 3.6 (a) and (b), respectively. These were attached to an independent steel frame located at the mid-height of the western end of the foundation beam. Potential sliding of the wall panel of Unit 2 relative to the foundation beam monitored through a 30mm travel linear potentiometer, see P9 in Figure 3.6 (b).

Rotation of the foundation beams were measured using 30mm travel potentiometers, see P18 and P19 in Figure 3.6 (a) and P10 to P12 in Figure 3.6 (b). Potentiometer P11 was placed in Unit 2 as the foundation beam rotation was expected to be significantly increased by the large vertical forces due to prestressing and the energy dissipators.

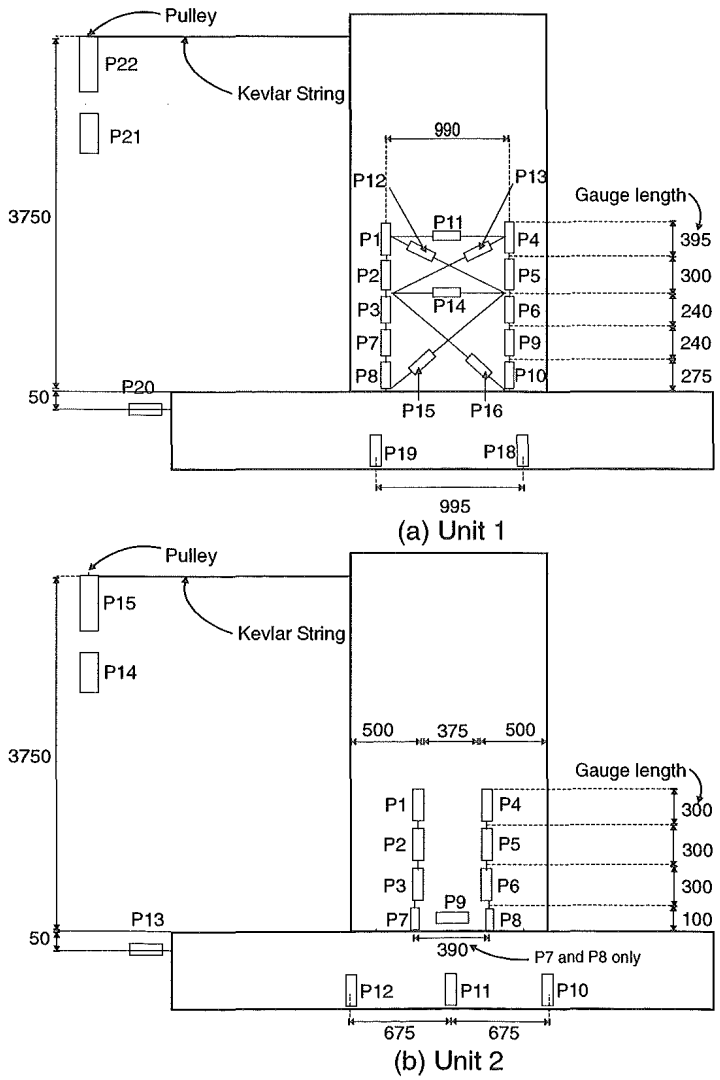

Figure 3.6 Schematic representation of the external instrumentation for monitoring displacements and deformations in the unit tested.

3.3.4 Reinforcement Strains

Electric foil strain gauges, (Tokyo Sokki type FLA-5-11-3L), with 5mm gauge length, were used to monitor longitudinal strains in the reinforcing bars in Units 1 and 2. Application consisted of removing the bar deformations before preparing the surface with emery paper and cleaning it with MEK. Once applied, each gauge had 3 coats of a water proofing compound added and securely wrapped mastic tape. The location of the strain gauges used in both units is shown in Figure 3.7.

For Unit 1, strain gauges were attached to either side of the external most longitudinal bars. Pairs of gauges were spaced at 150mm below the base of the wall as well as 50mm and 150mm above. These were placed in order to find the level of dissipation at which yielding of the longitudinal reinforcement commenced. One set of strain gauges was also attached to the threaded bars which were passed through either end of the wall as part of the recess connection with the foundation beam. These were used to indicate whether or not the recess connection was performing as designed.

For Unit 2, strain gauges were attached to the eastern half of the unit only. They consisted of three sets of strain gauges spaced 50mm, 300mm, and 500mm from the base of the longitudinal reinforcement. Three sets of strain gauges were also attached to the diagonal reinforcement. These were placed at the same vertical heights as those attached to the longitudinal bars. The purpose of these gauges were to determine whether yielding occurred as well as to gain an insight into whether the strut-and-tie model assumed in fact developed (refer section 2.3.2.1). Three sets of strain gauges were placed on the bottom most and second highest placed stirrups. (Two sets 200mm from each end with the remaining set placed mid-length) These gauges were mounted in order to determine the proportion of the force that flowed through the alternative load path previously outlined in Figure 2.24 in section 2.3.2.1.

Two strain gauges were attached to either side of the energy dissipators, 20mm above the milled section of the bar, see Figure 3.8. These gauges were used in calibrating axial load versus strain on an Avery universal testing machine in order to obtain the forces developed during testing. Figure 3.9 shows one of the dissipator bars prior to calibration. The section of bar beneath the milled segment was removed after calibrating, with a 35x35 20mm anchor plate welded to the end, see Figure 3.8.

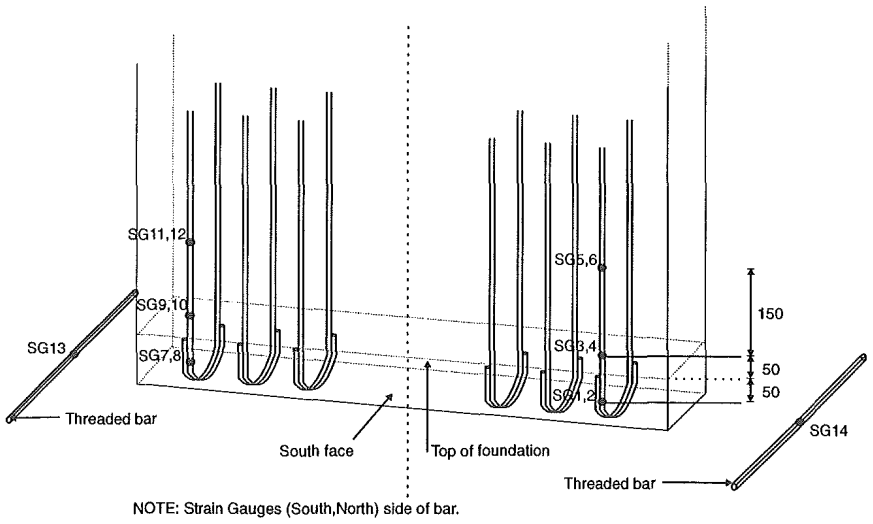

(a) Unit 1

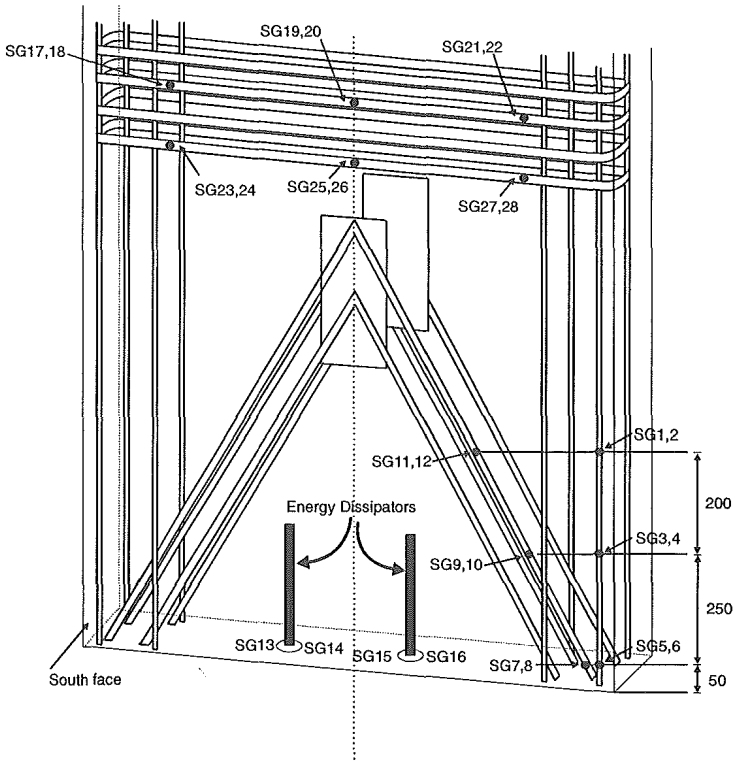

(b) Unit 2

Figure 3.7 Schematic representation of the position of strain gauges in the reinforcing bars of Units 1 and 2.

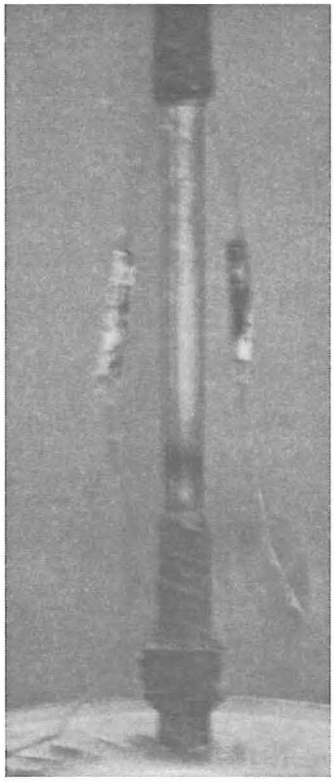

Figure 3.8 Detail of tapered energy dissipator.

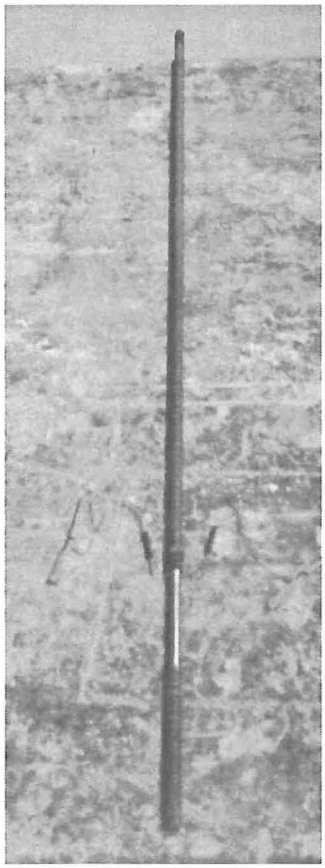

Figure 3.9 Energy dissipator prior to calibration.

3.4 MATERIAL PROPERTIES

3.4.1 Concrete and grout

Compression tests were completed on all concrete and grout admixtures at various stages of curing. Typically, 8 test cylinders were prepared for each concrete and grout mix. This ensured that there were enough specimens with which to calculate average strengths at the various stages of curing. Cylinder sizes range from 100mm diameter by 200mm long for concrete samples, to 50mm diameter by 100mm long for grout samples. All cylinders were tested on a 500kN Avery compression machine.

Table 3.1 Concrete and grout test properties for Units 1 and 2.

Location	Cylinder Size	Curing Method	No. of Tests	Age (days)	f'_c (MPa)
Wall panel +	100x200	Cured with unit	6	10	38.8
Foundation beam			5	28	43.5
(Unit 1)			4	38(testing)	45.8
Wall panel*	100x200	Cured with unit	3	16	29.7
(Unit 2)			3	28	35.1
			2	34(testing)	36.0
Foundation beam	100x200	Cured with unit	3	16	33.7
(Unit 2)			3	28	39.3
			2	34(testing)	39.5
Grout : Recess	50x100	Cured with unit	4	10(testing)	60.0
(Unit 1)					
Grout :	50x100	Cured with unit	5	8(testing)	47.0
Dissipator Ducts					
(Unit 2)					

* It was noted that the fibre reinforced concrete for Unit 2 maintained its load carrying capacity for a significant duration after f'_c had been achieved.

3.4.2 Reinforcing steel

The reinforcing steel for both Units 1 and 2 consisted of Hot-Rolled deformed bars. Typically three samples of each bar were tested in order to obtain a reasonable average. Testing was performed on a 1000kN Avery universal testing machine. Strains were measured using with a 30mm clip-gauge, with strain and load data captured electronically through a serial data acquisition box and computer. Only samples, where the exact material properties were required, were tested.

Table 3.2 Summary Tensile Properties of Unit 1 wall reinforcement.

Bar Designation	Area (mm^2)	Location	f_y (MPa)	f_{su} (MPa)	ε_{sh} (%)	ε_{su} (%)
HD10 Unit 1	78.5	Longitudinal Wall panel	476	611	2.26	13.0
HD16 Unit 2	201.1	Longitudinal Wall panel	464	609	2.13	17.6
HD16 Unit 2	201.1	Longitudinal Foundation beam	517	672	1.29	17.5
R6 Unit 1	28.3	Stirrup Wall panel	336	453	1.16	9.8
R6 Unit 1	28.3	Stirrup Foundation beam	334	446	1.05	11.2
R6 Unit 2	28.3	Stirrup Foundation beam	315	424	0.74	12.0

3.4.3 Energy dissipators

Two strain gauges were attached to either side of the energy dissipators, 20mm above the milled section of the bar, see Figure 3.8. These gauges were used in calibrating axial load versus strain on a 1000kN Avery universal testing machine. A axial tensile force of up to 50kN was applied to the dissipators.

The diameter of the dissipators was carefully measured at several intervals to ensure a near constant diameter. The diameter of the milled portion was 15.8mm for each bar. Figure 3.9 shows the eastern dissipator bar prior to calibration.

400mm off-cuts from each dissipator bar were used in order to obtain the ultimate tensile capacities, shown in Table 3.3. Note, both dissipators were milled from the same batch of reinforcement.

3.4.4 Carbon Fibre Tendons

The carbon fibre rods used in the post-tensioning of Unit 2 had a nominal diameter of 5.5mm, and unbonded length of 5100mm between anchors. A 300mm long sample with identical anchors to those of the test specimens was tested in an 1000kN Avery universal testing machine. 2mm strain gauges were attached to both sides of this rod in order to obtain the stress-strain relationship of the carbon fibre tendon. Figure 3.10 shows in detail the epoxied end anchor of one of these carbon fibre tendons.

3.4.5 Dramix Steel Fibres

Details concerning the recommended dosages of steel fibre reinforcement are discussed in Whiteside, 2000. Gives the properties of the fibres used in the admixture for casting the wall panel of Unit 2.

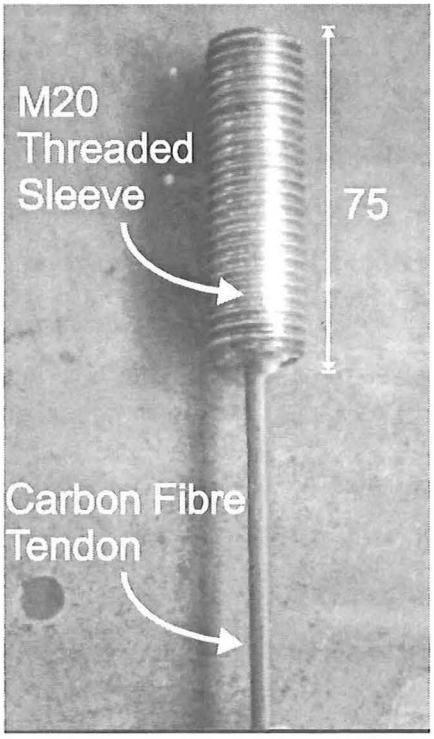

Figure 3.10 Detail of epoxied anchor of carbon fibre tendon.

Table 3.3 Material properties of tapered energy dissipators.

Bar Type	Area (mm^2)	Reduced Area (mm^2)	f_y (MPa)	f_{su} (MPa)	ε_y (%)	ε_{sh} (%)	ε_{su} (%)
HD20	314	196	464	593	0.21	3.43	16.9

Table 3.4 Material properties of BBR carbon prestressing tendons.

Diameter (mm)	Area (mm^2)	f_{su} (MPa)	ε_{su} (%)	E_p (GPa)
5.5	23.8	2289	1.37	166
Specified (mm)	**Area (mm^2)**	**f_{su} (MPa)**	**ε_{su} (%)**	**E_p (GPa)**
5.5	23.8	2350	1.47	160

Table 3.5 Geometric properties of the Dramix Steel Fibres.

Fibre Type	Length, L (mm)	Diameter, d (mm)	L/d
RC-65/35-BN	35	0.55	64

3.5 TESTING SCHELDULE

Loading of both units comprised of quasi-static lateral displacement based cycles. This test regime is identical to the one used by Rahman and Restrepo (2000), for the test of Unit 3 as plotted in Figure 3.11. Initial cycles to ±0.25% and ±0.5% lateral drift were completed. For Unit 1 these cycles were within the elastic range which allowed the stiffness and yield displacement of the wall to be established.

Subsequent cycles composed of two-large amplitude cycles followed by one cycle at a level corresponding to the last lower drift level. A jump of 0.5% drift between larger cycles was set. This schedule was completed up to 3% lateral drift for Units 1 and 2. The application of the lateral displacement was at a height of 3.75m above the foundation beam.

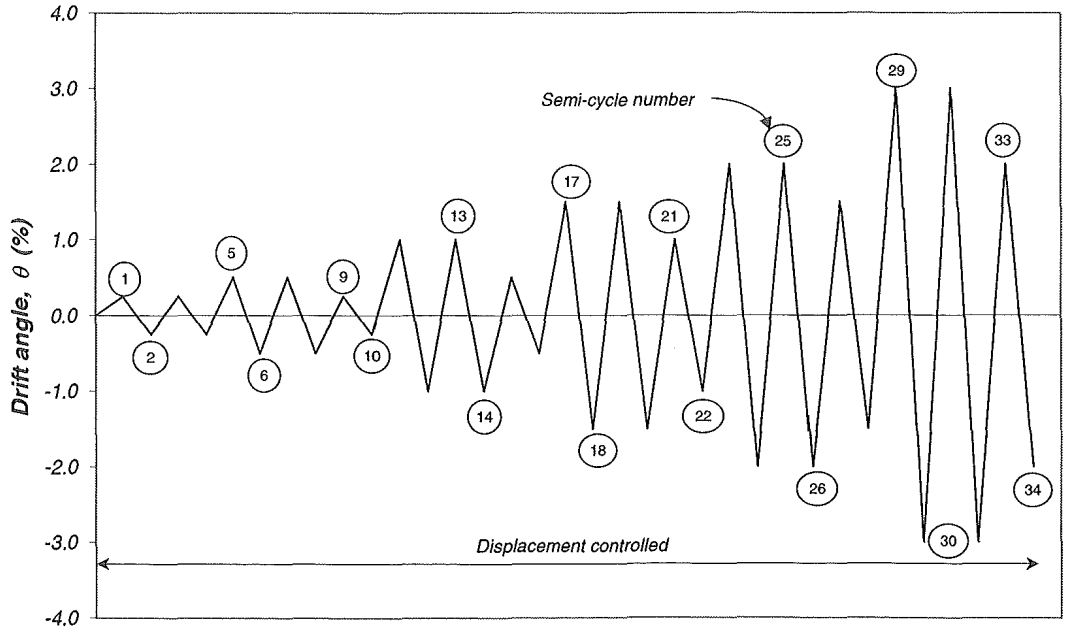

Figure 3.11 Testing schedule.

4 RESULTS AND OBSERVATIONS

4.1 GENERAL

Positive semi-cycles are those obtained by loading from East to West. Conversely, negative cycles are those cycles obtained by loading from West to East.

Semi-cycles are denoted though the direction of load, level of drift obtained, and the number of times that this drift has been obtained. For example +1.0x2 identifies the second time the unit has been displaced to 1.0% drift in the positive direction.

The south side of both units can be identified through the potentiometers mounted on this face.

4.2 RESULTS FOR UNIT 1

4.2.1 Behaviour and Observations of Unit 1

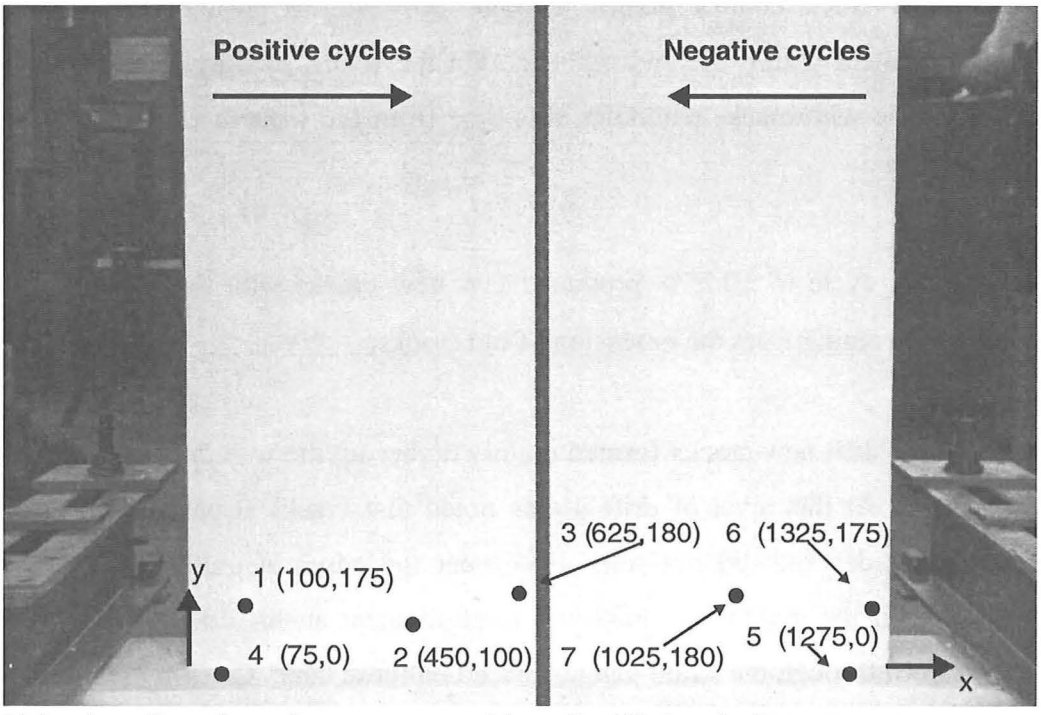

Note : Location of cracks are measured from the Western bottom corner. (North face showing)

Figure 4.1 Location of points for establishing crack widths.

Crack widths were measured in the wall panel of Unit 1 at a number of locations. Measurements were taken at both peak and unloaded semi-cycles up until widths in excess of 4mm were observed. The locations at which these measurements were taken are shown in Figure 4.1. For Unit 1 a 200x200 grid was drawn upon the North face of the specimen in order to help establish the magnitude and orientation of the cracks within the plastic hinge zone. This grid extending 1000mm from the top of the foundation.

Cracking of the unit was observed from the very first cycle to +0.25% drift. These cracks were only 0.1mm wide at the peak load and closed completely once the unit was unloaded. The extent of these cracks covered approximately 2/3 the width of the wall, and extended 1.4m up from the foundation, see Figure 4.2. Within the first 200mm from the edges the spacing of cracks was observed as being approximately 60mm. This corresponds to the transverse confinement and anti-buckling reinforcement spacing along the edges. Past 200mm, these cracks begin to converge resulting in crack spacings of approximately 180mm. This corresponds to the transverse reinforcement spacing found within the remainder of the unit. It was also noted that the width of these cracks was greater than those found closer to the edges. These observations highlight the improved crack control gained through providing a greater level of longitudinal reinforcement within the end regions. On the return semi-cycle similar observations were made with cracks extending this time from the western edge across the unit, see Figure 4.3.

A second cycle to ±0.25% produced few new cracks with the majority of observed cracking coming from the extension of old cracks.

At +0.5% drift new cracks formed mainly higher up the wall due to the greater applied moment. At this level of drift it was noted that cracks at peak loading had become slightly wider and did not fully close near the edges at unloading. This suggested yielding of the external longitudinal reinforcement at this drift level which was later confirmed through the strain gauges placed on these bars. Cracking at this level of drift had extended to approximately two-thirds the wall height. Yielding had spread approximately 300 mm upwards as suggested by the residual crack widths of 0.2mm or

greater. The reverse cycle showed identical behaviour to that described for the positive cycle.

A second cycle at 0.5% drift resulted in the extension of old cracks. At this drift level cracks from loading in one direction began to prominently connect with cracks formed through loading from the opposite direction, see Figure 4.4. As will be discussed later on yielding of the outermost longitudinal bars occurred in these cycles. The reference yield drift was found to be $\theta_y = 0.5\%$.

At the first semi-cycles to ±1.0% drift wide cracks began to develop within the wall panel. The widest crack measured of 2.2 mm was recorded at point 7, see Figure 4.1. The maximum residual crack width was also recorded at point 7, being 2.0 mm. Residual drift could be observed through the naked eye.

Repeated semi-cycles to ±1.0% produced few new cracks within the plastic hinge zone. Figure 4.6 illustrates the residual crack widths within the plastic hinge zone after unloading from semi-cycle -1.0x2.

At semi-cycle +1.5x1 a slight pullout of the wall at the western corner was observed. The extent of this movement was limited to this initial pull-out, being in the order of 5mm at the eastern most edge. Tension cracking was also noted at the eastern corner of the wall, first becoming visible at semi-cycle –1.5x1. Shear deformations became apparent at subsequent cycles at this level of drift, see Figure 4.7.

Spalling of the cover concrete occurred at both ends of the wall at the initial semi-cycles to ±2.0%, see Figure 4.8. The extent of spalling was approximately 50mm from the base of the wall and through 20mm of the cover concrete. Spalling became more extensive in the subsequent semi-cycles at this level of drift.

Continued spalling of the cover concrete occurred to 2.5% drift where at semi-cycle +2.5x2 the north-eastern corner longitudinal bar began to show the first signs of incipient bar buckling, see Figure 4.9. A small white "compression" crack was noted

within the region of buckling. –2.0x2 saw a similar effect on the outermost north-western bar.

After the completion of semi-cycles ±2.5x2, a third set of semi-cycles were completed to 2.0% drift. Fracture of the outermost north-western longitudinal bar occurred at the peak of semi-cycle –2.0x3. This bar had previously buckled during the last positive semi-cycle. At this point the lateral load capacity decreased substantially to the point of failure of the unit.

Complete failure of Unit 1 was determined at an imposed drift of 3.0%. The eastern outermost bars fracturing at the semi-cycle to +3.0x1. Extremely large cracks ran through the plastic hinge zone in particular, with the majority remaining open upon the unloading of the structure, see Figures 4.10 and 4.11. Extensive spalling at the corners of the wall caused much of the longitudinal steel to buckle resulting in the unit being virtually unrepairable. A significant level of residual drift was also evident upon unloading, see Figure 4.12.

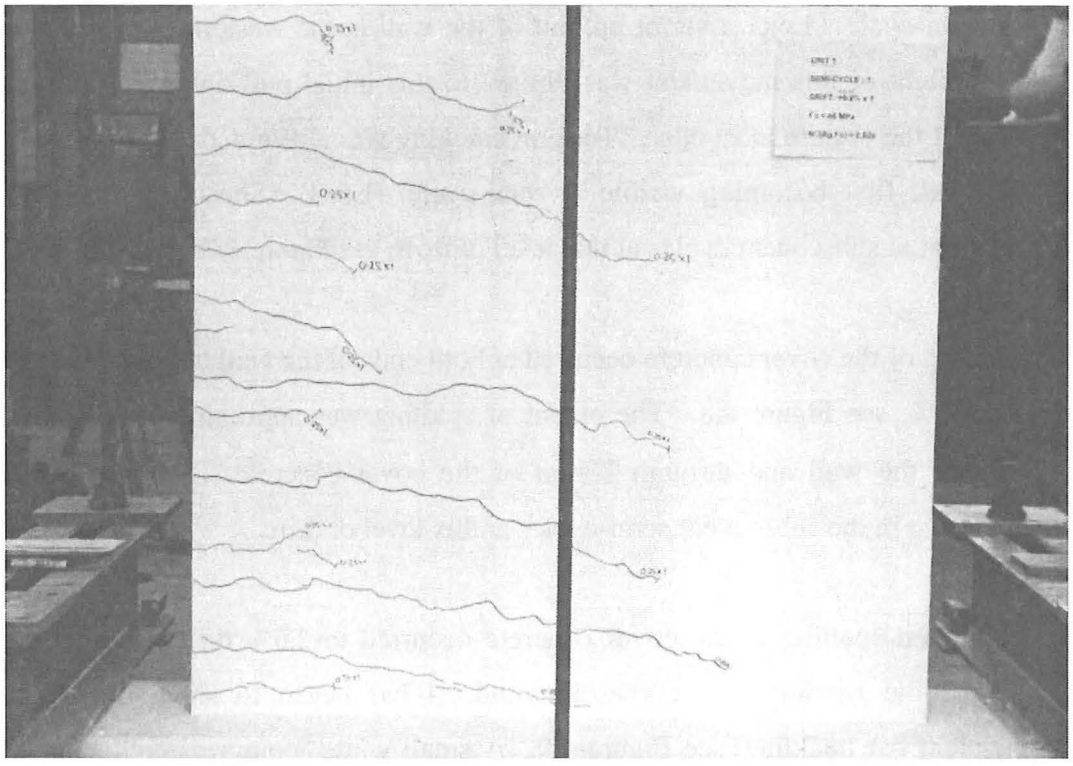

Figure 4.2 North face of Unit 1 at +0.25x1.

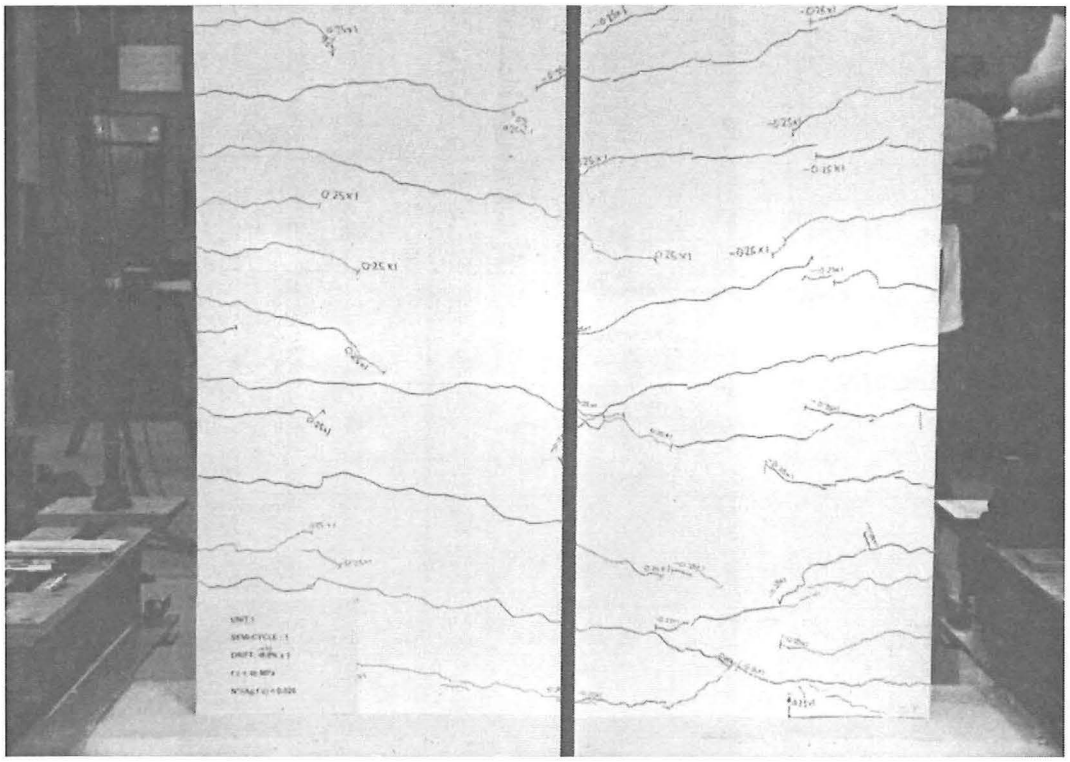

Figure 4.3 North face of Unit 1 at –0.25x1.

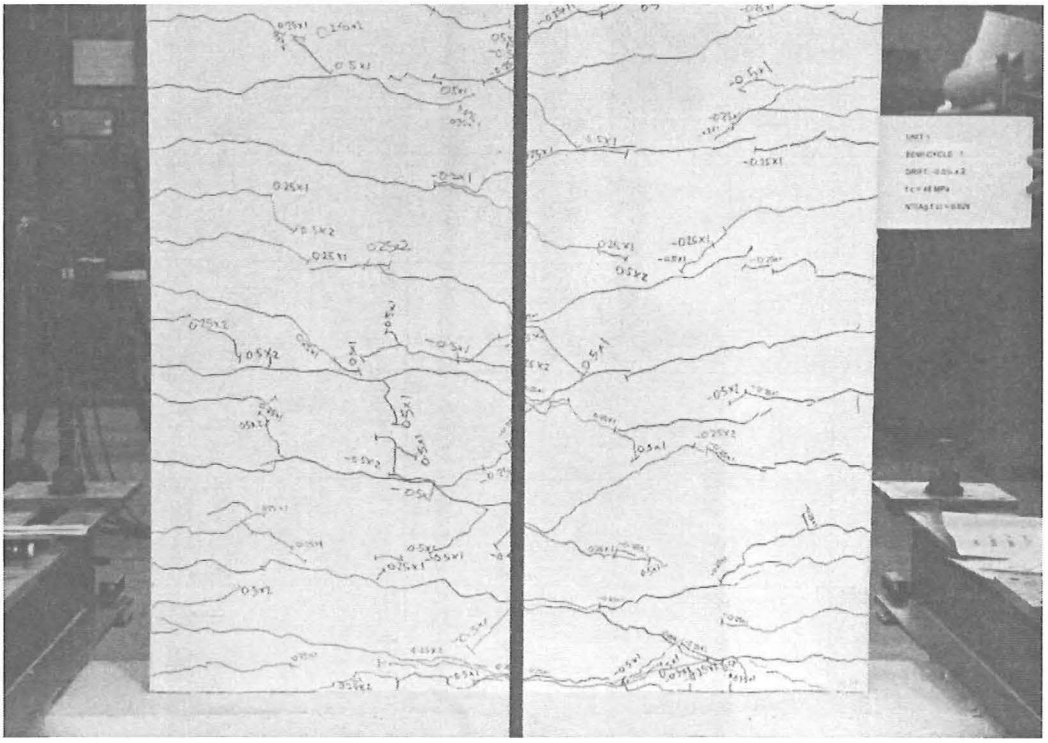

Figure 4.4 North face of Unit 1 at -0.5x2.

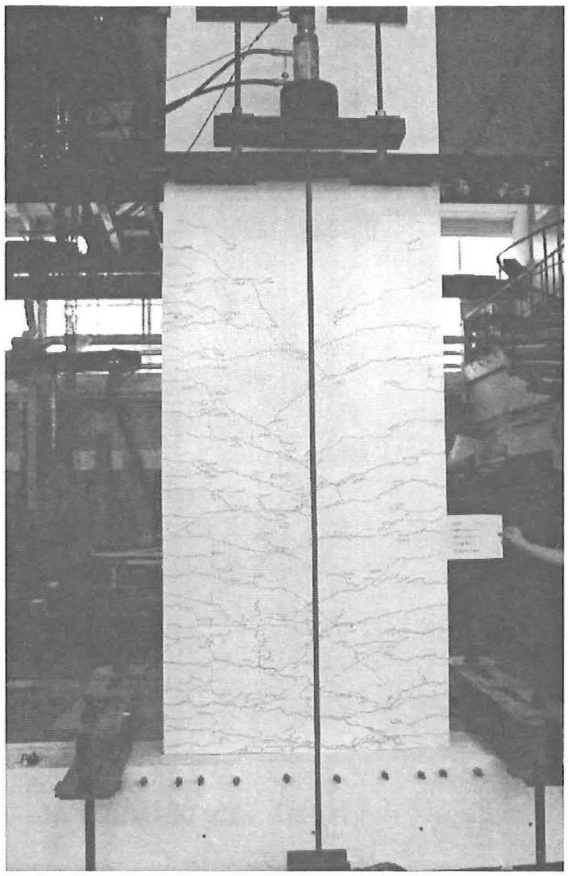

Figure 4.5 North face of Unit 1 at +1.0x1.

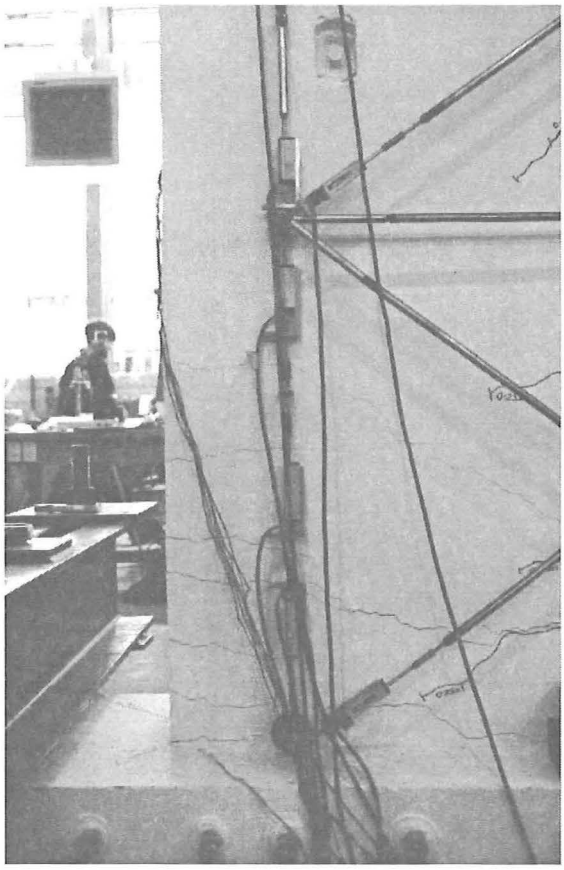

Figure 4.6 Residual cracking in the south-western corner of Unit 1 after –1.0x2.

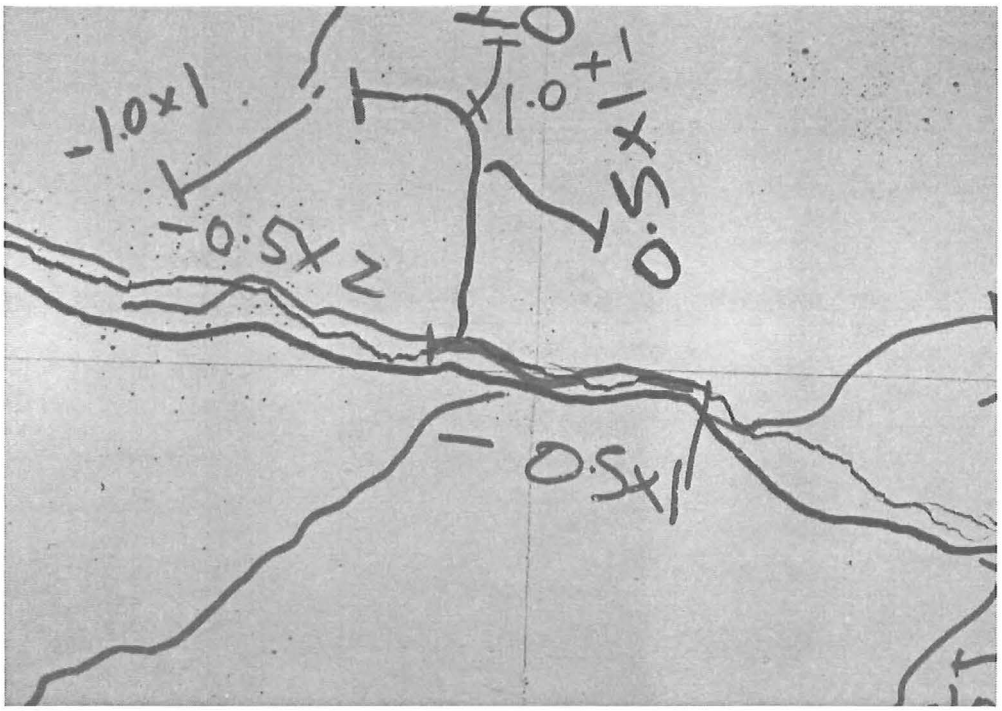

Figure 4.7 Initial visible signs of shear deformation at –1.0x2.

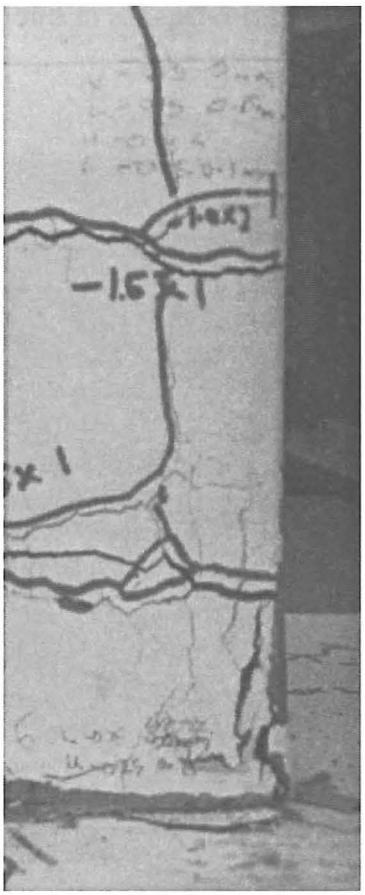

Figure 4.8 Initial spalling of cover concrete in the north-western corner of Unit 1 at –2.0x1.

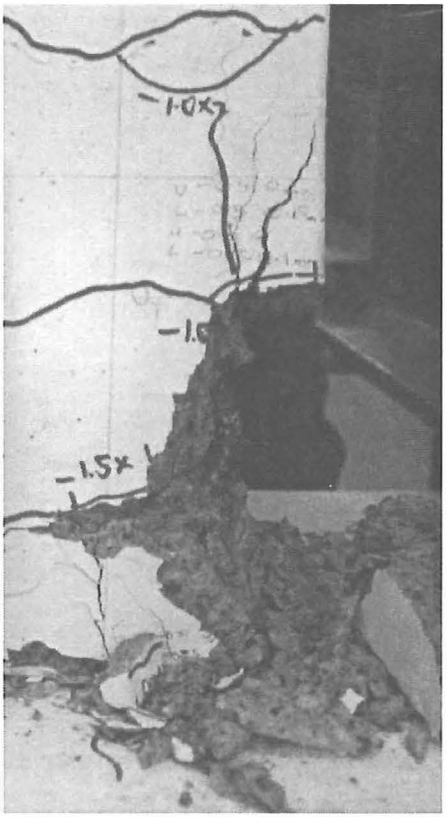

Figure 4.9 Initial stages of bar buckling +2.5x2.

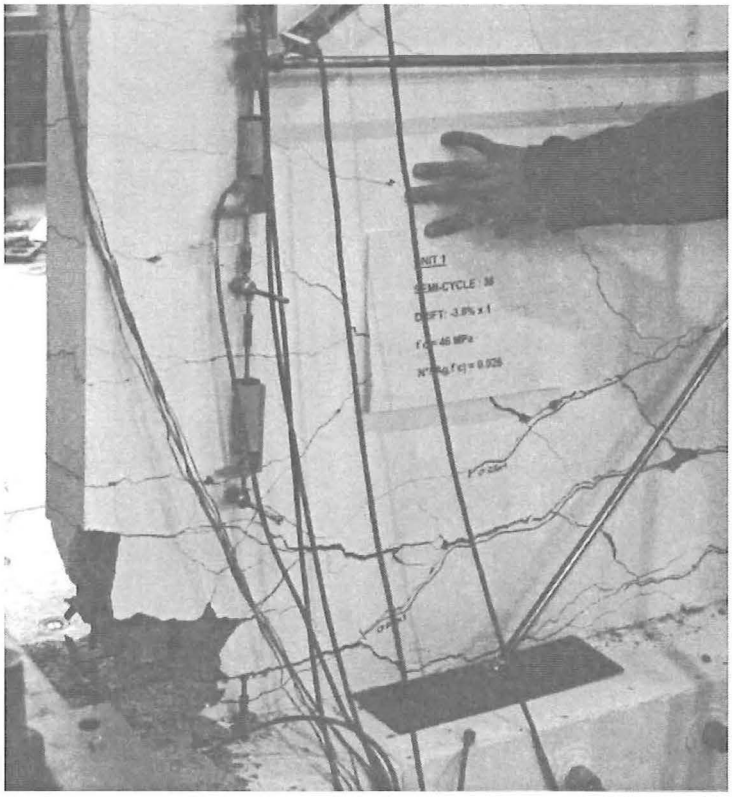

Figure 4.10 Fractured longitudinal bars at -3.0x1.

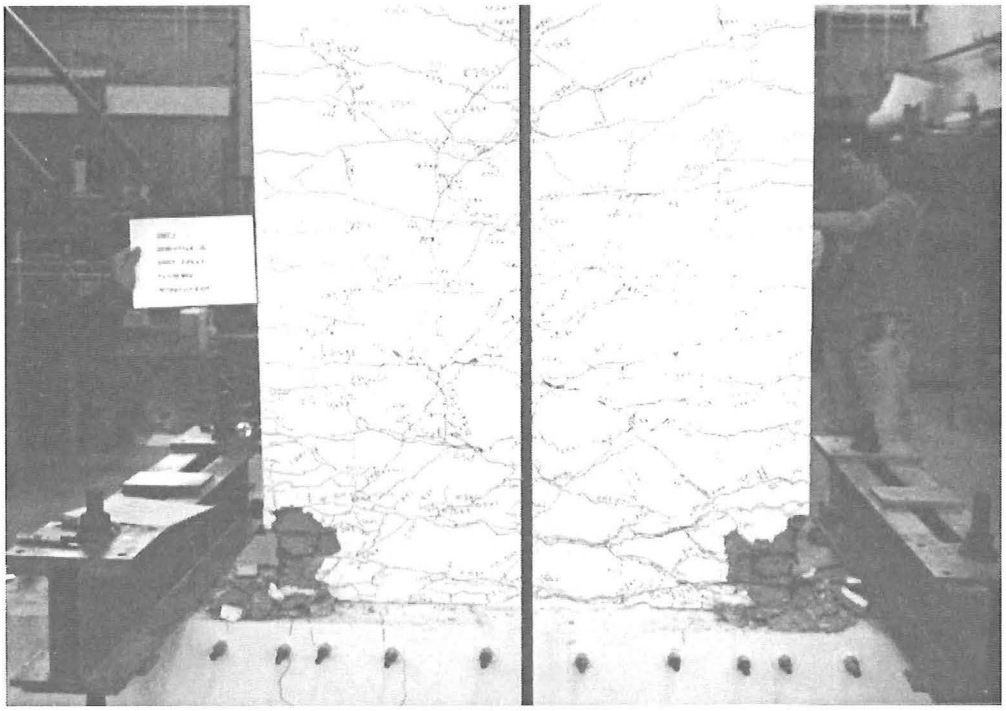

Figure 4.11 View of the north face of Unit 1 at the end of test (after –3.0x1).

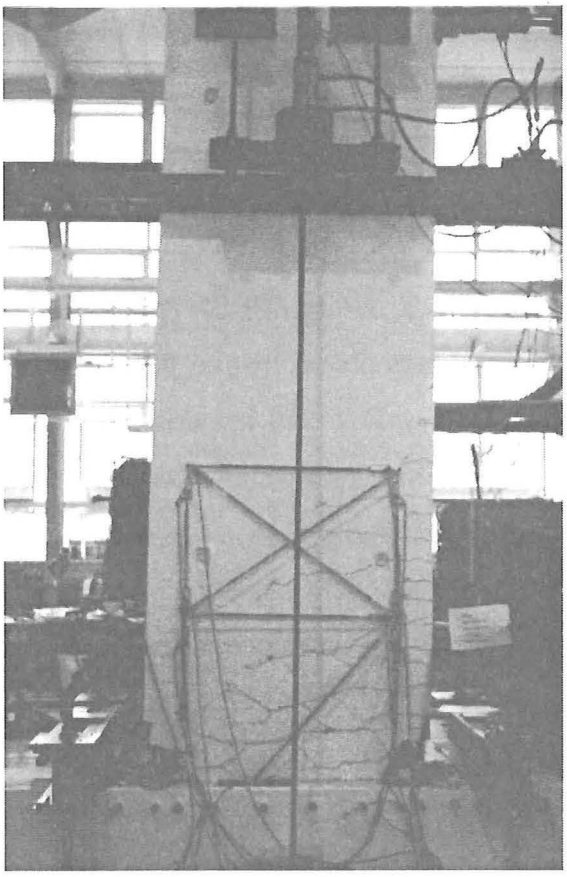

Figure 4.12 Residual drift after –3.0x1.

4.2.2 Analysis of Experimental Results for Unit 1

The performance of Unit 1 was close to that predicted analytically, showing typical behavioural characteristics of a conventionally monolithic reinforced concrete structural wall. Energy was dissipated mainly through yielding of the longitudinal wall reinforcement at the plastic hinge region. The connection of the wall to the foundation beam had no influence on the overall response of the unit. Adequate detailing of the plastic hinge zone allowed the structural to deform in a ductile manner, surpassing the 2.0% lateral drift design limit. Minimum design provisions in the Concrete Structures Standard governed the ultimate capacity of the Unit 1, which eventually obtained 2.5% lateral drift before significant loss in capacity occurred.

Figure 4.13 illustrates the hysteretic behaviour of Unit 1. The shape and size of the loops are typical of that expected for a cast-in-place concrete structural wall. In addition, the theoretical backbone curve found from a fibre model is provided. The theoretical capacity found using the method given in the Concrete Structures Standard (NZS 3101, 1995) using the measured material properties is also shown. The actual capacity of Unit 1 is very similar to that obtained from the standard. The theoretical backbone gives a relatively close approximation to the measured response, suggesting only a slightly greater capacity at the higher drift levels.

The hysteretic response up to 1% drift is illustrated in Figure 4.13. The yield point of the extreme longitudinal bars are plotted on this curve. Yielding was found to have taken place on the first cycle to ±0.5% drift at about 120kN lateral force. The theoretical backbone curve fits very well the response measured during this part of the test. The bi-linear representation of the response is also shown in this figure. The elastic stiffness and reference yield displacement shown are based on the secant line passing through the point at which first yielding was observed. The reference yield drift ratio obtained for this unit was 0.50%. Consequently, the ductility capacity of this unit was 2.5%/0.50% = 5.0, which is equal to the value selected in design.

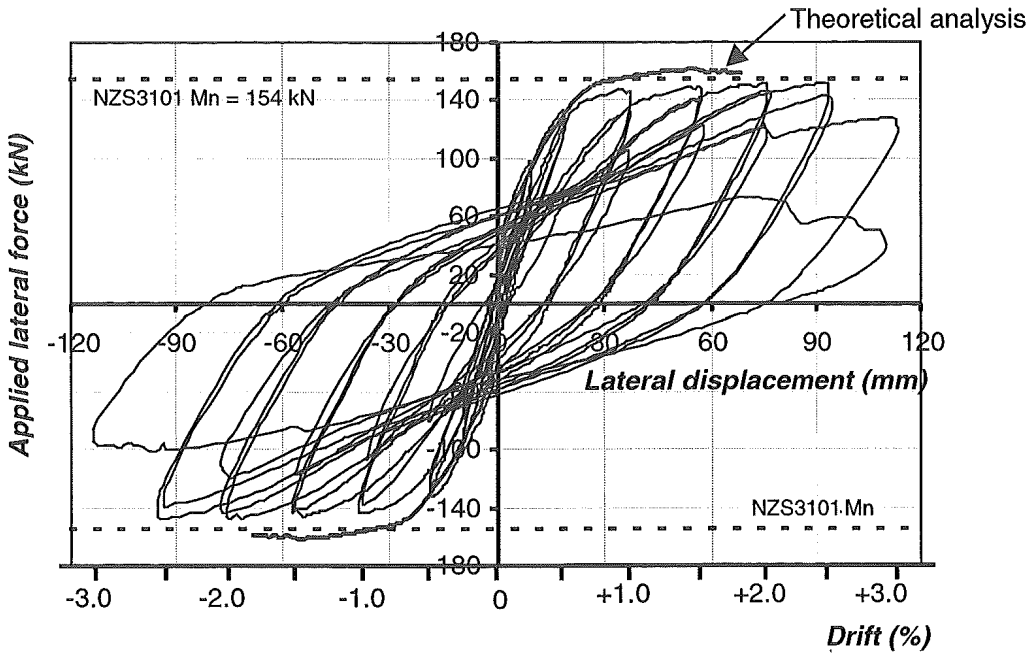

Figure 4.13 Full hysteretic response of Unit 1.

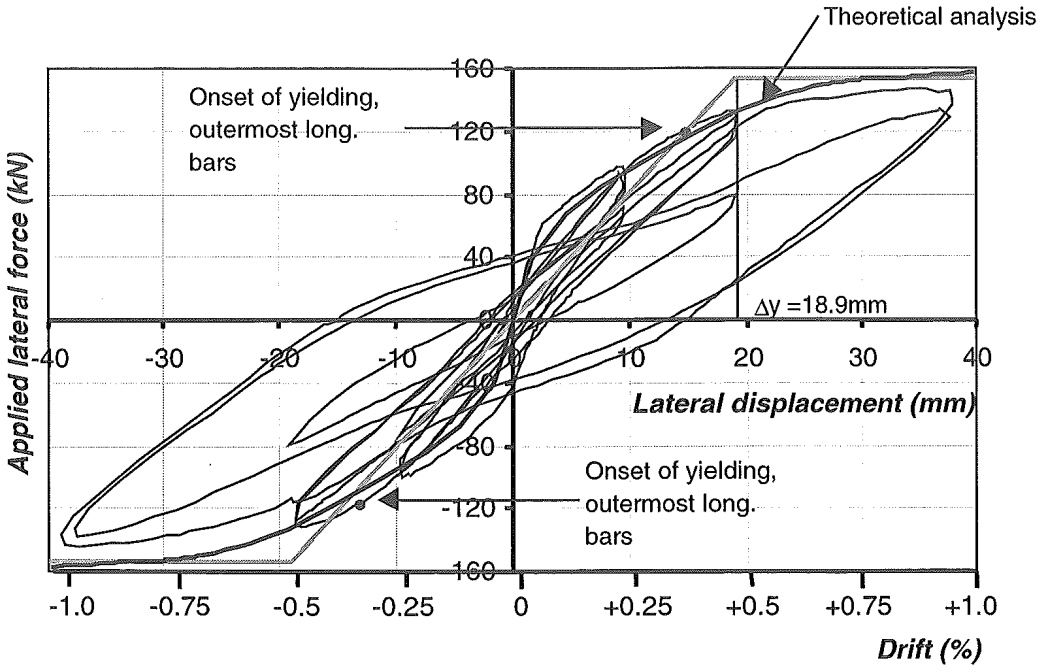

Figure 4.14 Hysteretic response of Unit 1 up to 1% drift.

By breaking down the hysteretic response into its individual cycles, the level of equivalent viscous damping for the structure can be obtained Chopra, 1995. Figure 4.15 illustrates how equivalent viscous damping increases from approximately 5% at 0.25% drift to 23.5% at 2.5% drift. The increase in damping in the cycles to 0.5% and beyond is mainly due to yielding of the longitudinal reinforcement. The first cycle from 0.25% to 0.5% lateral drift shows a drop off in damping due to the high levels of released energy that comes from the initial cracking of the specimen. In the cycles to large drift values the loss of damping in the second cycle can be attributed to the fact there is initial strain energy dissipated through concrete in compression. As the residual strains remain in the concrete, the amount of energy dissipated by the concrete is significantly reduced in the second cycle.

Figure 4.16 illustrates the residual drift of Unit 1 versus the peak drift obtained per semi-cycle. This plot clearly shows that initially residual drift is essential zero up until 0.5% lateral drift. At this drift level the onset of flexural yielding is attained, resulting in permanent deformations within inelastic portions of the member upon unloading. The percentage of residual drift was found to increase relatively linearly with higher cycles of applied lateral displacement. At 2.5% applied lateral drift, 1.5% residual drift remained upon unloading of the wall panel. This is a significant level of permeant deformation as evidenced in Figure 4.12. Residual drift seems to be essentially independent of the previous loading history with the 1st, 2nd and 3rd cycles at each level of drift essentially exhibiting identical behaviour.

The decomposition of the lateral displacements was achieved though the readings gained from the potentiometers placed on both the wall and foundation beam of Unit 1. Figure 4.17 identifies, flexural, shear deformations (occurring in the lower portion of the wall panel), and foundation beam rotation as the main components of the total lateral displacement applied. At each cycle the contribution from each type of deformation was plotted as a percentage of the total displacement applied at the top of the wall. This plot clearly shows that flexure deformations in the wall panel dominate the response, contributing approximately 85-90% of the total displacement. A flexural dominated response was expected given the geometry of the wall in addition to Unit 1 being designed in accordance with capacity design principles. Shear deformations contributed approximately 10%-15%, becoming more significant in the final stages of

the test as a result of the reduction in shear stiffness caused by the opening of diagonal cracks in the plastic hinge region. Foundation beam rotations accounted for roughly 5% of the total displacement, during the easily stages of testing. Their contribution diminished as the applied drift was increased and the behaviour of the wall began to dominate the response. For each semi-cycle the total deformation obtained from instrumentation ranged between 75 to 95% of the total lateral displacement applied. The remaining deflection that is not accounted for may be put down to experimental error, as well as elastic deformations in the upper portion of the wall panel where instrumentation was not placed.

Figure 4.18 plots the curvature distribution in the wall panel. Also shown in this figure is the theoretical first yield curvature associated with yielding of the outermost longitudinal bars, illustrating the spread of yielding in the wall. The first yield curvature obtained from the linear potentiometers P8 and P10, see Figure 3.6 (a), gave a first yield curvature at the onset of yielding of the outermost longitudinal bars during the semi-cycle to +0.5x1, equal to 0.003 rad/m. This value compares well with the theoretical value of 0.0025 rad/m obtained from the fibre model accounting for flexure and shear deformations. It is evident that the theoretical yield curvature was exceeded during the cycles past ±0.5%, which agrees with the observations obtained from the strain gauges placed on the outermost longitudinal bars. The spreading and hence the development of the plastic hinge as the drift increased is clearly seen in Figure 4.18. Yielding had spread about 1200mm from the base of the wall once the applied drift had reached ±2.5%. Though strain gauges SG3/SG4 and SG9/10, see Figure 3.7 (a), indicated the onset of yielding of the outermost bars they failed to provide useful information in the cycles beyond 0.5% drift.

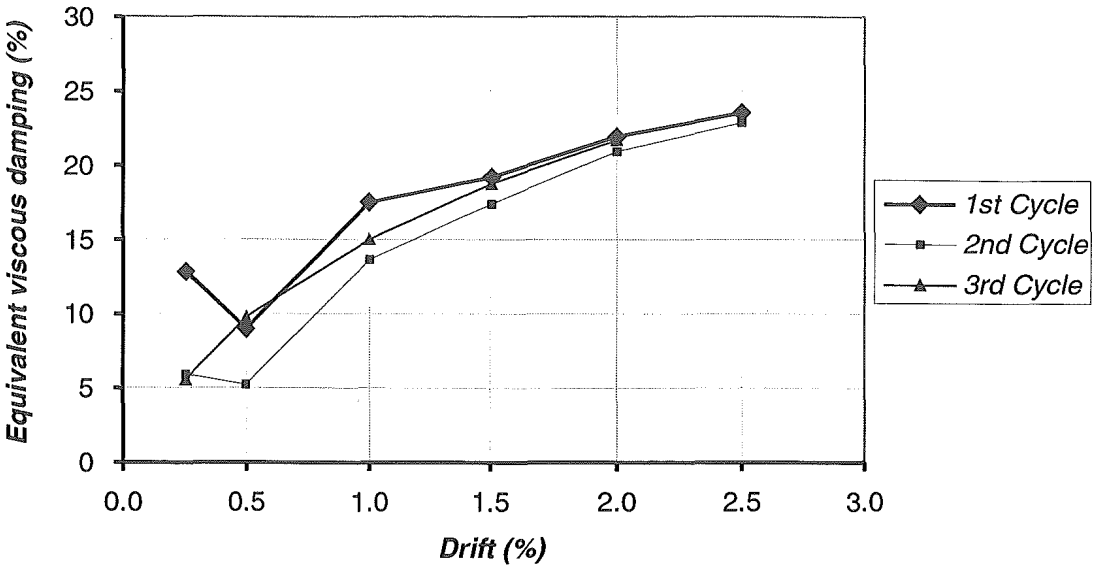

Figure 4.15 Equivalent viscous damping determined from the hysteretic response of Unit 1.

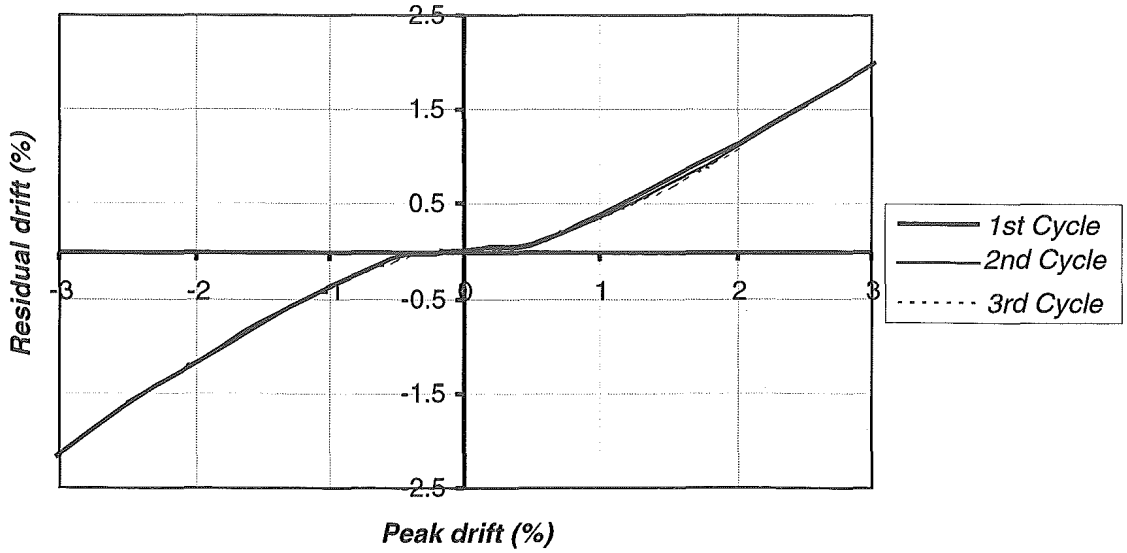

Figure 4.16 Peak drift versus residual drift recorded for Unit 1.

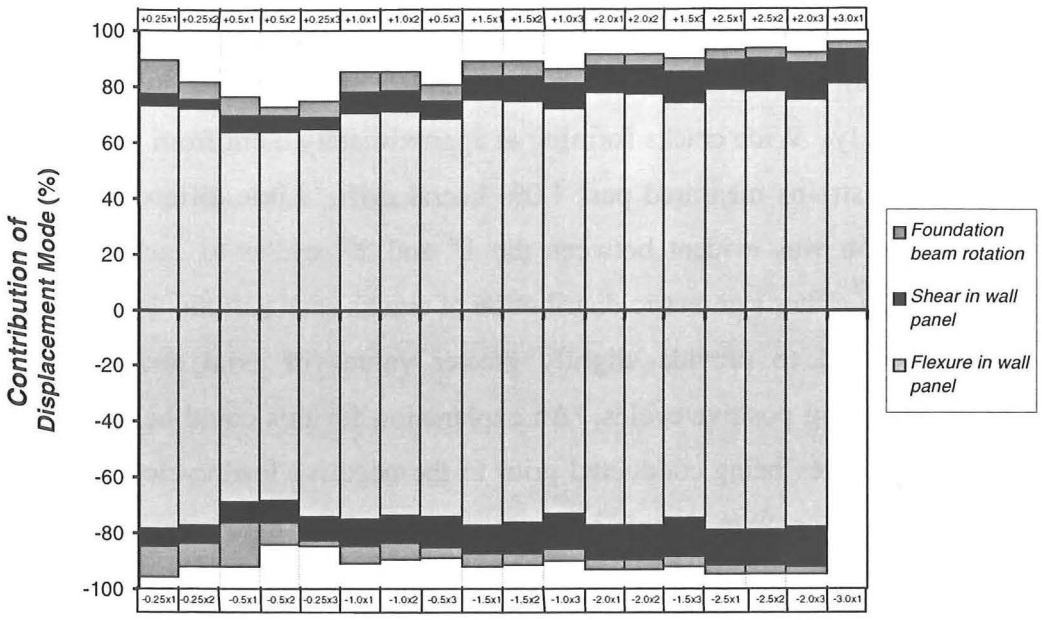

Figure 4.17 Decomposition of lateral displacements in Unit 1.

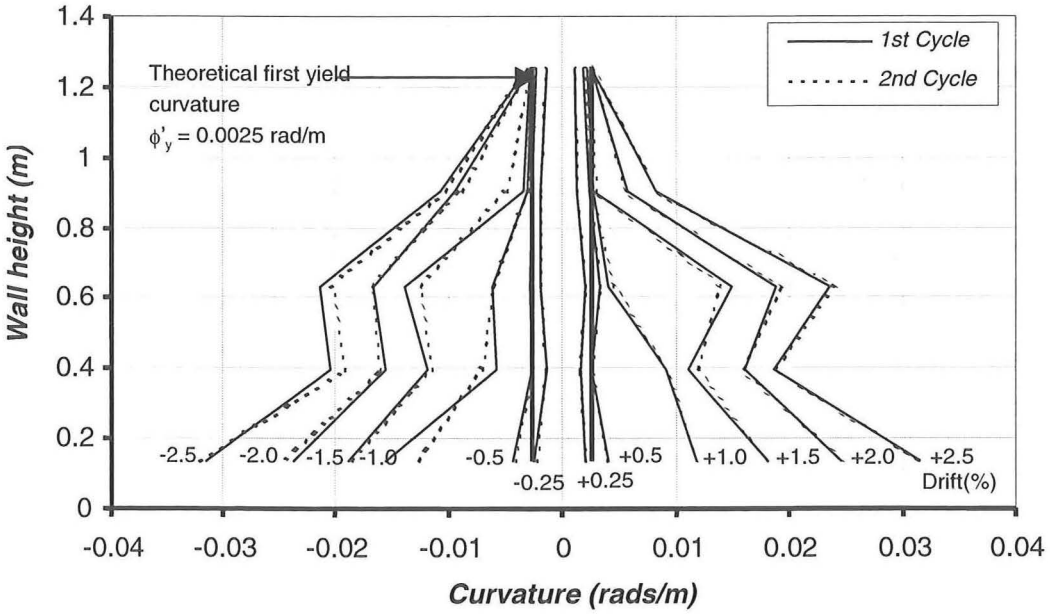

Figure 4.18 Curvature distribution in the wall panel of Unit 1.

The axial strain at the wall centreline in both the positive and negative directions of drift are illustrated in Figures 4.19 and 4.20. As suggested from the curvature distribution plot shown in Figure 4.18, axial strain diminishes from a maximum at the base of the wall to very low values near the top of the plastic hinge. Axial strain is also shown to increase with increased lateral drift. In the positive and negative directions the level of axial strain at the centreline was measured at 2.5% drift to be 2.0% and 2.3%, respectively. Wide cracks forming at approximately 0.6m from the base seem to boost the axial strains measured past 1.0% lateral drift. Little difference in the axial strain distribution was evident between the 1st and 2nd cycles to each level of drift. This suggests a rather symmetric distribution of cracks each half the wall. Negative cycles of drift seemed to provide slightly greater values of axial strain than those of the corresponding positive cycles. An explanation for this could be explained through the positive cycles being conducted prior to the negative load cycles. Some of the cracks that formed or opened during the previous positive cycle may not have fully closed upon unloading resulting in a contribution to the strain measured in the negative cycle. Integration of the axial strains gives the axial elongation of the wall. Since most of the axial strain is developed in the instrumented region the total wall elongation should be only slightly greater than that calculated for the axial strain distribution shown in Figures 4.19 and 4.20. At the peak of +1%, +1.5%, and +2% drift, the axial elongation of the wall was calculated to be 3.5mm, 6.4mm and 9.1mm, respectively. Slightly larger values of 4.0mm, 6.7mm, and 9.2mm were recorded in the negative cycles to the same levels of drift.

From both the curvature and axial strain plots it is possible to extrapolate in order to obtain the concrete extreme fibre strains at the corners of the wall. At the initial signs of spalling (±2.0% drift) the compressive concrete strain was determined as being 0.01% at the base of the wall. At crushing (2.5% drift) extrapolation of the data produced compressive concrete strains at the extreme fibre in compression of 0.10%. Both these values are very low when one considers typical values in the order of 0.7% and 1.5% at the initial stages of spalling and the ultimate crushing of the concrete. This suggests therefore that the longitudinal bars at the corners of the unit were carrying a significant portion of the compression force and that compression was carried through the concrete through dislocated particles. Rather than the concrete spalling due to

excessive compression, spalling might have occurred due to bar buckling of the longitudinal reinforcement.

Crack widths at locations stated in section 4.2.1 were recorded at both peak and residual points of each cycle, see Table 4.1. Up to 0.5% drift, crack widths remained beneath 0.2mm and all but closed upon unloading. Past 0.5% drift crack widths surpassed 1mm with some remaining open up to 90-100% of there original width upon unloading. This indicates the beginnings of residual drift at quite low levels of lateral displacement, well before significant damage to the wall unit itself. By ±2% drift residual widths of essentially all the cracks measured remained open to almost their peak values, many of these cracks being in excess of 2-3mm wide.

The general performance of Unit 1 was typical of a conventional reinforced cast-in-place structural wall. The recess connection between the wall and foundation beam performed particularly well. Virtually no pullout was observed during the test, providing the idealised fixed connection assumed in design. Strain gauges placed on threaded bars placed horizontally through the beam and wall show a cyclic response matching the loading schedule. These bars, as per design, remained below yield.

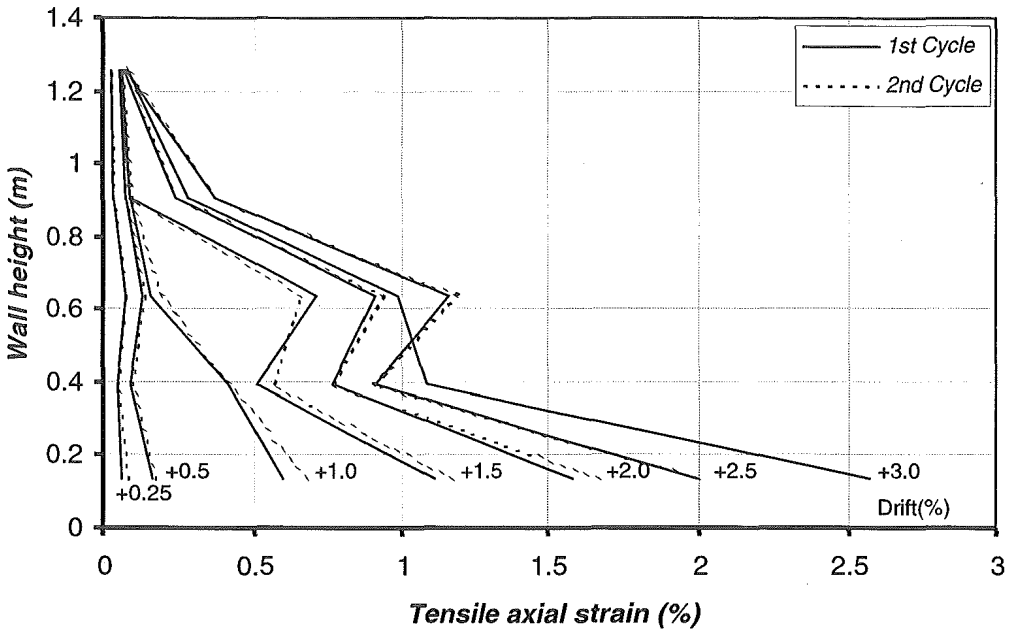

Figure 4.19 Unit 1 Centreline tensile axial strain – positive drift.

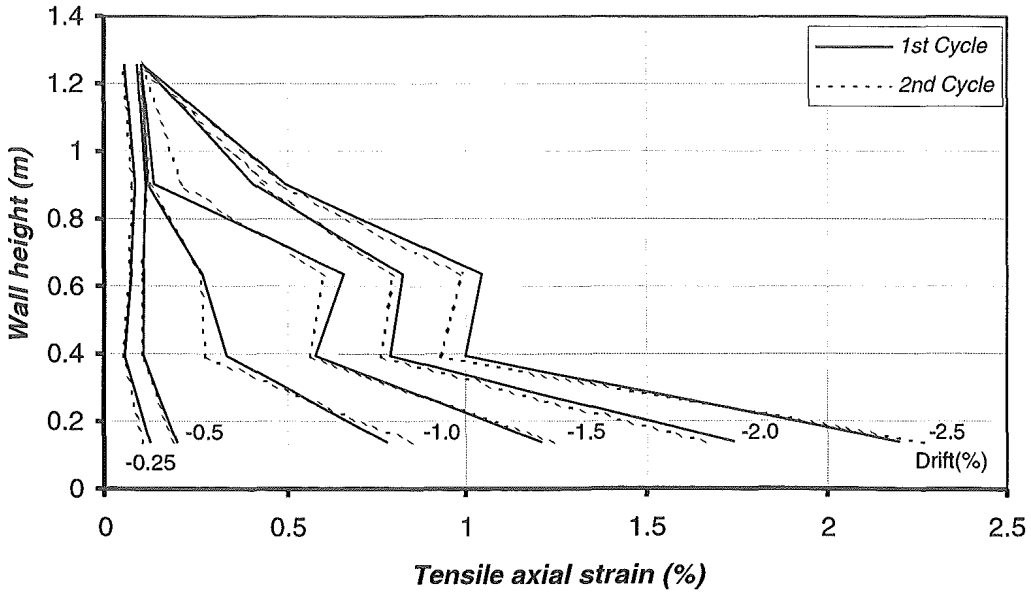

Figure 4.20 Unit 1 Centerline tensile axial strain – negative drift.

Table 4.1 Crack widths at peak and residual drifts.

Positive drift cycle cracking

	Location:				
	1	2	3	4	7
+0.25% L	0.1	0.1	0.1	0.1	0
+0.25% U	0	0	0.05	0	0
+0.5% L	0.2	0.15	0.2	1	0
+0.5% U	0	0	0.05	0.2	0
+1.0% L	0.8	1	1	1.6	0
+1.0% U	0.6	1	0.8	1.4	0
+1.5% L	1.8	2	1.5	2.5	0.2
+1.5% U	1	2	1.5	1.6	0.2
+2.0% L	2	2.5	2	3	0.5
+2.0% U	1.8	2.5	2	2.5	0.4
+2.5% L	2	2.6	3	4	0.5
+2.5% U	1.8	2.5	2.5	2.6	-

Negative drift cycle cracking

	Location:			
	3	5	6	7
-0.25% L	0.08	0.08	0.1	0.1
-0.25% U	0.05	0	0	0.05
-0.5% L	0.1	1	0.15	0.2
-0.5% U	0.05	0.2	0	0.05
-1.0% L	1	1.8	1.5	2.2
-1.0% U	0.8	1.2	1.2	2
-1.5% L	0.8	2.5	2	3
-1.5% U	0.8	1.6	1.2	2.5
-2.0% L	1.5	2.5	2	3.5
-2.0% U	1.5	1.8	1.8	3
-2.5% L	2	2.5	2.5	4
-2.5% U	2	2.5	2	4

Key

L = At peak loading of 1st cycle to given drift level.

U = At unloaded state of 1st cycle to given drift level.

Notes: (1) All crack widths stated are in units of mm.
(2) See Figure 4.1 for location of crack points.

4.3 RESULTS FOR UNIT 2

4.3.1 Behaviour and Observations of Unit 2

From the initial semi-cycle to +0.25% the wall rocked, opening up a gap of 3mm at the easternmost corner that extended approximately midway through the joint. Very careful examination of the wall uncovered no visible cracking of the specimen. Identical observations were made at the reverse semi-cycle, as well as the subsequent cycles to +0.25x2, and –0.25x2.

Semi-cycles to ±0.5% lateral drift again produced no visible cracking of the wall. The gap at the bottom of the unit opened to approximately 5mm at the corners and extended two thirds the way through the wall, see Figure 4.21. The foundation beam first showed initial signs of flexural cracking at the semi-cycle to ±0.5x1. These cracks did not extend considerably nor did they open appreciably after this attained level of drift. Over subsequent semi-cycles to ±0.5x2 and ±0.25x3 no visible change in the behaviour of the unit was observed.

At semi-cycles ±1.0x1 Unit 2 remained visibly undamaged. Rocking had opened the gap at the base of the wall to roughly 10mm extending to within 200mm of the pivoting corner, see Figure 4.22. The semi-cycle to +1.0x2 was the first cycle reached that produced visible cracking in the wall panel. A vertical hairline crack was visible on the north-face of the wall only, extending approximately 150mm from the base, initiating 400mm from the Western corner. This crack did not extend over the remainder of the test nor was it visible upon the removable of the lateral load. The cause of this crack is thought to be the result of tension through bottom cord of the unit, see Figure 2.22. At this stage of the test the wall was brought to rest at zero lateral load, this produced negligible residual drift.

Subsequent drifts from 1.5% to 2.5% showed no further signs of cracking in the wall panel or foundation beam, see Figure 4.23. The gap at the wall base opened very close to that predicted from purely rigid body rotation, suggesting the wall panel was rocking about the lowermost corners.

At semi-cycle +3.0x1, the drift limit of the original test history, a small split crack was observed in the south-western corner of the unit, see Figure 4.24. This crack was approximately 40mm in length and 0.5mm wide. Excess mortar also began to flake off the base plate in this same corner, though this can not be attributed to damage of the unit apart from the removal of paint. It was noted that the western corner of the unit had sustained no damage at this level of drift. At peak loading the gap at the bottom of the wall had opened 50mm, the neutral axis depth reducing to approximately 100mm, see Figure 4.25.

Residual drift as was the case throughout the entire test was found to be negligible upon loading, see Figure 4.26. The observed crack pattern in the foundation beam, see Figure 4.27, was similar to that which was expected from the strut-and-tie model developed, see Figures 2.39 and 2.40.

In order to find the ultimate capacity of Unit 2, the failure mechanism had to be determined. In order to achieve this it was decided that the unit be laterally displaced in the positive direction until either failure of an energy dissipator bar or carbon fibre post-tensioning tendon occurred. To ensure testing equipment and instrumentation were operating correctly a complete cycle at 2.5% drift was completed. Unit 2 was then laterally displaced to an effective +5% interstorey drift. At this drift a minor amount of concrete crushing was observed to occur at the western corner of the wall. This extended approximately 40mm up the wall and 5-10mm into it, see Figure 4.28. A 100mm long crack, less than 0.5mm wide, on the northern face was observed to extend from western corner, orientated at an angle similar to that of diagonal reinforcement. This crack closed and was no longer visible once the lateral force had been removed. The unit was subsequently loaded to its equivalent -5% lateral drift. At this semi-cycle no damage was observed at the eastern corner upon which the unit rocked. It was during this semi-cycle however that an apparent push-out failure of the dissipator bars was first noticed. Spalling of the concrete within the foundation beam recesses was observed with a large crack running the full height of each recess between both post-tensioning ducts, see Figure 4.29.

Unit 2 was displaced in the positive direction until failure occurred at an approximate drift of 6.2%, see Figure 4.30. Failure was initiated with the eastern dissipator bar fracturing. The unit was displaced a small amount past this limit, moments later resulting in a loud failure of all three eastern-duct carbon fibre tendons. Spalling of the corner concrete was perceived to not have progressed much further past that observed at 5.0% drift, see Figure 4.31. Apart from the eastern dissipator bar and carbon rod at failure, Unit 2 remained virtually undamaged after cycles in excess of 6.0% drift.

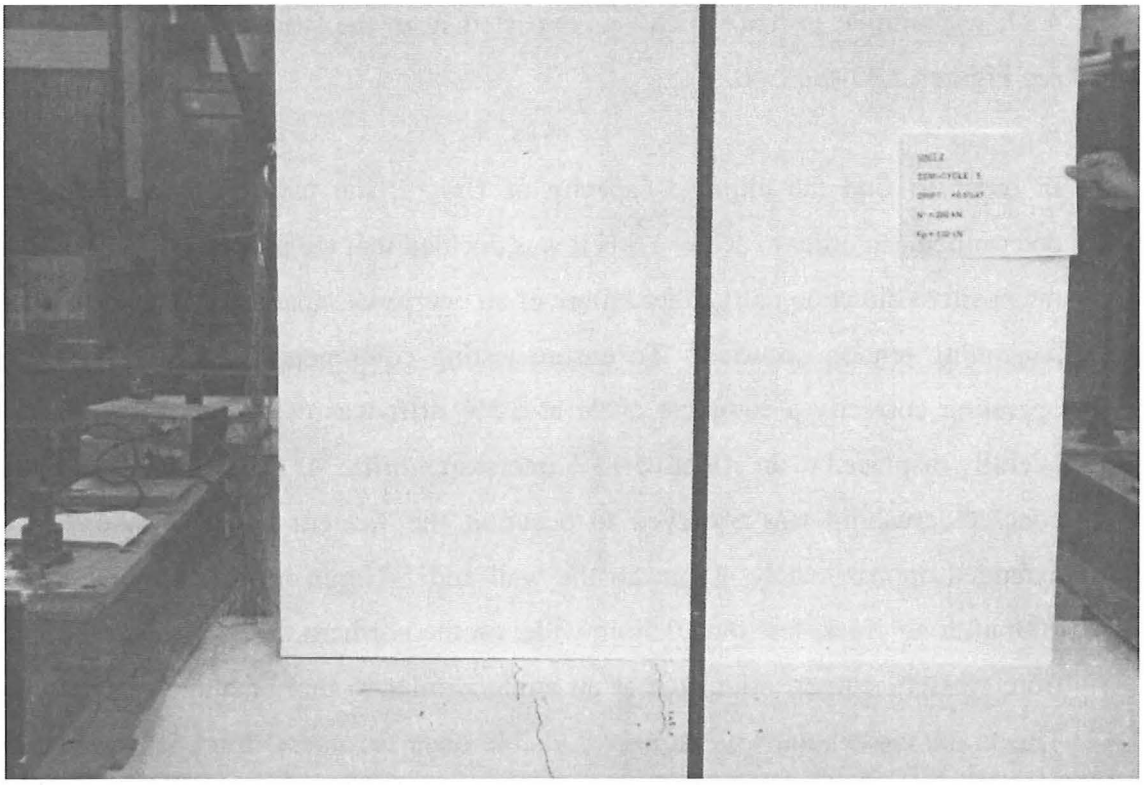

Figure 4.21 North face of Unit 2 at +0.5x1.

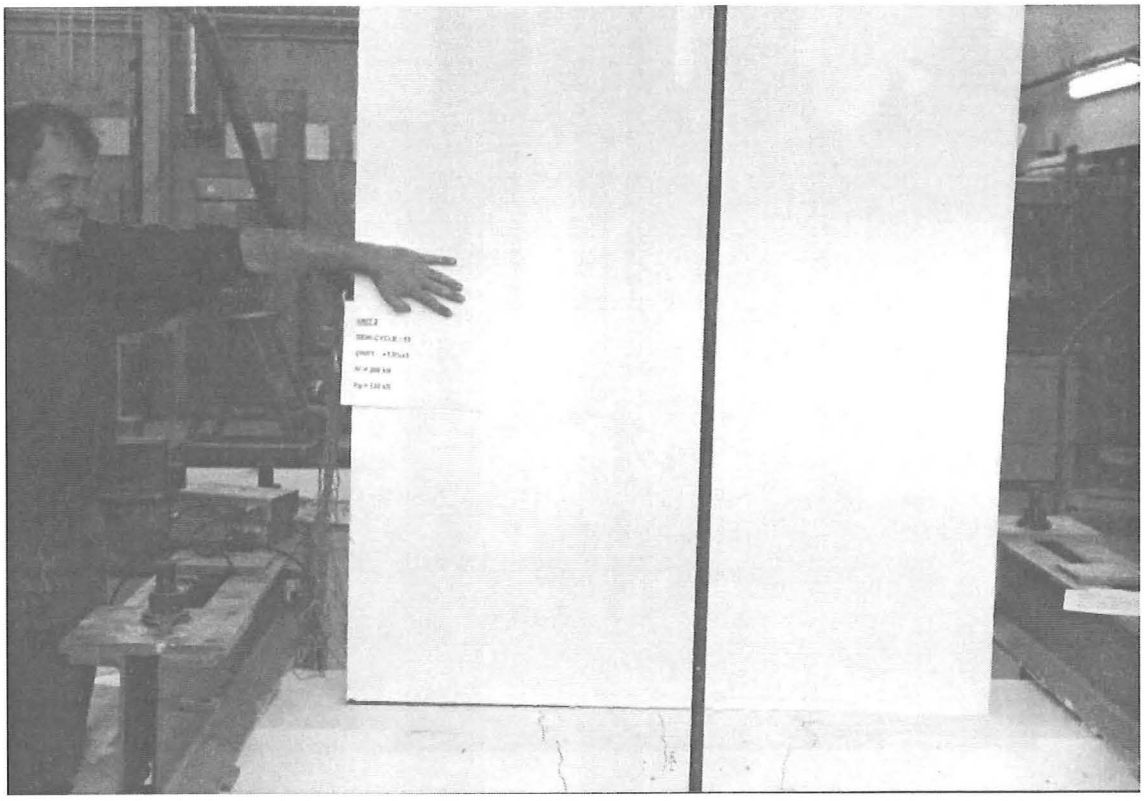

Figure 4.22 North face of Unit 2 at +1.0x1.

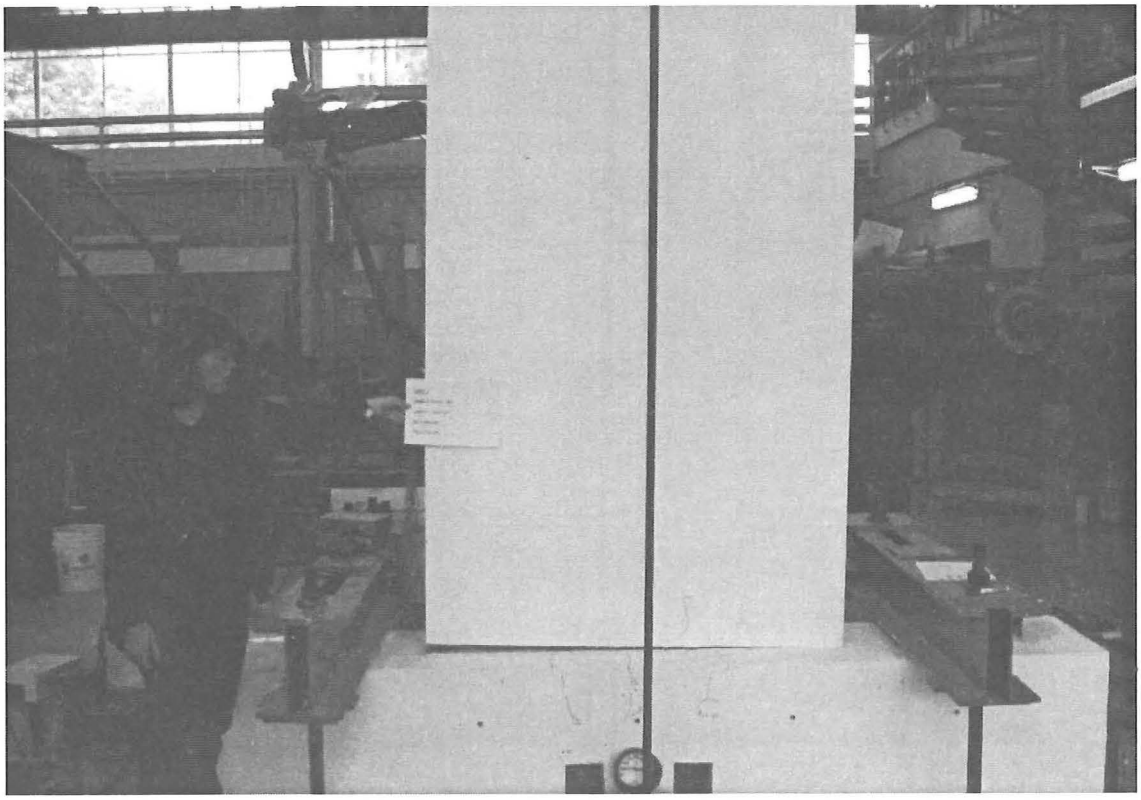

Figure 4.23 North face of Unit 2 at +2.5x1.

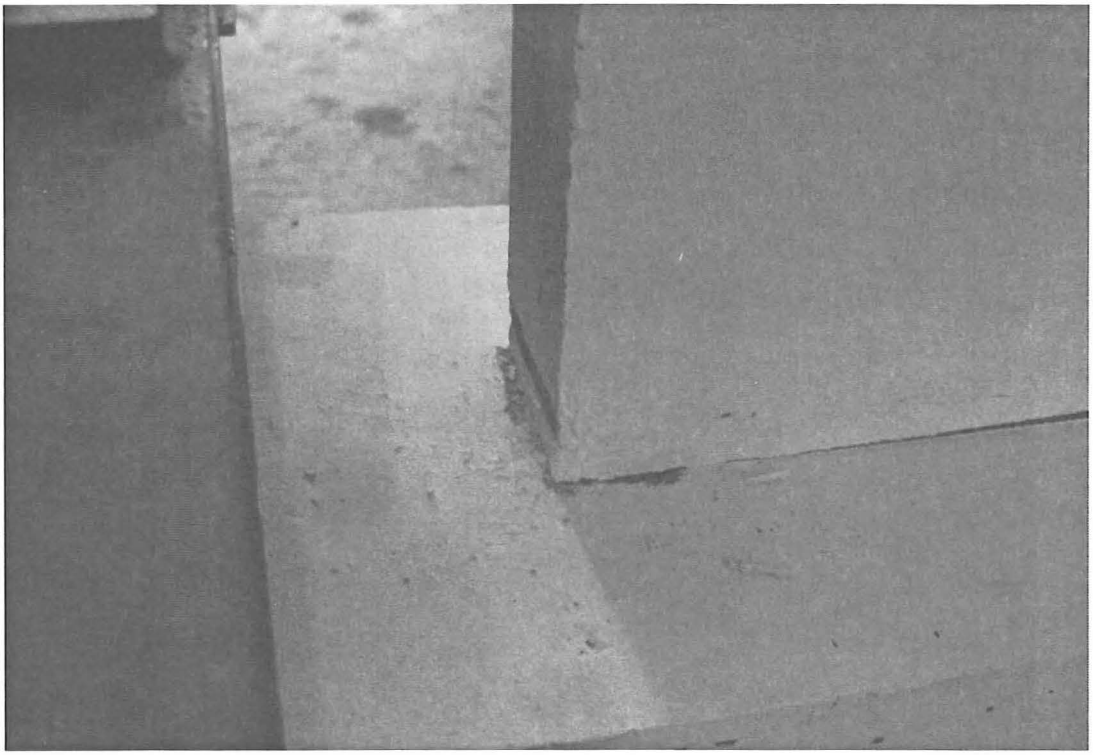

Figure 4.24 Small split crack at the south-western corner of the wall panel of Unit 2 +3.0x1.

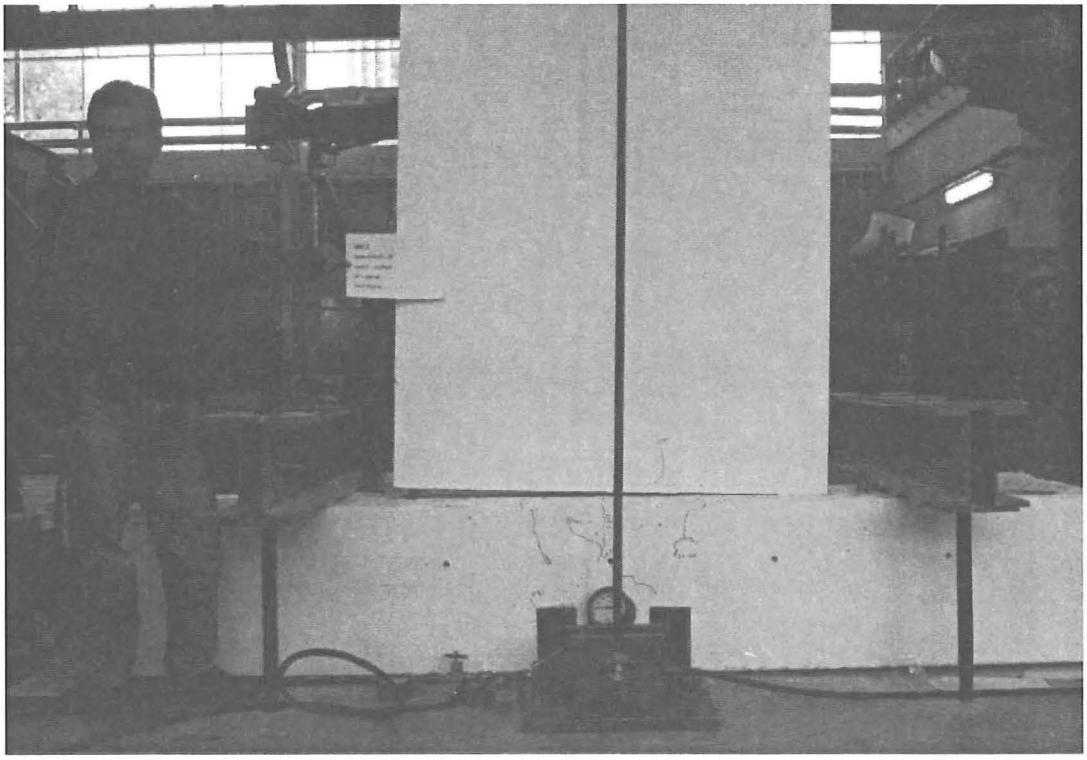

Figure 4.25 North face of Unit 2 at +3.0x1.

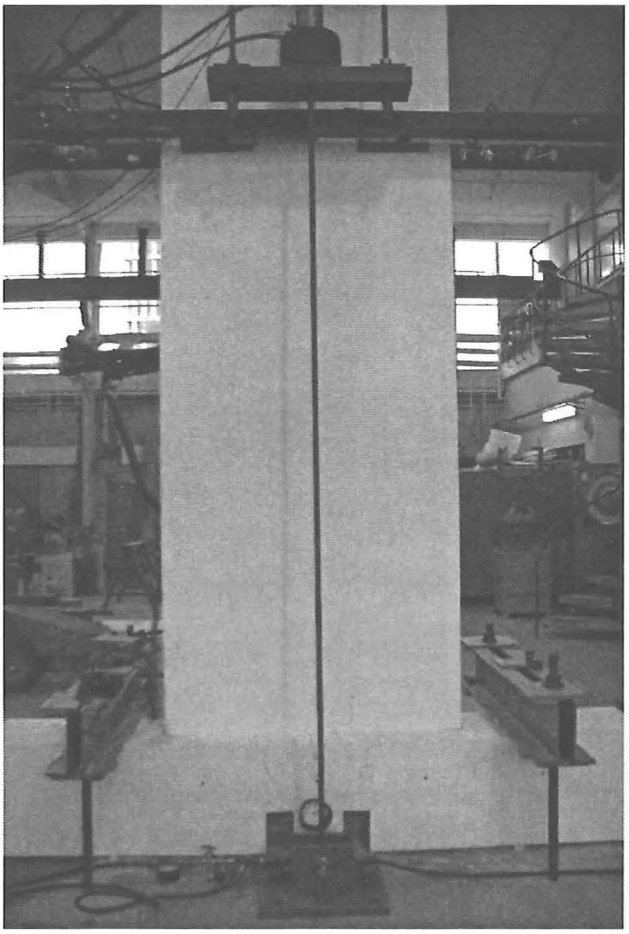

Figure 4.26 Residual drift of Unit 2 after +3.0x1.

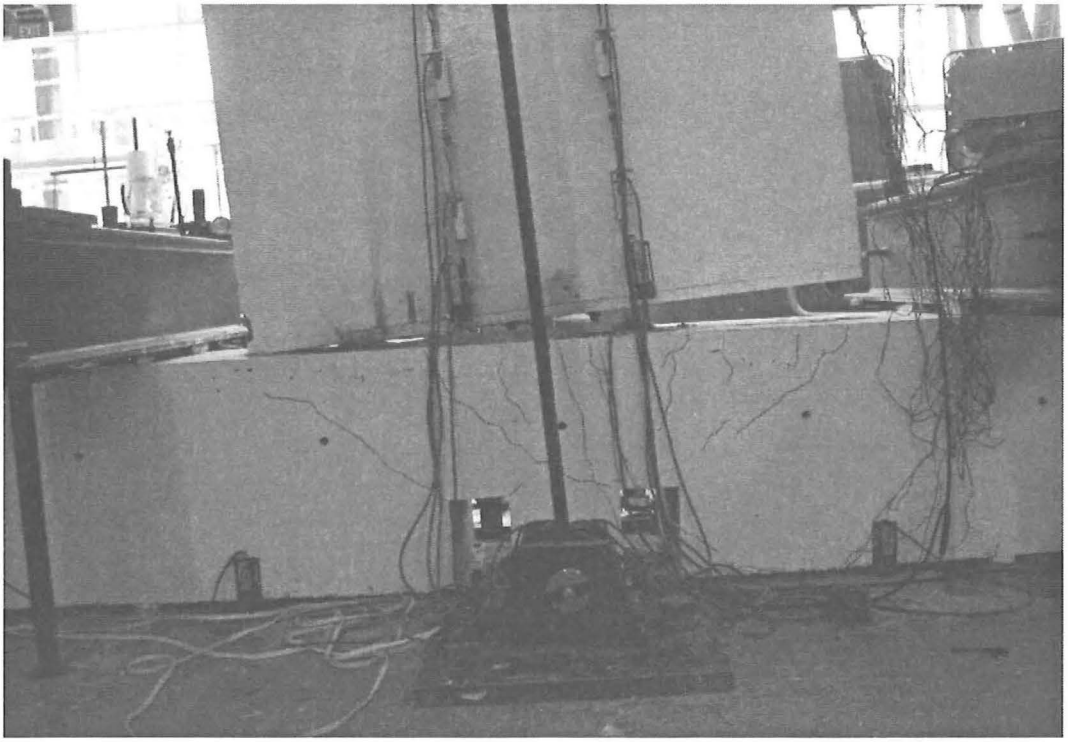

Figure 4.27 Unit 2 foundation beam crack pattern at +5.0x1.

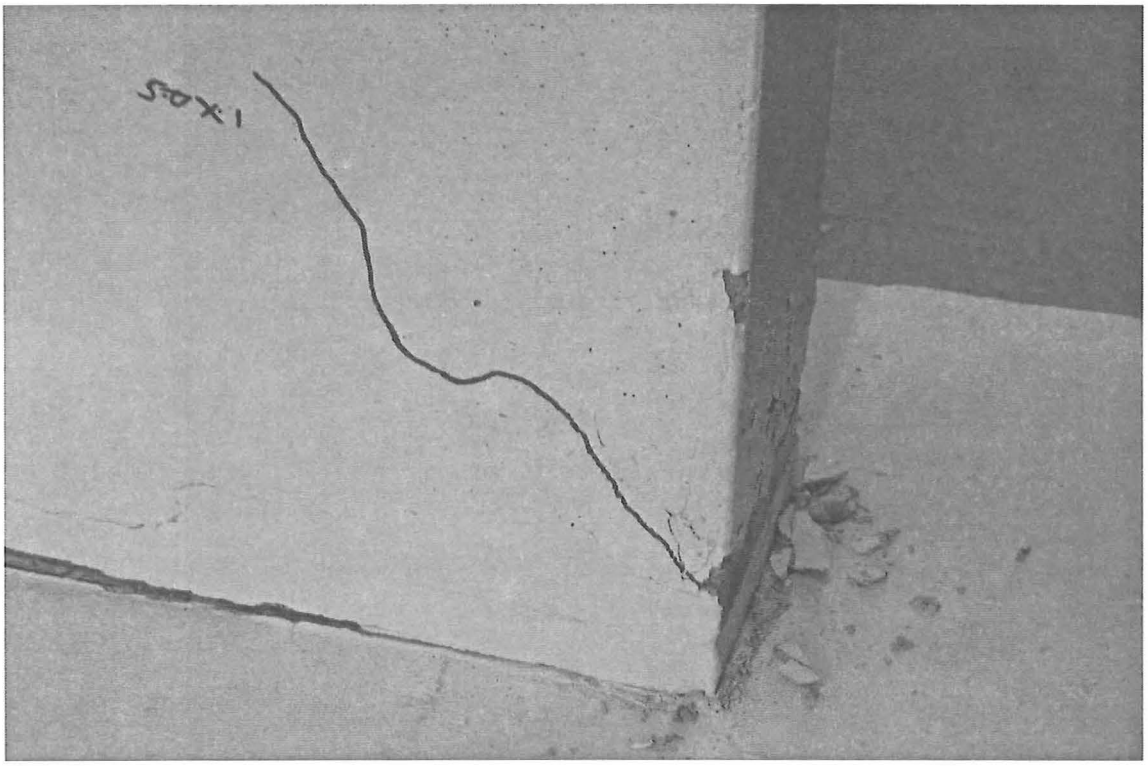

Figure 4.28 Incipient concrete spalling in the north-western corner of Unit 2 at +5.0x1.

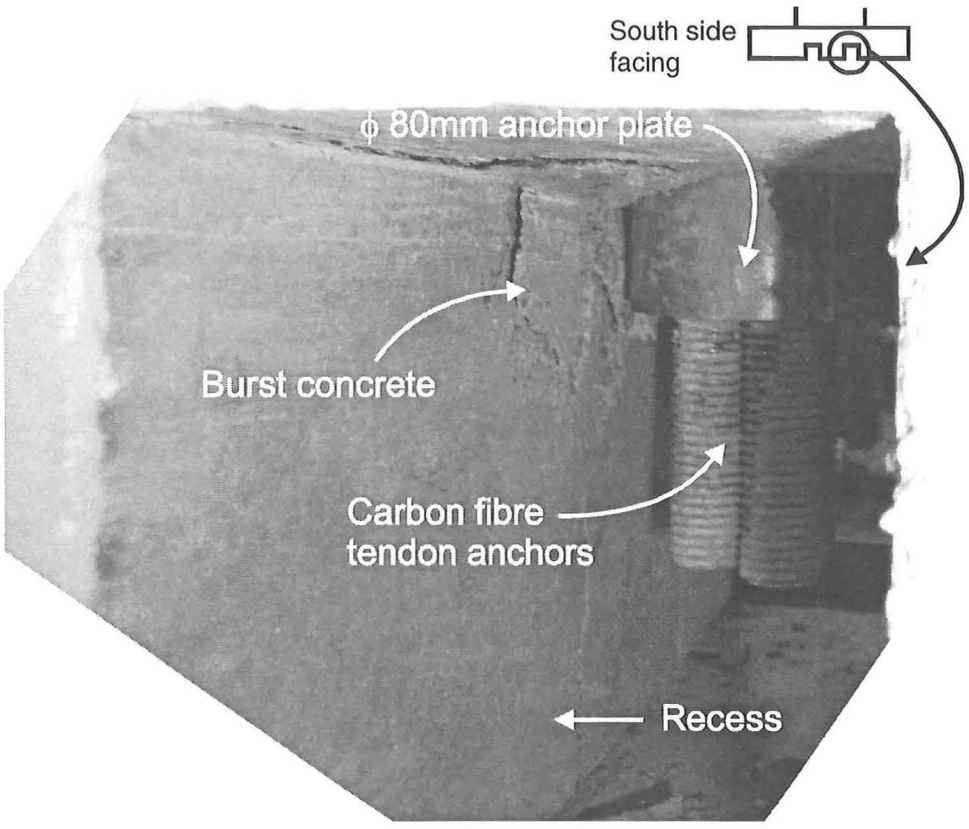

Figure 4.29 Energy dissipator push-out failure at -5.0x1.

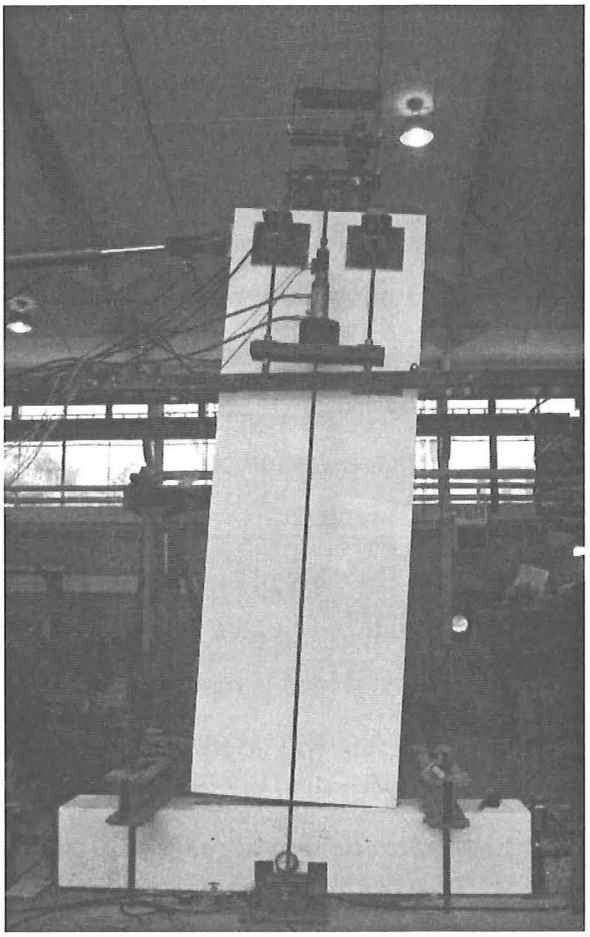

Figure 4.30 View of Unit 2 at +6.2x1.

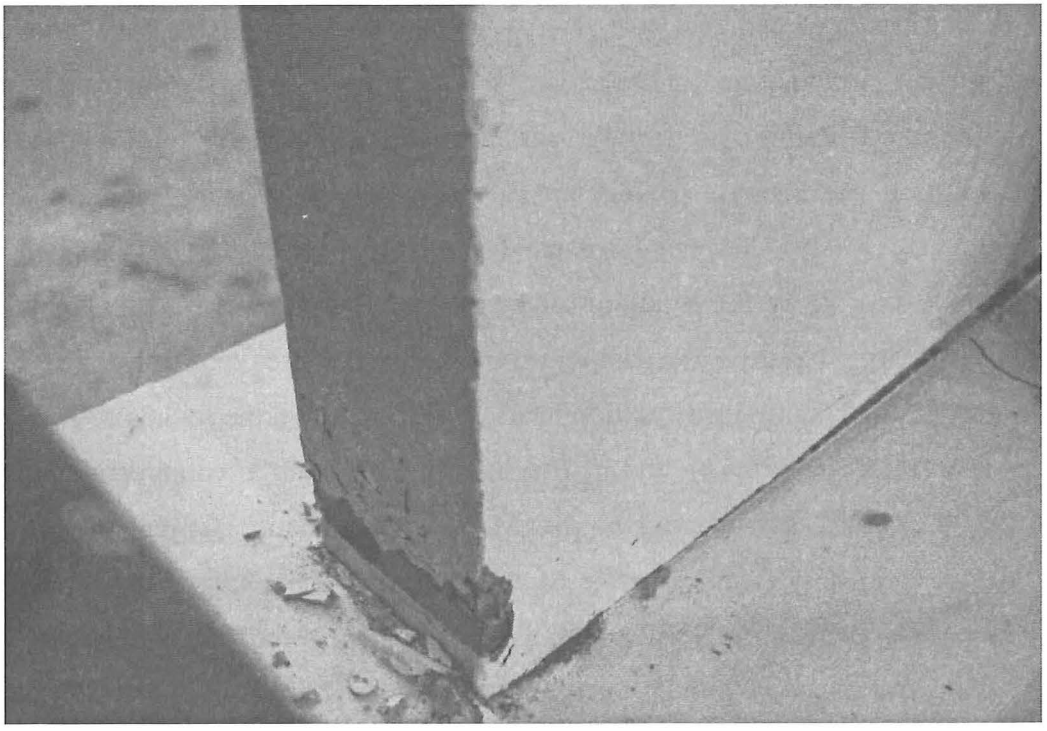

Figure 4.31 Extent of concrete spalling in the south-western corner of Unit 2 at the end of the test.

4.3.2 Analysis of Experimental Results for Unit 2

Figure 4.32 shows the lateral force–lateral displacement response of Unit 2. Also shown in this figure is the theoretical backbone response obtained using the approach discussed in section 2.3.3, and using a/2= 88.0mm in Equations 2.25, 2.26, 2.27, 2.29, 2.30, and 2.32. Figure 4.33 shows the response of Unit 2 up until 1.0% drift. The backbone response of Unit 2 was very close to that predicted theoretically, in both the positive and negative directions of loading. The theoretical response also closely matched the point at which rocking commenced. This suggests that the performance of such structures can be closely predicted.

The shape of the loops also indicates a lack of energy dissipation during the unloading part of the cycle, where the lateral load is removed and the gap formed at the base of the wall closes. No damping due to compression of the energy dissipators seemed apparent in the response. The same observations can be made from both the negative and positive drift semi-cycles. Observation of the loops obtained by Rahman and Restrepo (2000) illustrates the expected hysteretic development, with energy dissipation occurring throughout the entire cycle, see Figure 4.34. The main cause for the lack of compressive force in the energy dissipators was due to the use of 18mm thick plywood pugs which dammed the steel ducting within the foundation beam, into which the dissipators were grouted. Given that the bearing plate of the dissipator bar was placed at the very bottom of the ducting, see Figure 2.37, compaction of this pug would have acted as if like a spring preventing the energy dissipation bars from yielding back in compression. Another cause for the lack of compression energy dissipation can be attributed to the push-out failure of the energy dissipation bars. Illustrated in Figure 4.29 a bearing failure of the post-tensioning anchors caused crushing and spalling of the concrete. This caused a disruption to the load path within the foundation beam (refer to Appendix A (b), struts eg and ij) causing the dissipators in compression to slip rather than fully yield back in compression. Much to the potential damping to the system was therefore lost. It is noteworthy to mention that the energy dissipator bars were adequately anchored in tension and, as a result, they contributed to the capacity of the system and provided limited energy dissipation. Despite of the above failings Figure 4.32 indicates no strength degradation of Unit 2 past 3% drift.

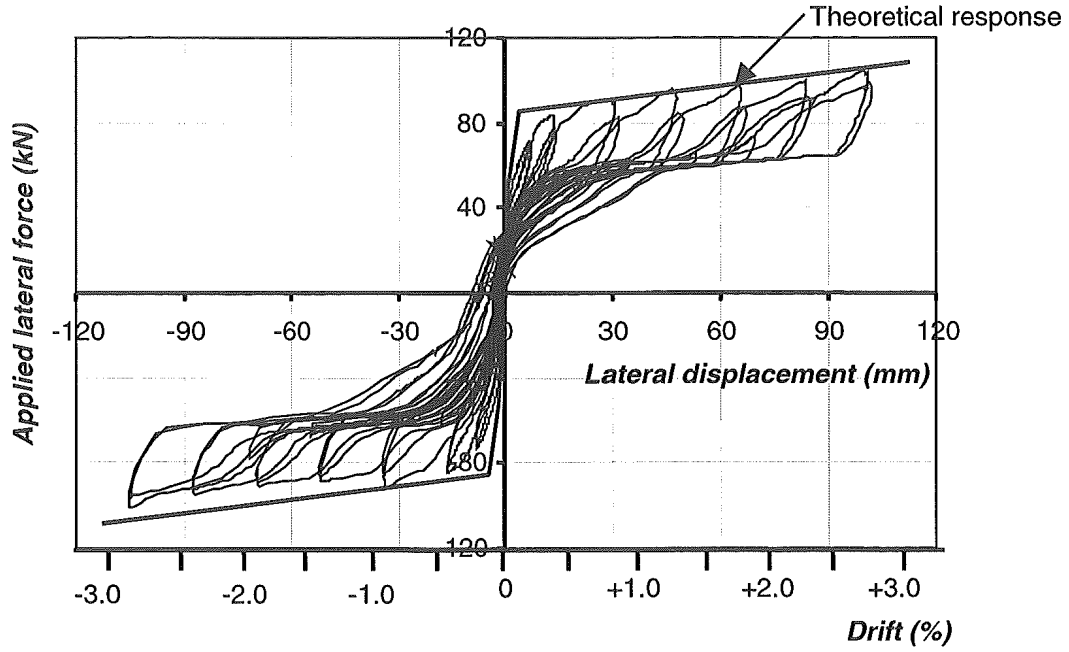

Figure 4.32 Full hysteretic response of Unit 2 up to 3.0% drift.

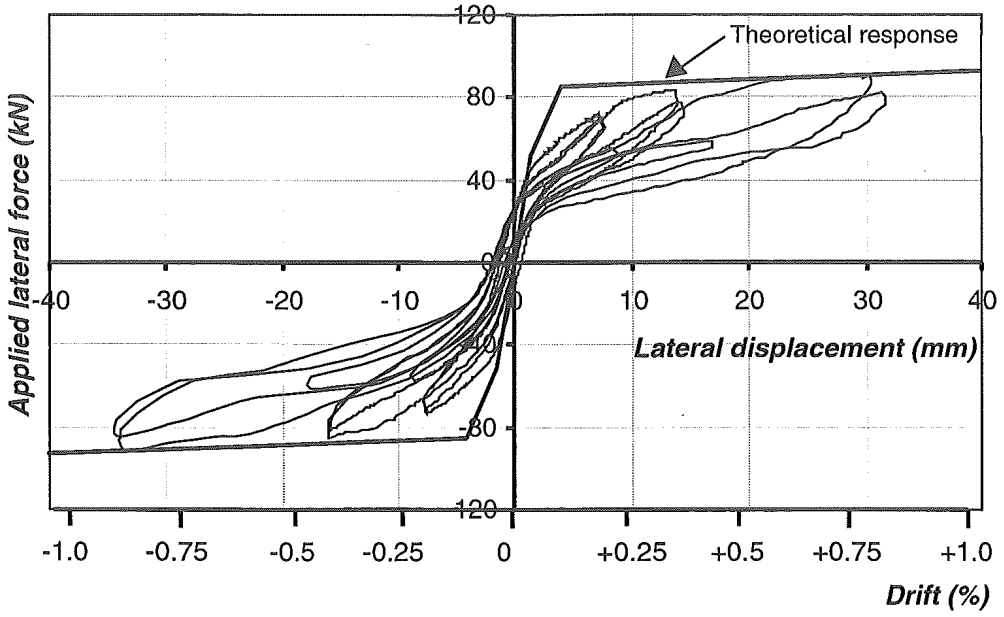

Figure 4.33 Hysteretic response of Unit 2 up to 1.0% drift.

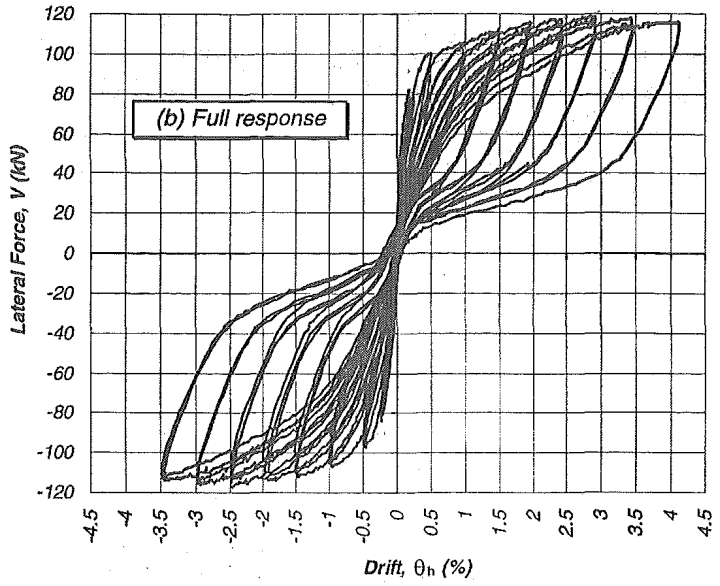

Figure 4.34 Lateral force-drift response of Unit 3. (Rahman and Restrepo, 2000)

Little data was attained from strain gauges placed on the energy dissipator bars due to a simultaneous failure of these gauges at approximately 0.5% drift. Readings were obtained up until yield for the eastern dissipator, however no useful data could be garnished from the strain gauges placed on the western bar. Figure 4.35 plots the axial force-strain relationship for the eastern dissipator up until yield. The axial force was derived from strain gauge readings, using the calibration factor obtained for the dissipator. Average tensile strain was obtained from the axial displacements at the level of the dissipators using the readings of linear potentiometers P7 and P8 referred to in Figure 3.6. The axial displacement was divided by the milled length of the dissipator to obtain average strains. Figure 4.36, obtained from Rahman and Restrepo (2000), shows the expected axial force-strain relationship of an energy dissipation bar similar to those designed for Unit 2. Figure 4.36 indicates how the maximum tensile and compressive stresses should be of similar magnitude. The behaviour of the eastern dissipator for Unit 2, over the small data range captured, is similar to observered by Rahman and Restrepo, (2000).

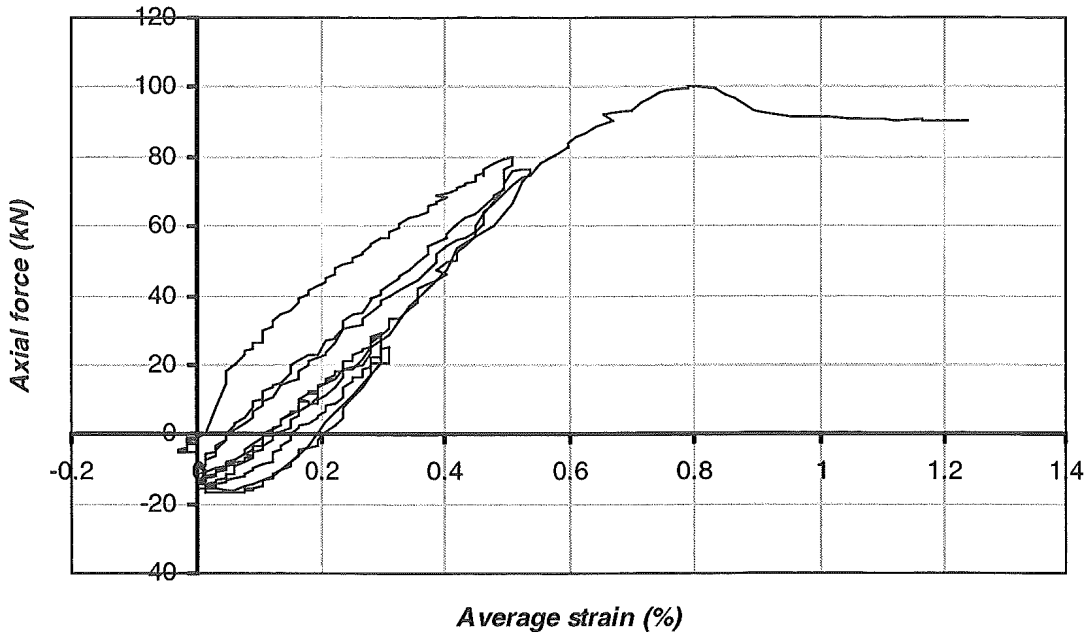

Figure 4.35 Unit 2 Axial force-strain relationship for eastern dissipator.

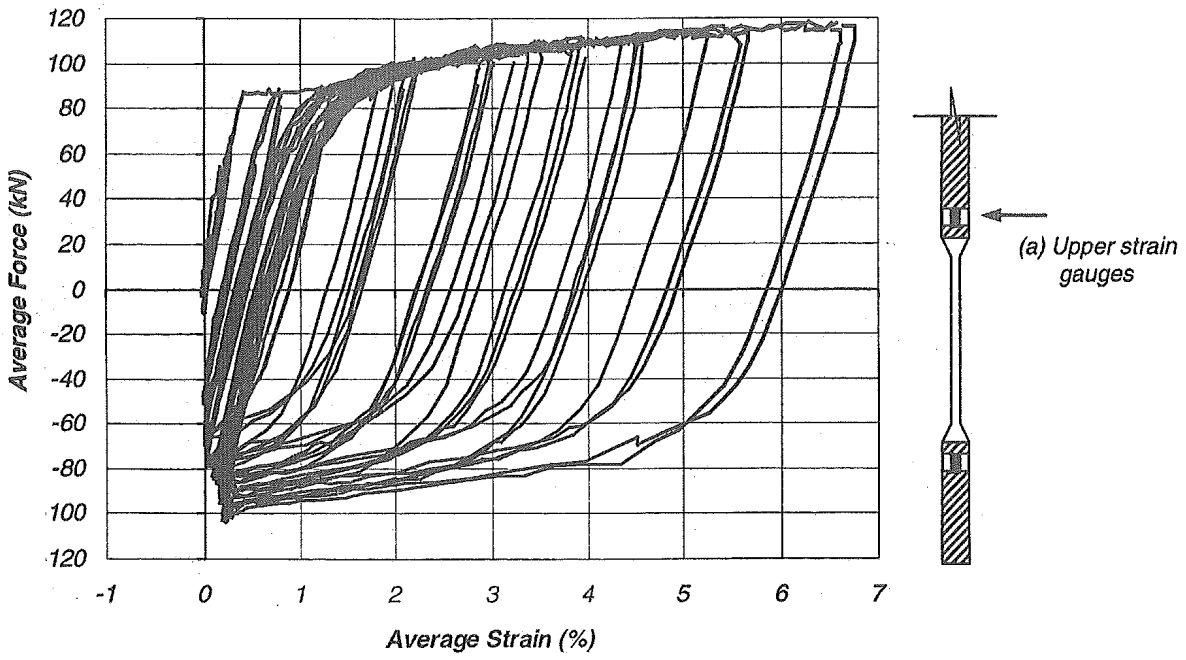

Figure 4.36 Axial force-strain characteristics of the east energy dissipator in Unit 3 tested by Rahman and Restrepo (2000).

The hysteretic response up until failure is illustrated in Figure 4.37. The sudden drop off in load at approximately 6.2% drift indicates the simultaneous failure of the eastern dissipator bar and carbon fibre tendons. The shape of the hysteretic loops, specifically those cycles at 5.0% drift, again indicated a lack of energy dissipation through compression of the tapered dissipator bars. Despite this the capacity of the energy dissipating bars exceeded their design demand of 2% drift. Failure to develop compression may have helped in this respect. The excessive drift that they did attain however indicated that the failure mechanism, highlighted by Rahman and Restrepo (2000) of fracture due to localised stresses seemed to be averted through adequate chamfering of the transitions between the tapered and non-tapered sections.

The equivalent viscous damping of the hybrid system was as expected somewhat lower than that achieved by Unit 1, see Figure 4.38. This was further exasperated by the unexpected push-out failure of the tapered energy dissipator bars. An approximate average of 5% equivalent viscous damping was achieved over the full testing schedule. As expected the 1st cycle at each level of drift produced higher levels of damping than the subsequent 2nd and 3rd cycles. This drop off in energy dissipation is more pronounced between the 1st and 2nd cycles than the 2nd and 3rd cycles due to the greater energy required to plastically deform the tapered energy dissipating bars past their previous maximum strain. The reduced equivalent viscous damping at higher drifts is evident of the push-out failure in the energy dissipators. The equivalent viscous damping for the initial cycles between 0.25%-3.0% drift, range from 8.5% to 3.8%. Over the same range 2nd cycles to these drift levels produced equivalent viscous damping ratios of between 5.9% and 2.2%.

Unit 2 performed as expected in regards to sustaining essentially no residual drift upon unloading, and in sustaining large drifts with no damage. As illustrated in Figure 4.39 practically no residual drift could be accounted for even after cycles in excess of 3.0% drift. Much of the residual drift can be attributed to the finite precision of the data records. Given that residual drift was found to be essentially negligible no meaningful conclusions can be made in regards to the effect of 1st, 2nd and 3rd cycles to particular levels of drift, other than to say that their effect is insignificant.

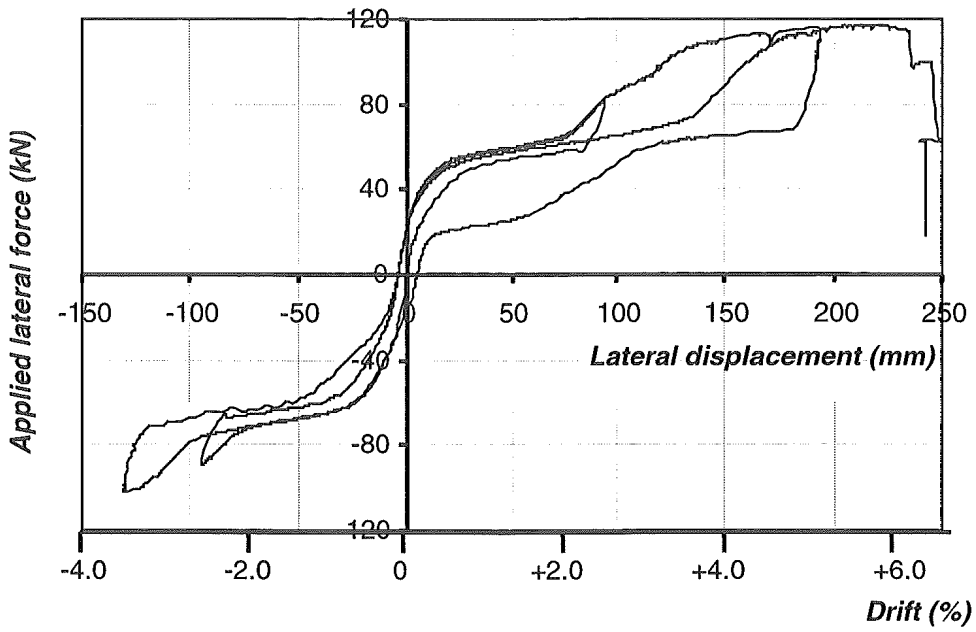

Figure 4.37 Hysteretic response of Unit 2 in final cycles of the test.

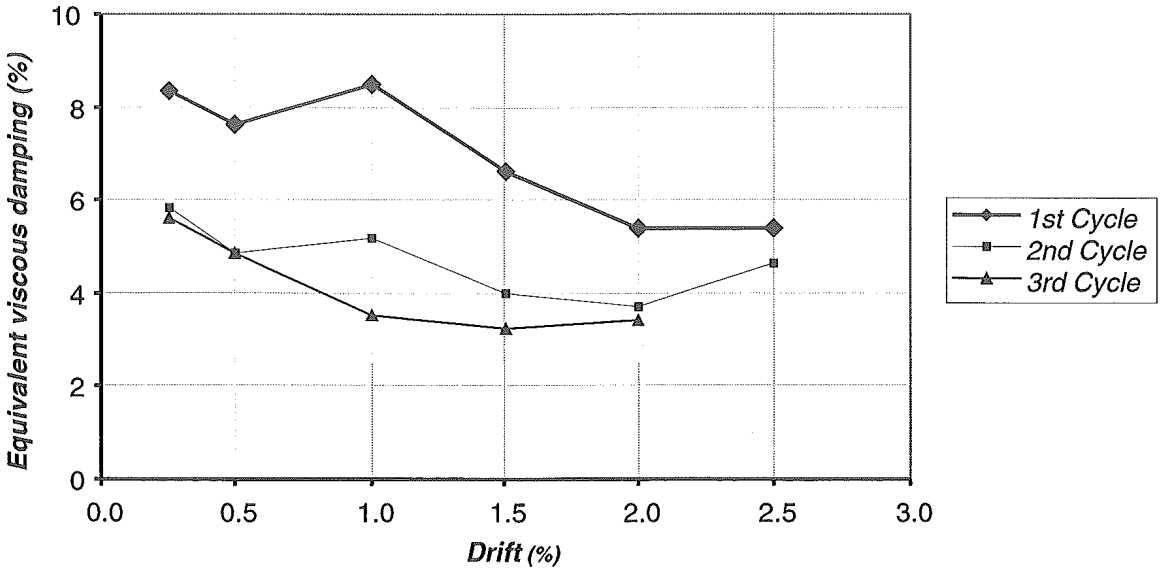

Figure 4.38 Equivalent Viscous Damping of Unit 2.

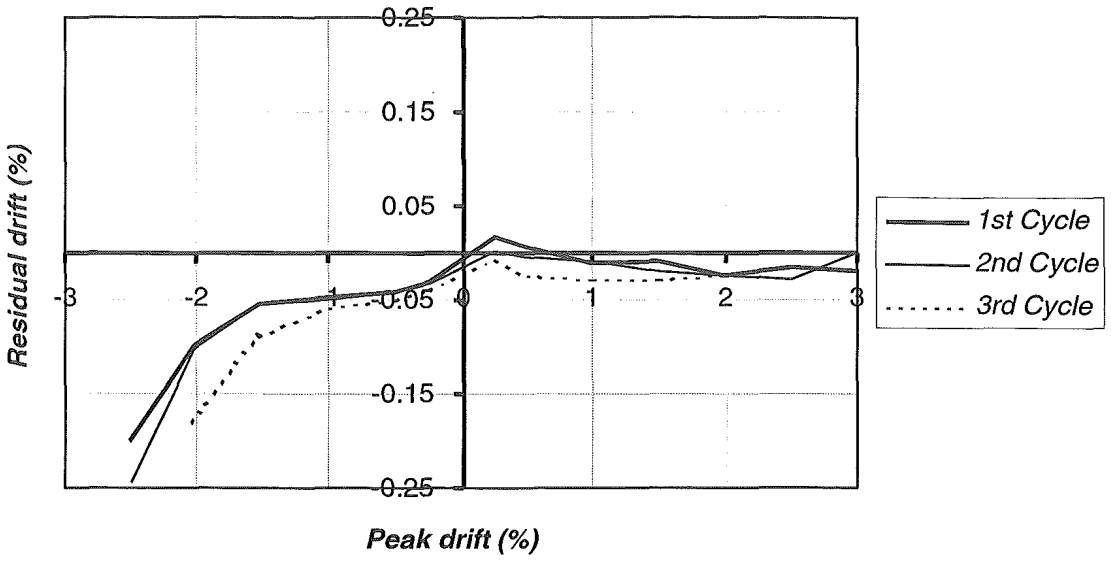

Figure 4.39 Unit 2 Peak versus Residual drift.

Figure 4.40 shows the decomposition of lateral displacements over each semi-cycle as a percentage of the total recorded lateral drift at the applied load. The lateral displacement exerted on Unit 2 showed that over 80-90% of the accountable lateral drift could be attributed to rocking of the wall panel. Another 15-20% was attributed to rotation of the foundation beam, with the remainder associated with foundation beam and wall sliding. This last component was found to be largely negligible. As with Unit 1, the decomposition of lateral displacements was achieved though readings gathered from linear potentiometers placed on both the wall and foundation beam. For each semi-cycle the total displacement that could be attributed through rocking, foundation beam rotation, and wall and base sliding ranged from approximately 80 to 100% of the total deflection recorded. As the applied lateral displacement is increased, the total displacement that can be accounted for approaches 100%. This is expected given the diminishing influence from elastic flexural and shear deformations in the wall panel, not accounted for, make up a greater proportion of the total displacement at low lateral drifts. As found with Unit 1, the contribution from beam rotation diminishes as the applied drift increases and rigid body rotation of the wall panel begins to dominate the response.

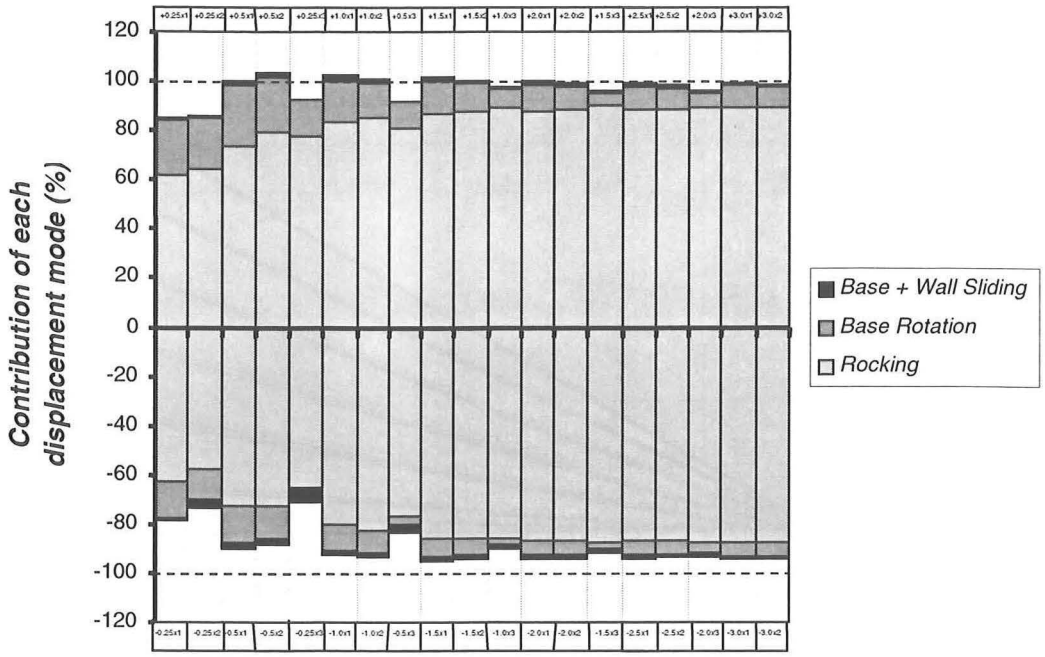

Figure 4.40 Decomposition of lateral displacements in Unit 2.

The base rotation at the 1st and 2nd semi-cycles up to 3.0% lateral drift are given in Figure 4.41 and Figure 4.42. The measured width of the gap at the base of the wall with respect to the aspect ratio shows that the majority of the applied deflection at the top is due to rigid body rotation of the wall. Virtually identical responses in both the positive and negative directions are shown, with essentially no change in the response between the 1st and 2nd semi-cycles at each level of drift. The compression block, about which the unit pivoted, is shown to decrease from approximately 350mm to 90mm in length as the level of drift is increased. Between 2-3% lateral drift the bearing length is approximately 90mm, very close to that assumed under ultimate conditions in section 2.3.3.

Figure 4.43 shows the neutral axis depth ratio to wall panel length versus drift. For both positive and negative semi-cycles the neutral axis depth is shown to decrease with increasing drift. A relatively constant ratio of 0.08 is obtained in both directions of load past 2.0% drift. This corresponds to a neutral axis depth of 110mm which is reasonably close to that assumed in design, a = 176 mm. This suggests that the compressive force carried by the inner longitudinal bars was slightly greater than that carried by the outer bars, see Figure 2.21.

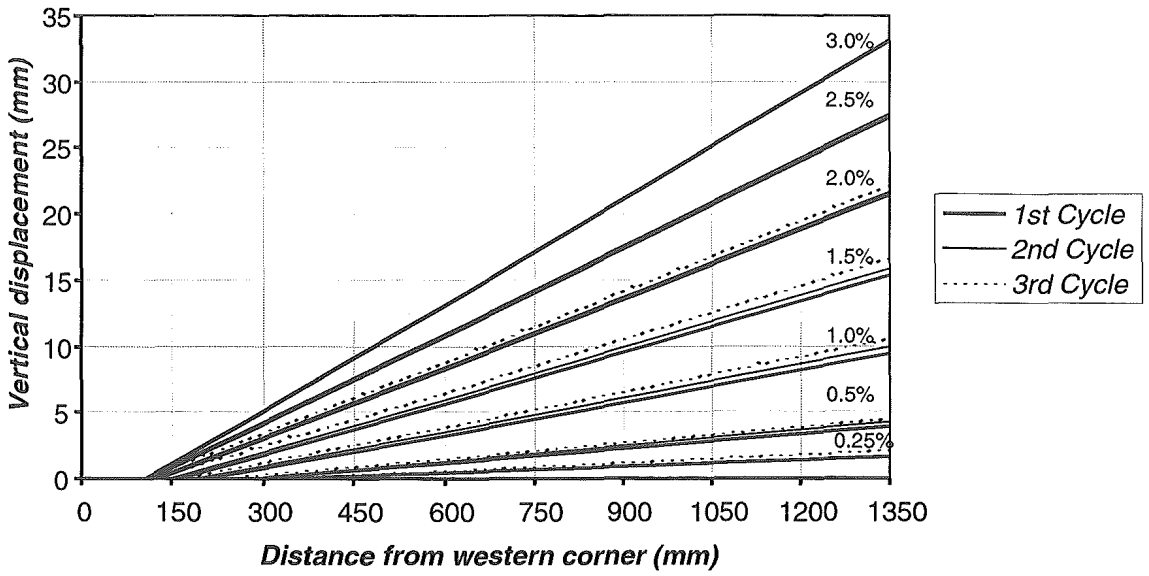

Figure 4.41 Wall base uplift – Positive cycles.

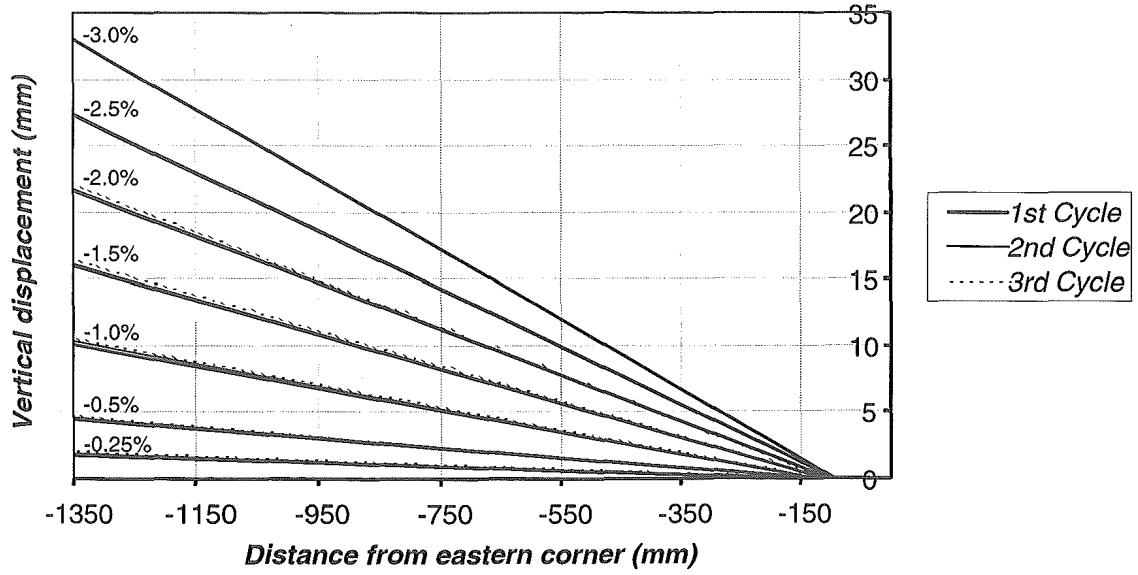

Figure 4.42 Wall base uplift – Negative cycles.

Strain gauges placed on the longitudinal and diagonal reinforcement of the wall panel showed no evidence of yielding within the unit. The average compressive strain recorded by strain gauges SG5 and SG6, see Figure 3.7, was 1500 με at 2.5x2. Strain gauges SG7 and SG8 recorded an average compressive strain of 800 με at the same drift level. Gauges mounted on the stirrups placed to help distribute the compressive forces within the panel recorded a maximum tensile strain of 50 με. This indicates that the alternative force flow shown in Figure 2.24 (b) was not activated. This was also evident due to the lack of cracking in the wall panel.

In general the performance of Unit 2 was very good as far as virtually no cosmetic damage to the wall panel occurred up until failure at a lateral drift in excess of 6% drift. The wall attained the design limit drift of 2% with no visual cracking of the concrete. It also demonstrated the self-centring characteristics expected upon unloading.

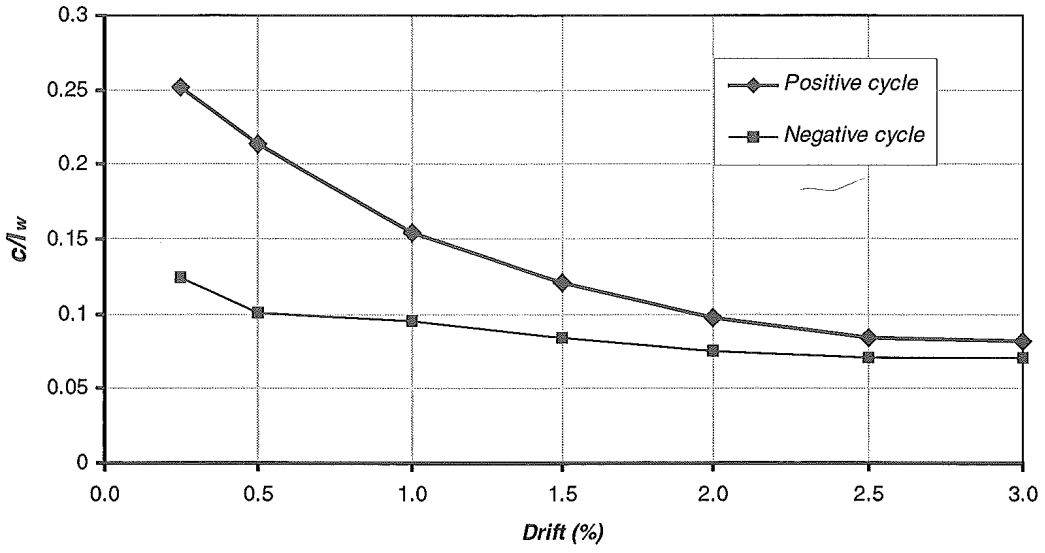

Figure 4.43 Neutral axis depth ratio to panel width versus drift.

5 DISCUSSION

Unit 1 performed as per design, its behaviour typical of a monolithic reinforced cast-in-place structural wall. Its capacity was very close to that predicted analytically. Capacity design principles ensured an inelastic mechanism formed involving the development of a flexural plastic hinge at the base of the wall. The recess connection between the wall and foundation beam performed particularly well. Virtually no pull-out of the wall panel was observed during the test, providing the idealised monolithic connection assumed in design. This unit attained a displacement ductility of $\mu_\Delta = 5.0$, and a drift of 2.5% when significant strength degradation occurred. As expected from the behaviour of the conventional monolithic construction large residual cracks, exceeding 2mm in width were observed after undergoing a peak drift of 1.0%. Residual drifts once the unit was pushed into the inelastic domain, which are also a characteristic of monolithic construction, where marginally smaller than at peak drifts.

The performance of Unit 2 was mixed in that it performed very well in regards to sustaining virtually no cosmetic damage to the wall panel, though not so well in that a push-out failure of the dissipator bars resulted a significant reduction in the level of energy dissipation achieved. The lateral load capacity was not significantly affected by this push-out failure, with the theoretical response closely matching that of the model structure. This is of particular importance given that current building codes would require a hybrid design approach to be reviewed as an alternative solution. It also provides the engineer confidence in that relatively simple hand calculations can predict the performance of the structure extremely well. The engineer can have better control over the design of the structure by incorporating both strength and stiffness requirements thereby obtaining the most economical solution. The unit attained the design limit drift of 2% with no visual cracking of the concrete. It also demonstrated the self-centring characteristics expected.

A comparison between Units 1 and 2 and Unit 3 tested by Rahman and Restrepo is made in the following paragraphs. Unit 3 was a hybrid unit, similar to Unit 2 tested in this research project. The wall panel in Unit 3 was conventionally reinforced, and post-tensioned with steel tendons. The energy dissipators in this unit were cast into the foundation beam and grouted into the wall panel. Specific reinforcement details are given in Section 1.4.3.

Damage to Unit 1 was extensive at even a moderate drift of 1%. Residual cracks up to 2mm wide extended throughout the unit concentrating especially within the plastic hinge zone. At a drift of 2.5% the damage was such that the capacity of the unit began to significantly degrade, see Figure 5.1 (a). In contrast Units 2 and 3 sustained very little damage up until the 3% design level drift.

Though Unit 3 sustained minimal damage to the wall panel under cyclic loading, Unit 2 was found to behave even better with virtually no cosmetic damage to the wall panel under lateral drifts exceeding 5%. Figures 5.1 (b) and (c) illustrate the relative damage to each unit at 3% lateral drift. The steel baseplate, cast at the bottom of the wall panel, and at the top of the foundation beam was particularly effective in preventing excessive compressive strains in the corner concrete, that otherwise would have caused crushing. Strut-and tie modelling proved to be an effective method of ensuring that the reinforcement carried the majority of the tensile and compressive forces developed under lateral displacement. The steel fibre reinforced concrete, used in order to control the development of cracks, allowed much of the conventional reinforcement cage utilised in Unit 3 to be omitted. The utilisation of steel fibre reinforced concrete, over that of conventional reinforcing, provides clear opportunities for savings in regards to both construction time and materials.

Apart from damage to the unit itself, residual drift after a seismic event is an additional problem associated with conventional monolithic construction. Units 2 and 3 both experienced virtually no residual drift at peak displacements well in excess 3% drift. This is because the hybrid walls are explicitly designed to self-centre after being subjected to large lateral displacements. The contrast between monolithic and hybrid construction is clearly shown in Figure 5.3. The lack of structural damage and lack of

residual drifts observed in jointed walls might easily overshadow the smaller inherited damping that can be obtained from the hybrid wall systems.

The drift capacity of Unit 2 was found to be greater than that achieved by Unit 3. The ultimate lateral drift prior to failure for Unit 2 and 3 being 4% and 6.2 %, respectively. The failure mechanism for both units was due to fracturing of the energy dissipators, stress concentrations sighted as the cause of failure in Unit 3. This therefore suggests that chamfering of the tapered transition as stated per design was effective.

The equivalent viscous damping of Unit 1 was, as expected, greater than that obtained for both hybrid units, see Figure 5.2. A direct comparison with Unit 3 shows that Unit 1 had about twice the level of viscous damping. A failure of the dissipators to provide damping in compression in the case of Unit 2 resulted in equivalent viscous damping ratios much lower than those obtained by Unit 3, see Figures 5.2 (b) and (c). As previously explained in section 4.3.2 this failure was attributed to two causes. The main cause was associated with the use of plywood pugs that dammed the steel ducting into which the dissipators were grouted. The other was attributed to a push-out failure caused by excessive bearing of the post-tensioning anchors that resulted in crushing and spalling of the concrete. Unit 2 shows slightly higher levels of damping at very low drifts due to the length of the milled portion of the dissipator being shorter than that used in Unit 3. The equivalent viscous damping of Unit 3 increases from approximately 6% at 0.25% drift, to 12% at 3% drift. Conversely, the equivalent viscous damping for Unit 2 remained essentially constant at 8% up until 1.0% drift at which point there was a gradual drop off in equivalent viscous damping eventually providing only 3% at 3% drift. This response indicates that a full push out failure of the dissipators occurred at drifts approaching of 1%.

Relatively high levels of equivalent viscous damping, such as that associated with the monolithic construction of Unit 1, reduce the structures displacement demand though the damage caused to the structure may be irreparable after a large earthquake, or very costly given even a moderate event. Neither situation being ideal. The hybrid design of Units 2 and 3 in comparison however showed very little damage to the wall panel, after attaining drifts well in excess of that achieved by Unit 1, see Figure 5.1.

There is common misconception that arises when one sees the rocking motion of a hybrid wall, in that it appears to elongate significantly more than equivalent monolithic systems. This however is an optical illusion as is shown in Figure 5.4. The elongation that arises from the opening of the joint at the base of the wall in the case of a hybrid system, can be expected to be of a similar magnitude to that associated with the summation of the crack widths up the wall panel in a monolithic wall dominated by flexure. The approximately 20% more elongation of Unit 2 is due to a larger percentage of the lateral displacement applied to Unit 2 attributed to rocking, compared to that of Unit 1 where flexure dominates, but a significant amount of shear deformations exists (refer Figures 4.17 and 4.40). Figure 5.4 would have shown an even closer correlation had the instrumentation in the case of Unit 1 been placed up the entire height of the wall.

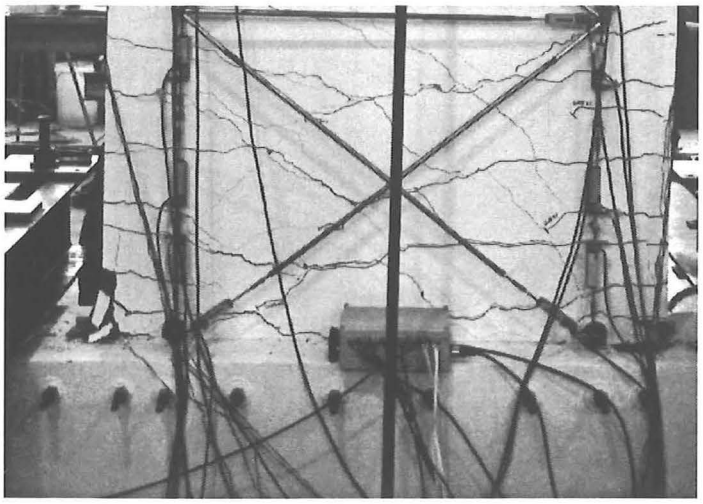

(a) Unit 1 at 2.5% drift

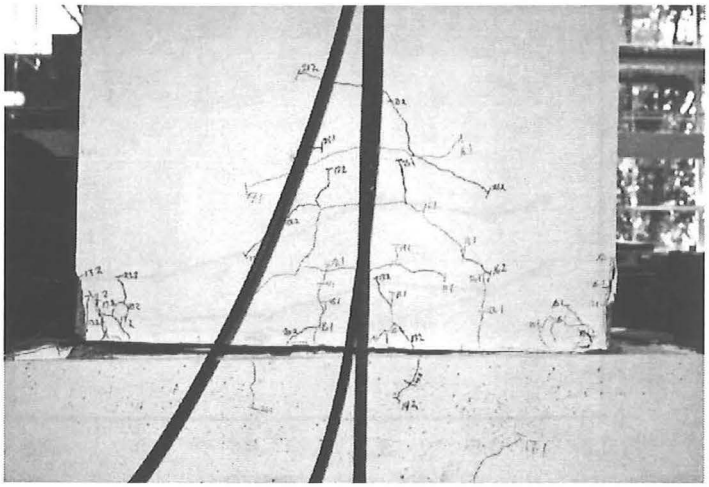

(b) Unit 3 at 3% drift (Rahman and Restrepo, 2000)

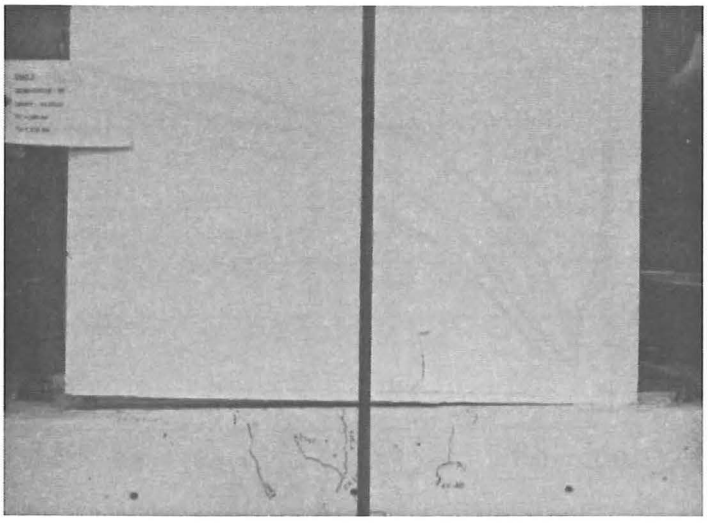

(c) Unit 2 at 3% drift

Figure 5.1 Cracking of wall panel at design level drifts.

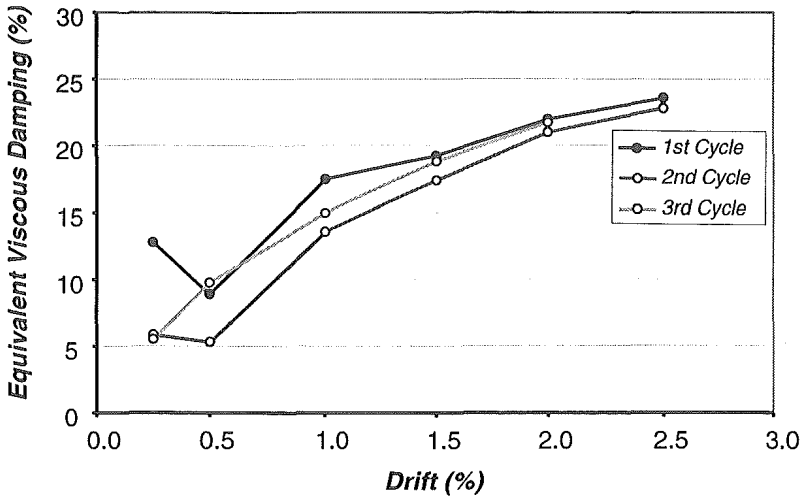

(a) Equivalent viscous damping for Unit 1

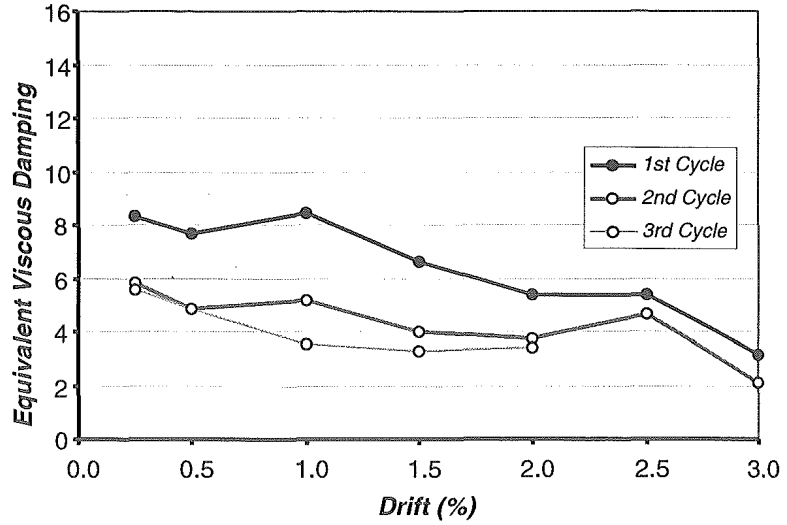

(b) Equivalent viscous damping for Unit 2.

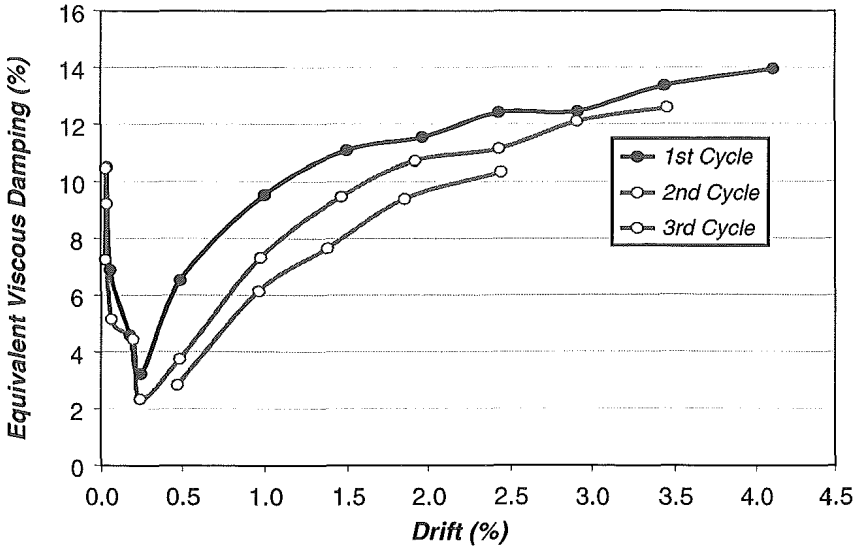

(c) Equivalent viscous damping for Unit 3 (Rahman and Restrepo, 2000)

Figure 5.2 Comparison of equivalent viscous damping ratios.

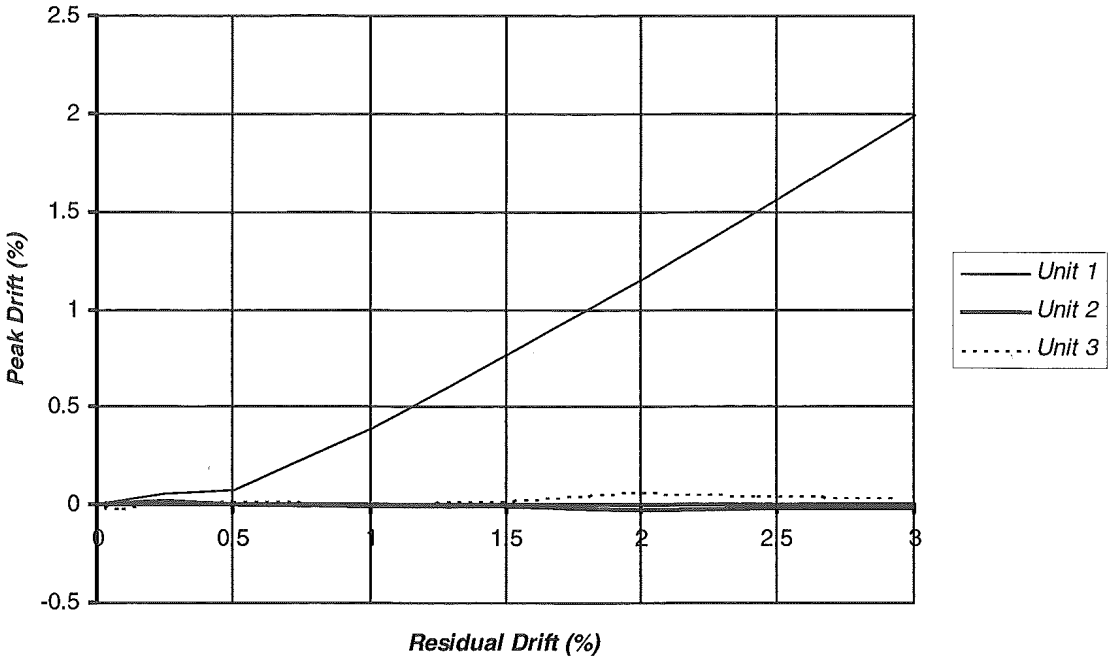

Figure 5.3 Comparison of relative residual drifts between units.

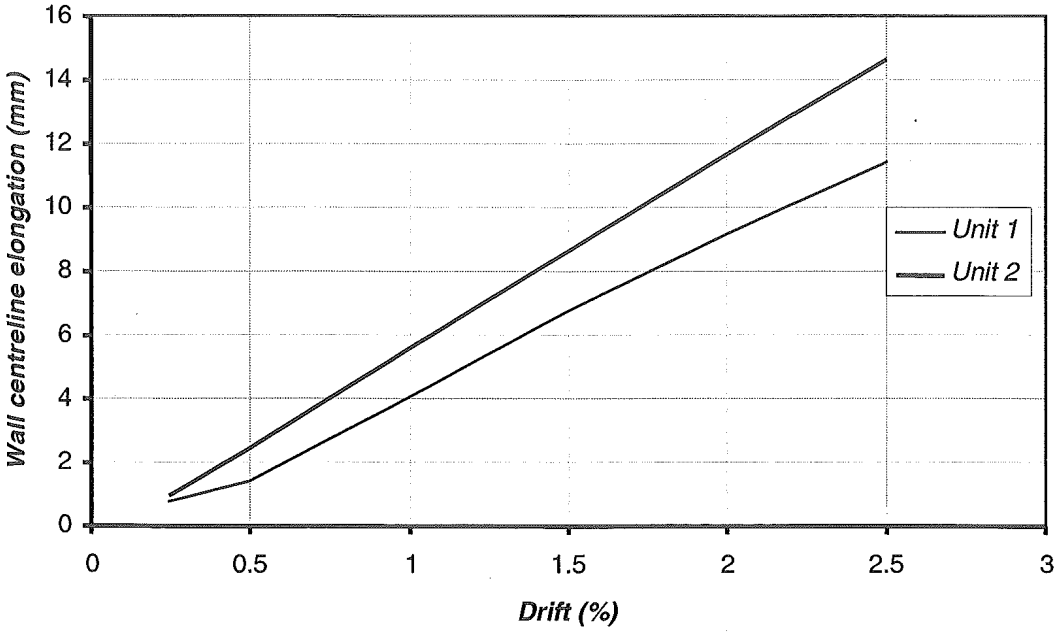

Figure 5.4 Comparison of centreline elongation of Units 1 and 2.

6 CONCLUSIONS

Comparison was made between the test results of a precast concrete cantilever wall designed to emulate ductile monolithic behaviour and a hybrid system incorporating carbon fibre prestressing tendons and steel fibre reinforcement. The monolithic wall performed as expected with energy dissipated through the formation of plastic hinge designed for sufficient ductility. The recess connection provided the ideal monolithic connection assumed in design. The unit eventually failed due to fracture of the longitudinal reinforcement, preceded by buckling, after cycles to 2.5% drift. Residual cracks between 1mm and 2.2mm in width were recorded at the onset of yielding at 1.0% drift. In contrast, the hybrid wall reached a drift in excess of 6.0% drift with virtually no cosmetic damage to the wall panel prior to failure. The development of a gap due to the rigid body rotation of the wall panel closed at all cycles upon unloading resulting in essentially zero residual drift. An unexpected push-out failure of the tapered energy dissipation bars resulted in a reduced energy dissipation capacity for the hybrid unit. Advantages of the hybrid post-tensioned wall system over conventional reinforced ductile design were shown to include:

1. **Essentially no cosmetic damage to wall panels at drift capacities well in excess of design requirements.** Zero, or minimal repair costs in terms of time and money.
2. **Negligible residual drift.** Enabling occupation directly after a strong seismic event. Minimising business loses due to down-time, lost revenue, and stock.
3. **Simple detailing.** Plastic hinge zones do not form, with special confinement restricted to the corners of the wall about which it rocks.
4. **Initial high stiffness due to post-tensioning.** Prior to decompression of the extreme fibres under lateral displacement.
5. **Geometrical Consideration.** The lack of a plastic hinge in the wall panel eases the geometrical limitations imposed on monolithic walls.
6. **System is extremely well suited to the precasting industry.** Construction of walls can be completed quickly and efficiently, fully or partially, off site at a specialist facility. The use of steel fibre reinforcement is an added benefit for simplifying the reinforcing details in the wall panel.

7 SUGGESTIONS FOR FUTURE RESEARCH

Issues and suggestion raised from this research which require further investigation:

1. A Cost-benefit analysis of initial construction costs comparing hybrid systems against conventional monolithic ductile construction, as well as a complete life cycle cost-benefit analysis.

2. Incorporating the hybrid system philosophy with various types of energy dissipation methods, such as "dual-phase" steel dissipating bars, or externally attached systems that could be more easily inspected and replaced.

3. Effects of out-of-plane loading on hybrid wall systems.

4. Alternative detailing of wall ends to provide confinement for the wall ends. Proposed but eventually not used in the construction of Unit 2 was the idea of incorporating perforated plates within these regions, see Figure 7.1.

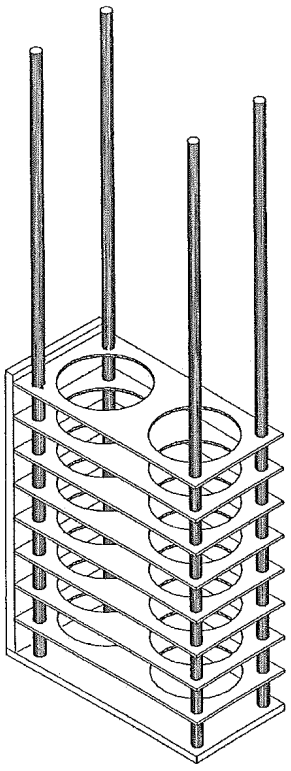

Figure 7.1 Proposed corner confinement reinforcement for Hybrid Wall system.

5. An alternative reinforcing detail to preclude the push-out failure experienced by the energy dissipator bars is shown in Figure 7.2. The duct is drawn with a circular steel plate to prevent compression of the pug. Hanger bars acting below the dissipator, transfer the forces to the top of the foundation beam, rather than relying on strut action as shown in Figure 2.40.

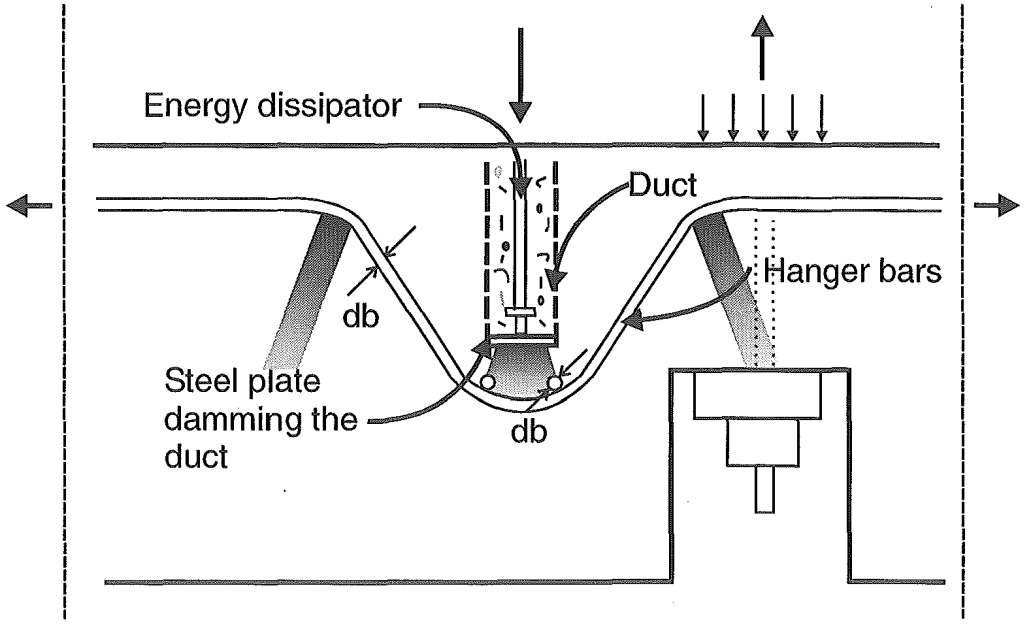

Figure 7.2 Alternative design to avoid energy dissipator push-out failure.

REFERENCES

CAE, "*Guidelines for the use of structural precast concrete in buildings : report of a Study Group of the New Zealand Concrete Society and the New Zealand National Society for Earthquake Engineering*", Centre for Advanced Engineering, University of Canterbury, Christchurch, 1991, 144p.

Chopra, A.K., "*Dynamics of Structures : Theory and Applications to Earthquake Engineering*", Prentice Hall, 1995, 729p.

Collins, M. and Mitchell, D., "*Prestressed Concrete Structures*", Prentice Hall, 1991, 766p.

Kurama, Y., Pessiki, S., Sause, R. and Le-Wu Lu, "*Seismic Behavior and Design of Unbonded Post-tensioned Precast Concrete Walls*", *PCI Journal*, 38(3), 1999. pp. 72-93.

NZS 3101: 1995, Concrete Structures Standard, Part 1: *"The Design of Concrete Structures"* and Part 2: *"Commentary on the Design of Concrete Structures"*, Standards Association of New Zealand, Wellington, 1995.

NZS 4203: 1992, *"Code of Practice for General Structural Design and Design Loadings for Buildings"*, Standards Association of New Zealand, Wellington, 1992.

Otani, S., *"Development of Performance-Based Design Methodology in Japan"*, *Seismic Design Methodologies for the Next Generation of Codes* (eds: Fajfar and Krawinkler, AA. Balkema, 1997, pp. 59-67.

Priestley, M.J.N. and Tao, J.R.T., *"Seismic Response of Precast Prestressed Concrete Frames with Partially Debonded Tendons"*, *PCI Journal*, 38 (1), 1993, pp. 58-69.

Priestley, M.J.N., Sritharan, S., Conley, J.R. and Pampanin, S., "*Preliminary Results and Conclusions From the PRESSS Five-Story Precast Concrete Test Building*", PCI Journal, 44(6), 1999, pp. 42-67.

Rahman, A. and Restrepo, J.I., *"Earthquake Resistant Precast Concrete Buildings: Seismic Performance of Cantilever Walls Prestressed using Unbonded Tendons"*, Research Report 2000-5, Department of Civil Engineering, University of Canterbury, Christchurch, New Zealand, 2000.

Restrepo, J.I., *"Seismic Behaviour of Connections between Precast Concrete Elements"*, Research Report, Department of Civil Engineering, University of Canterbury, Christchurch, New Zealand, 1992.

Skinner, R.I., Robinson, W.H. and McVerry, G.H., *"An Introduction to Seismic Isolation"*, John Wiley & Sons, 1993.

UBC 1997, "*Uniform Building Code*", International Conference of Building Officials, Whittier, California, Vol. 2, 1997.

Whiteside, M. *"The Performance of Slender Precast Conventionally Reinforced Cantilever Walls incorporating Steel Fibre Reinforced Concrete under Seismic Forces"*, M.E thesis, Department of Civil Engineering, University of Canterbury, Christchurch, New Zealand, 2000.

Wood, S. Wright, J. and Moehle, J. *"The 1985 Chile Earthquake, Observations on Earthquake-Resistant Construction in Vina del Mar"*, Civil Engineering Studies, Structural Research series No 532, University of Illinios, Urbana, Feb 1987.

Wyllie Jr, L.A and Filson, J.R. (eds), *"Armenia Earthquake Reconnaissance Report"*, Earthquake Spectra Publication 89.01, Special supplement, August 1989.

APPENDIX A - Design actions of foundation beam for Unit 2

a) LATERAL LOAD

Node	x	y
a	0	50
b	600	500
c	600	445
d	825	50
e	934.1	0
f	1065.6	215
g	1212	445
h	1212	50
i	1325	310
j	1325	215
k	1410	252
l	1590	283.6
m	1675	310
n	1675	276.4
o	1788	276.4
p	1788	50
q	2094	445
r	2094	50
s	2400	50
t	2400	0
u	3000	50

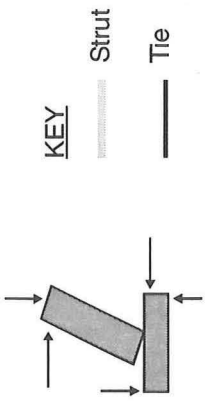

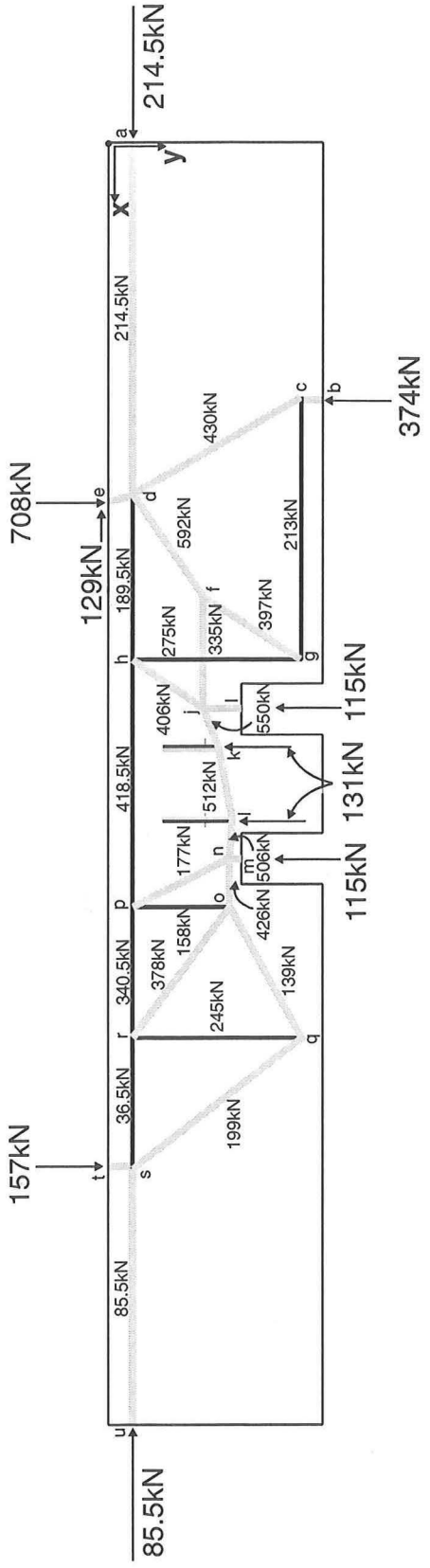

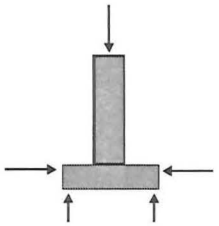

KEY

Strut

Tie

Node	x	y
a	0	50
b	600	500
c	600	268
d	962	268
e	962	50
f	962	0
g	1325	310
h	1325	268
i	1325	50
j	1325	0
k	1410	215
l	1590	215
m	1675	310
n	1675	268
o	1675	50
p	1675	0
q	2037	268
r	2037	50
s	2037	0
t	2400	500
u	2400	268
v	3000	50

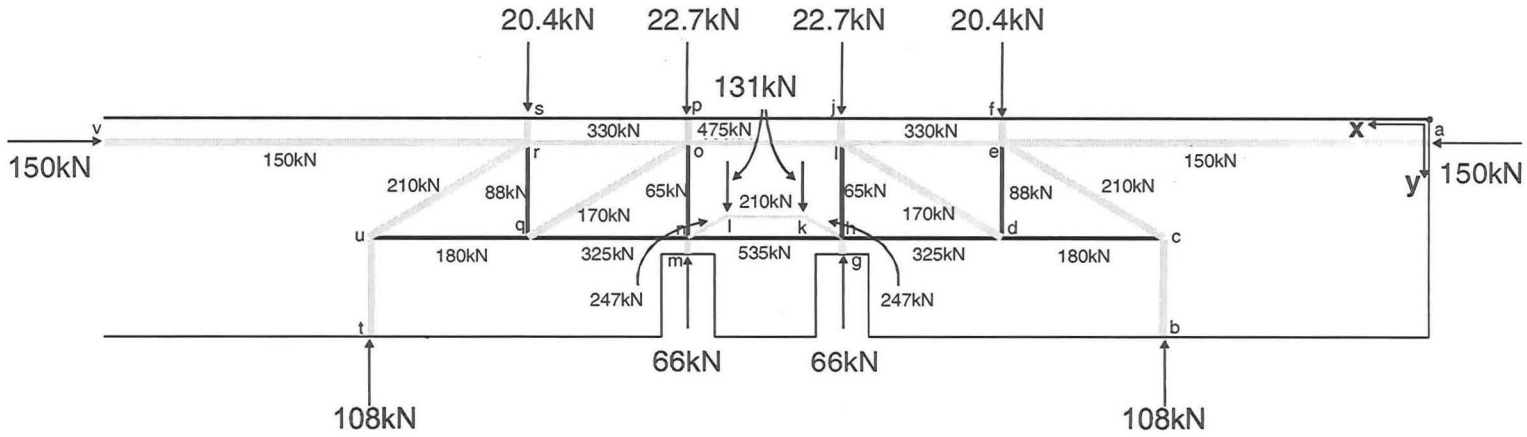

APPENDIX B - Hysteretic response for Units 1 and 2

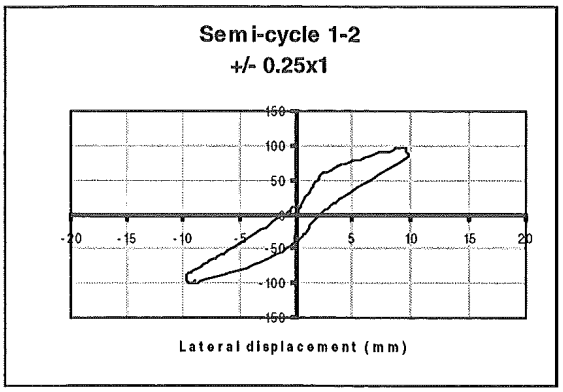

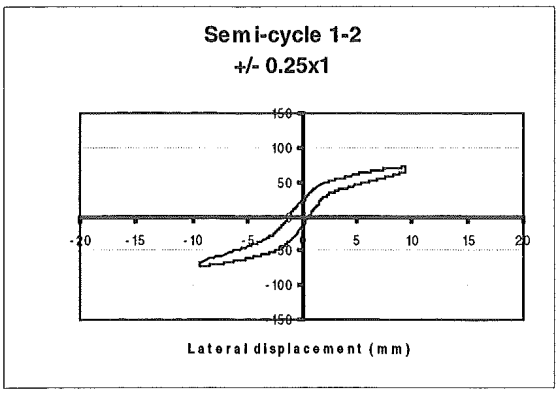

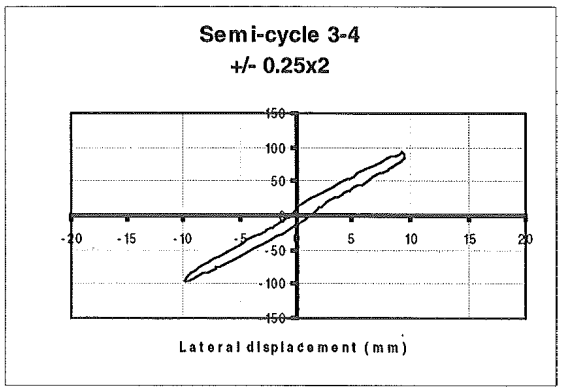

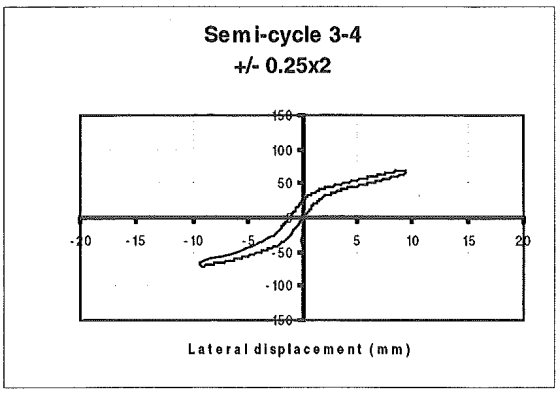

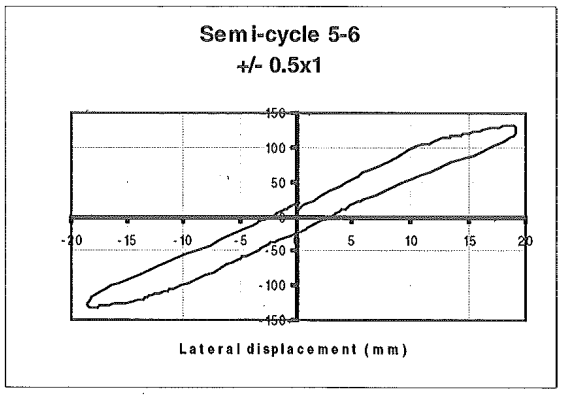

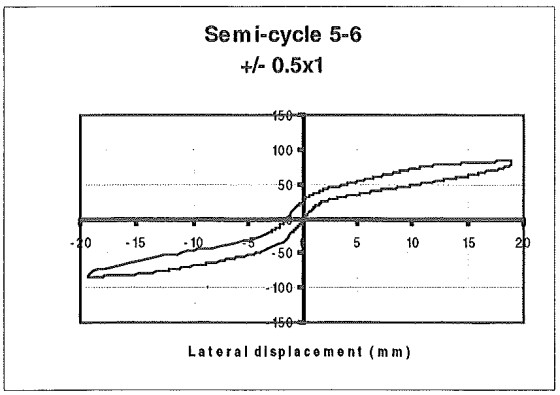

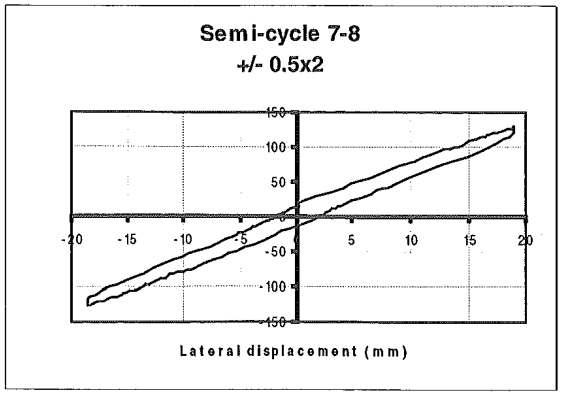

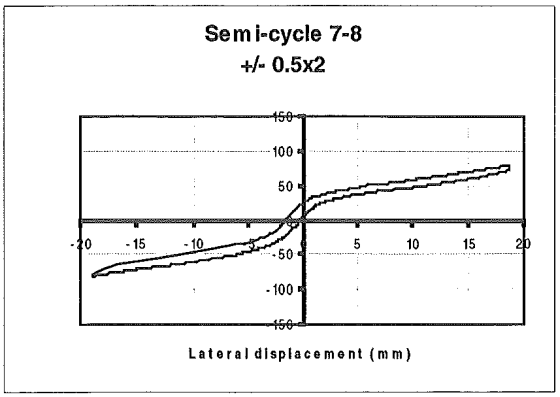

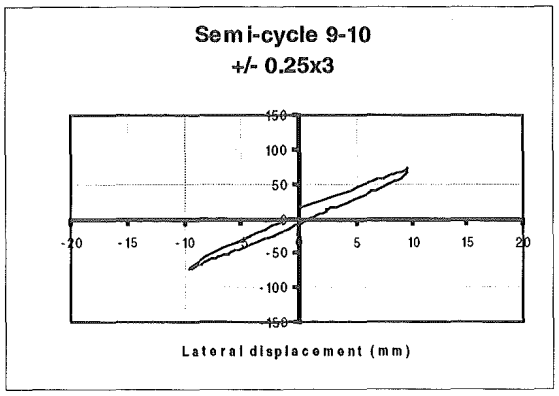
Semi-cycle 9-10
+/- 0.25x3
Lateral displacement (mm)

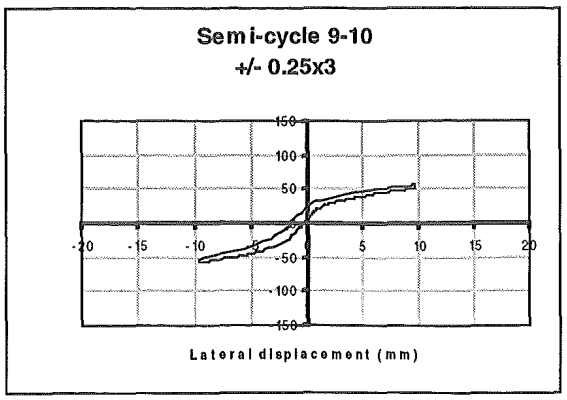
Semi-cycle 9-10
+/- 0.25x3
Lateral displacement (mm)

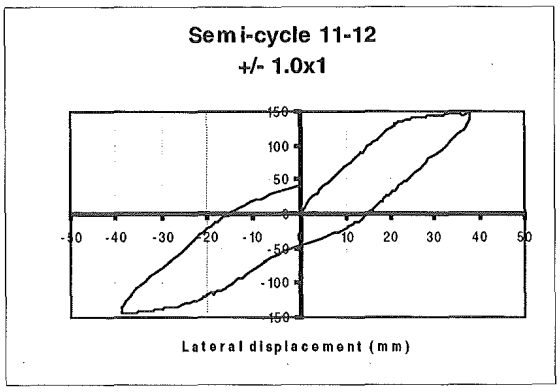
Semi-cycle 11-12
+/- 1.0x1
Lateral displacement (mm)

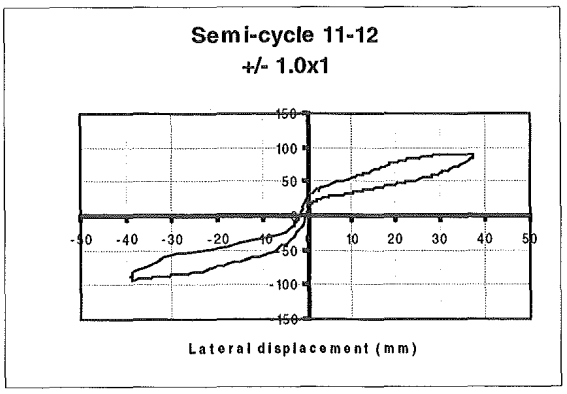
Semi-cycle 11-12
+/- 1.0x1
Lateral displacement (mm)

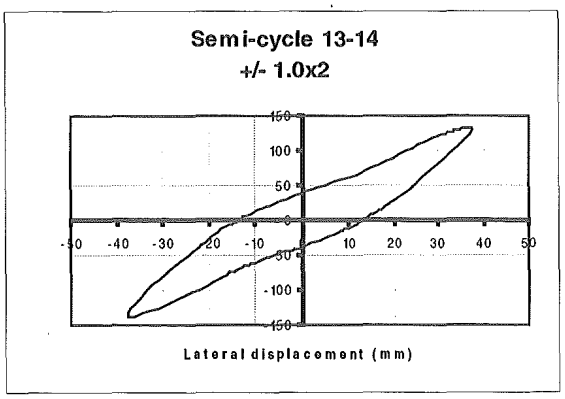
Semi-cycle 13-14
+/- 1.0x2
Lateral displacement (mm)

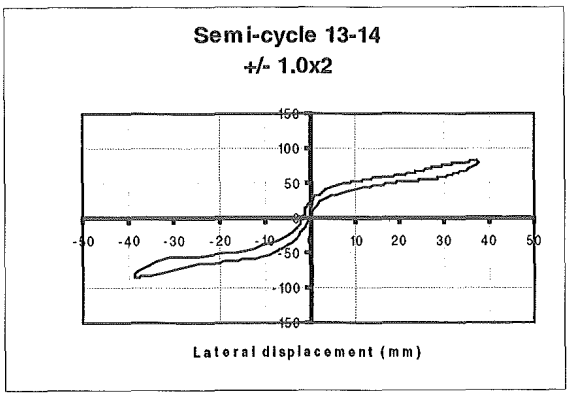
Semi-cycle 13-14
+/- 1.0x2
Lateral displacement (mm)

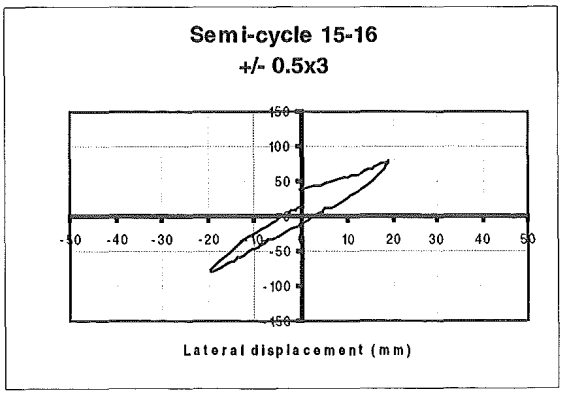
Semi-cycle 15-16
+/- 0.5x3
Lateral displacement (mm)

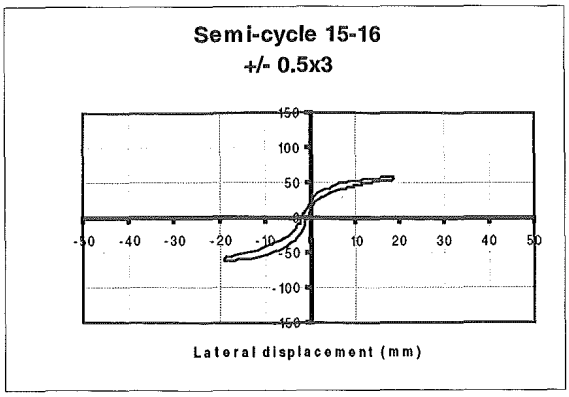
Semi-cycle 15-16
+/- 0.5x3
Lateral displacement (mm)

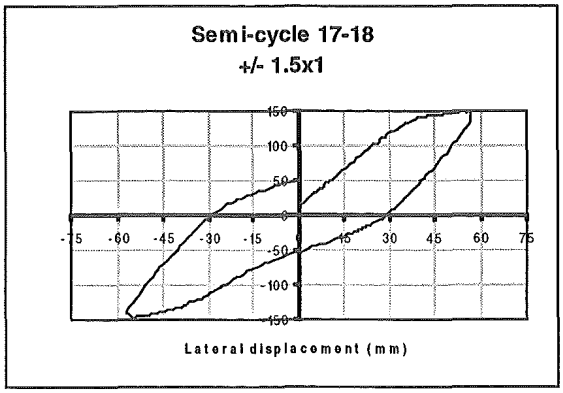
Semi-cycle 17-18
+/- 1.5x1
Lateral displacement (mm)

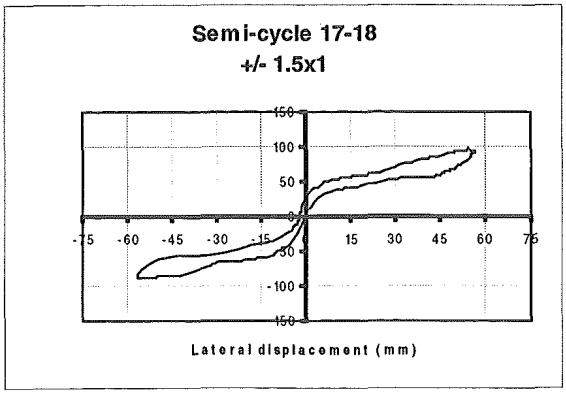
Semi-cycle 17-18
+/- 1.5x1
Lateral displacement (mm)

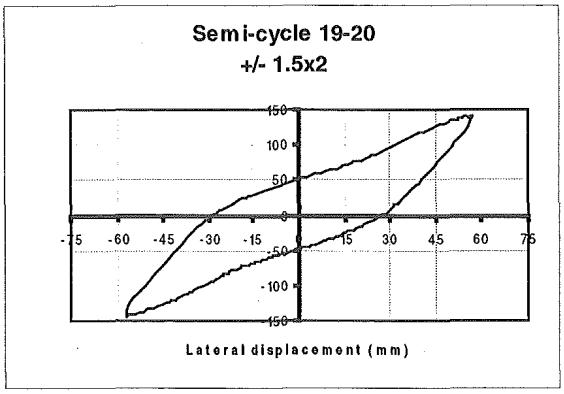
Semi-cycle 19-20
+/- 1.5x2
Lateral displacement (mm)

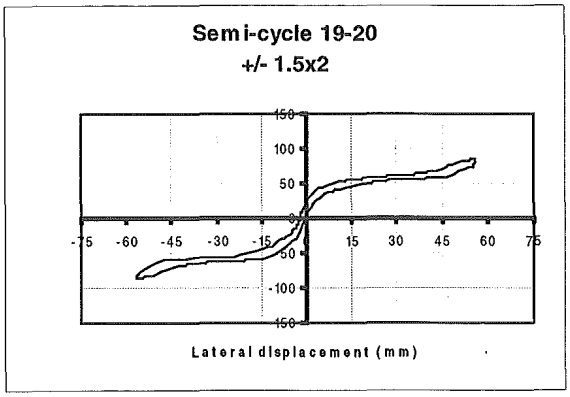
Semi-cycle 19-20
+/- 1.5x2
Lateral displacement (mm)

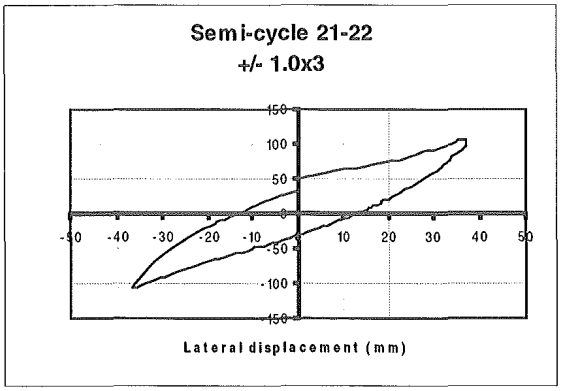
Semi-cycle 21-22
+/- 1.0x3
Lateral displacement (mm)

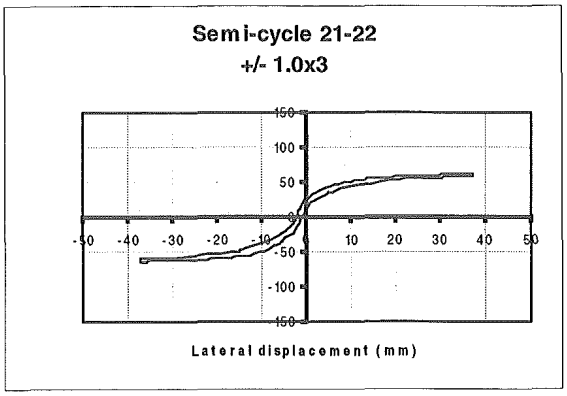
Semi-cycle 21-22
+/- 1.0x3
Lateral displacement (mm)

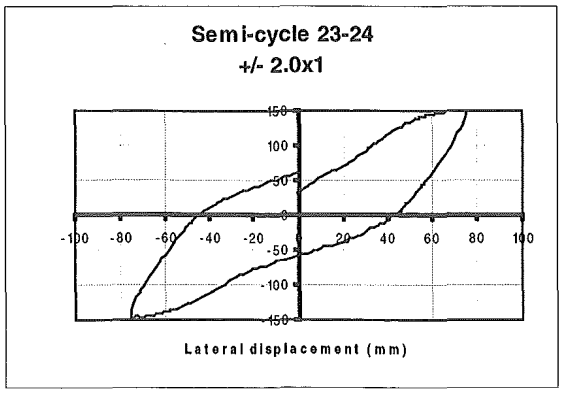
Semi-cycle 23-24
+/- 2.0x1
Lateral displacement (mm)

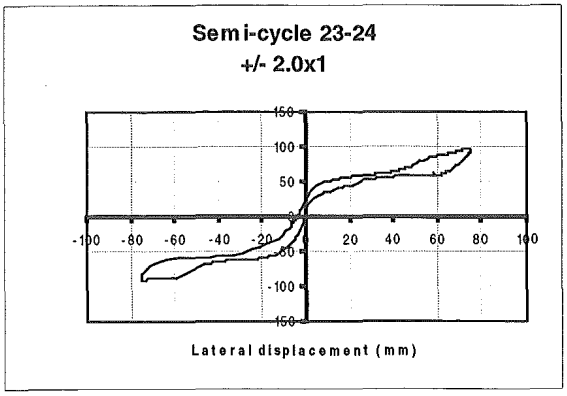
Semi-cycle 23-24
+/- 2.0x1
Lateral displacement (mm)

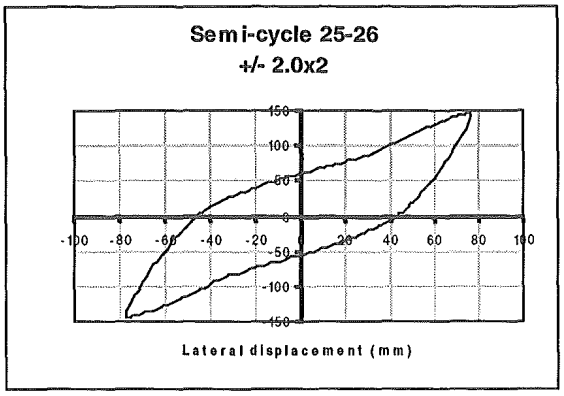
Semi-cycle 25-26
+/- 2.0x2
Lateral displacement (mm)

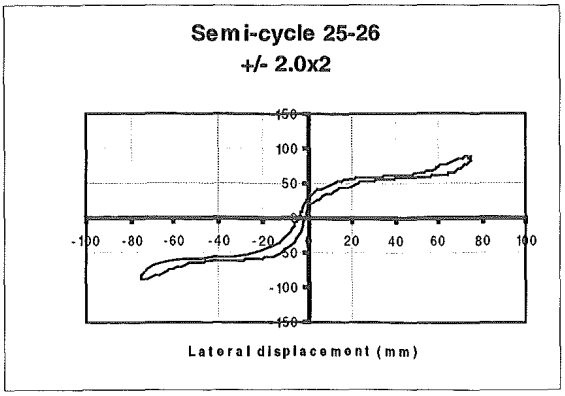
Semi-cycle 25-26
+/- 2.0x2
Lateral displacement (mm)

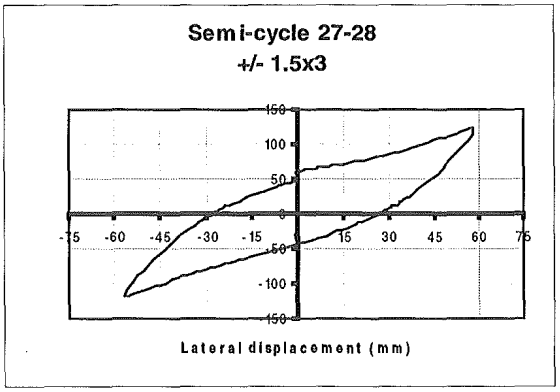
Semi-cycle 27-28
+/- 1.5x3
Lateral displacement (mm)

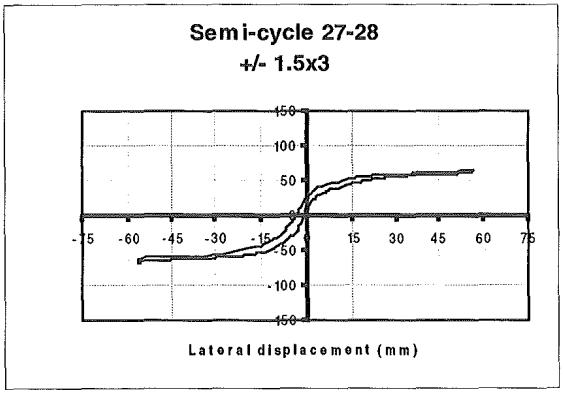
Semi-cycle 27-28
+/- 1.5x3
Lateral displacement (mm)

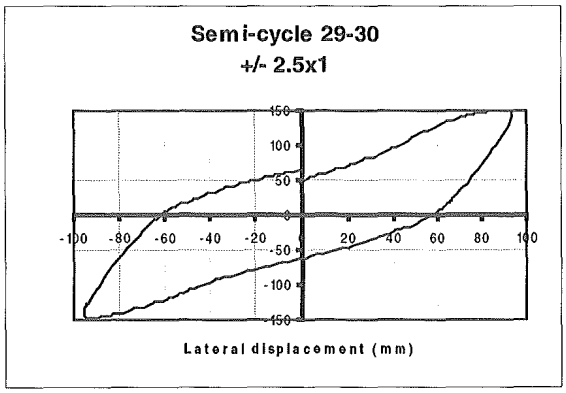
Semi-cycle 29-30
+/- 2.5x1
Lateral displacement (mm)

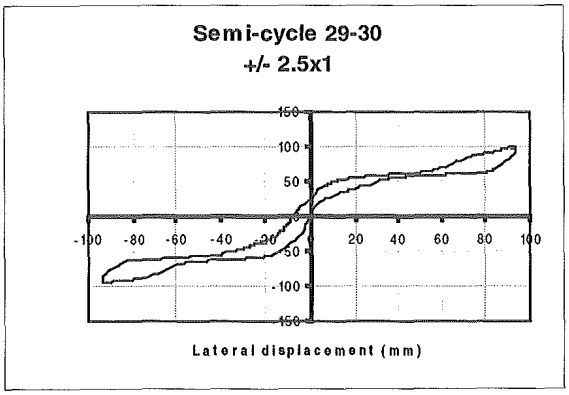
Semi-cycle 29-30
+/- 2.5x1
Lateral displacement (mm)

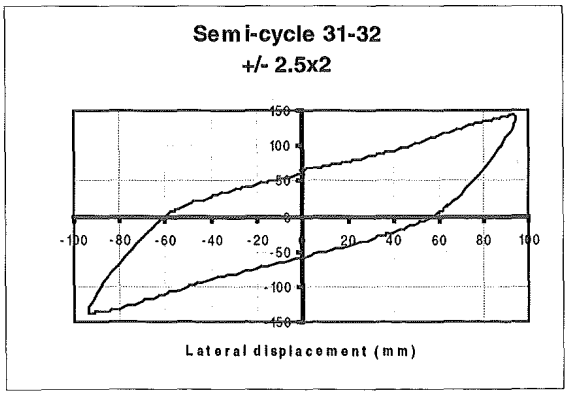
Semi-cycle 31-32
+/- 2.5x2
Lateral displacement (mm)

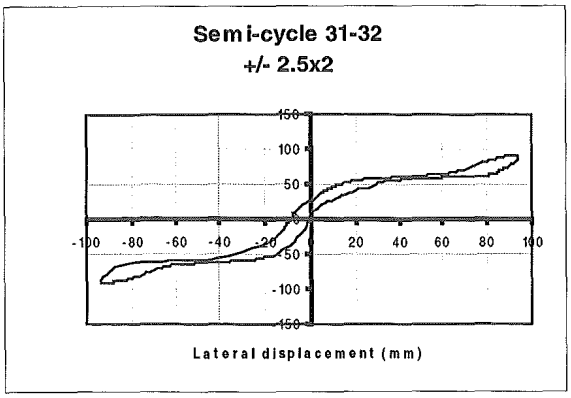
Semi-cycle 31-32
+/- 2.5x2
Lateral displacement (mm)

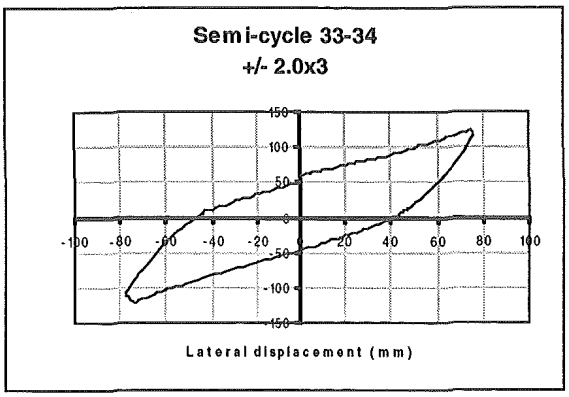
Semi-cycle 33-34
+/- 2.0x3
150
100
50
0
-50
-100
-150
-100 -80 -60 -40 -20 0 20 40 60 80 100
Lateral displacement (mm)

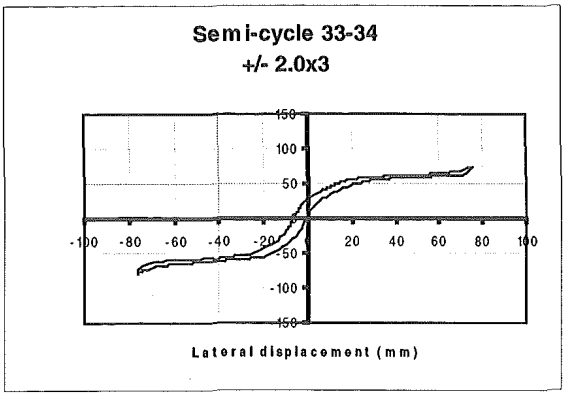
Semi-cycle 33-34
+/- 2.0x3
150
100
50
0
-50
-100
-150
-100 -80 -60 -40 -20 20 40 60 80 100
Lateral displacement (mm)

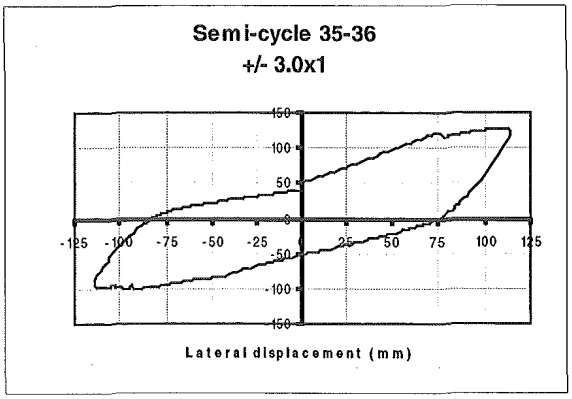
Semi-cycle 35-36
+/- 3.0x1
150
100
50
0
-50
-100
-150
-125 -100 -75 -50 -25 0 25 50 75 100 125
Lateral displacement (mm)

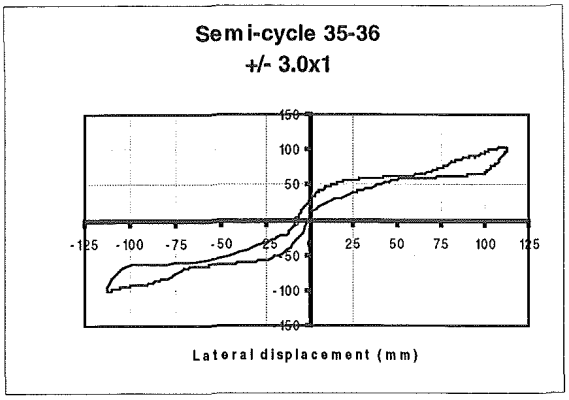
Semi-cycle 35-36
+/- 3.0x1
150
100
50
0
-50
-100
-150
-125 -100 -75 -50 -25 25 50 75 100 125
Lateral displacement (mm)

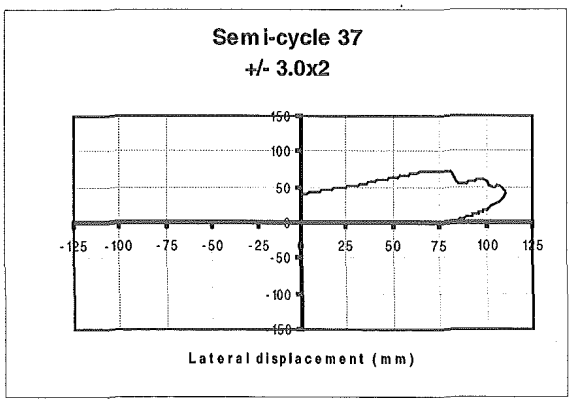
Semi-cycle 37
+/- 3.0x2
150
100
50
0
-50
-100
-150
-125 -100 -75 -50 -25 0 25 50 75 100 125
Lateral displacement (mm)

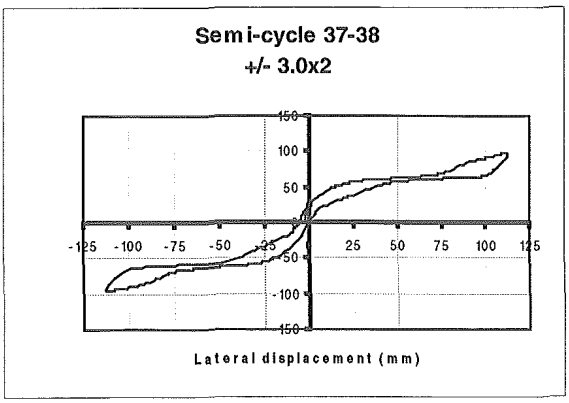
Semi-cycle 37-38
+/- 3.0x2
150
100
50
0
-50
-100
-150
-125 -100 -75 -50 -25 25 50 75 100 125
Lateral displacement (mm)

APPENDIX C - Spreadsheet summarising the dissipator design used in Unit 2 and by Rahman and Restrepo, (2000)

CASE : New Design

L_{ed} =	**165**	mm
a =	**15**	mm
a+b =	**180**	mm
$2a/(d_b-d_{br})$ =	**7.5**	

d_b =	**20**	mm
d_{br} =	**16**	mm

Δ_e =	**13.39**	mm

λ_u =	1.4	
f_y =	465	MPa
$0.5\varepsilon_{su}$ =	0.08	
ε_y =	0.00233	

Check bar bearing

$(\Delta\varepsilon_a+a)*\theta_v$ =	**0.308**	mm
OA =	**1.76**	mm

OA <> $(\Delta\varepsilon_a+a)*\theta_v$ =>
Bar does not bear

a_y =	10.993	mm
d_{by} =	18.9315	mm

A(y) =	281.487	mm^2
F =	130891	N
$f_s(y)$ =	465	MPa

$\varepsilon_s(y)$ =	0.00233	
$\Delta\varepsilon_a$ =	0.41667	mm
y =	10.993	mm

$\Delta\varepsilon_b$ =	**13.2**	mm
$\Delta\varepsilon_a$ =	**0.417**	mm
Δ_{tot} =	**13.62**	mm

Check surface strain

$\theta_{v\,1}$ =	0.02	
$\theta_{v\,2}$ =	0.02	
θ_t =	-0.0048	
θ_b =	-0.0079	
ε_{ss} =	**0.741**	ε_{su}

ε_{ss} <> $0.8\varepsilon_{su}$ => **Surface strain OK**

CASE : Rahman and Restrepo (2000)

L_{ed} =	**200**	mm
a =	**10**	mm
a+b =	**210**	mm
$2a/(d_b-d_{br})$ =	**5**	

d_b =	**20**	mm
d_{br} =	**16**	mm

Δ_e =	**13.39**	mm

λ_u =	1.4	
f_y =	465	MPa
$0.5\varepsilon_{su}$ =	0.10667	
ε_y =	0.00233	

Check bar bearing

$(\Delta\varepsilon_a+a)*\theta_v$ =	**0.207**	mm
OA =	**4.267**	mm

OA <> $(\Delta\varepsilon_a+a)*\theta_v$ =>
Bar does not bear

a_y =	7.32864	mm
d_{by} =	18.9315	mm

A(y) =	281.487	mm^2
F =	130891	N
$f_s(y)$ =	465	MPa

$\varepsilon_s(y)$ =	0.00233	
$\Delta\varepsilon_a$ =	0.36729	mm
y =	7.32864	mm

$\Delta\varepsilon_b$ =	**21.33**	mm
$\Delta\varepsilon_a$ =	**0.367**	mm
Δ_{tot} =	**21.7**	mm

Check surface strain

$\theta_{v\,1}$ =	0.02	
$\theta_{v\,2}$ =	0.02	
θ_t =	-0.0012	
θ_b =	-0.0043	
ε_{ss} =	**0.726**	ε_{su}

ε_{ss} <> $0.8\varepsilon_{su}$ => **Surface strain OK**

Errata for "A Comparison of the Seismic Performance of Precast Wall Construction: Emulation and Hybrid Approaches" by Tony J. Holden . Supervised by Dr J. I Restrepo and Professor J. B. Mander.

Research report 2001 – 4
April 2001
ISSN 0110 – 3326

The following equations shall be replaced in the text as follows:

Equation (2.5) Pg. 38

$$f_t = \frac{2(P+W+2F_{ed})e}{b_w H_w^{\,2}\sqrt{1+\left(\frac{l_w}{H_w}\right)^2}} \qquad (2.5)$$

Equation (2.6) Pg. 38

$$e \le \frac{l_w}{4\cos(\theta)} = \frac{L_w}{4}\sqrt{1+\left(\frac{l_w}{H_w}\right)^2} \qquad (2.6)$$

Equation (2.7) Pg.38

$$f_t \le \frac{(P+W+2F_{ed})l_w}{2b_w H_w^{\,2}} \qquad (2.7)$$

Equation (2.9) Pg.38

$$\frac{f_t}{f'_t} \le \frac{(P+W+2F_{ed})l_w}{0.66b_w H_w^{\,2}\sqrt{f'_c}} \qquad (2.9)$$